# A cardiac electromechanical model coupled with a lumped-parameter model for closed-loop blood circulation

F. Regazzoni [a,*], M. Salvador [a], P.C. Africa [a], M. Fedele [a], L. Dedè [a],
A. Quarteroni [a,b]

[a] *MOX – Dipartimento di Matematica, Politecnico di Milano, P.zza Leonardo da Vinci 32, 20133 Milano, Italy*
[b] *Mathematics Institute, École Polytechnique Fédérale de Lausanne, Av. Piccard, CH-1015 Lausanne, Switzerland*

## ARTICLE INFO

## ABSTRACT

We propose a novel mathematical and numerical model for cardiac electromechanics, wherein biophysically detailed core models describe the different physical processes concurring to the cardiac function. The core models, once suitably approximated, are coupled by a computationally efficient strategy. Our model is based on: (1) the combination of implicit-explicit (IMEX) schemes to solve the different core cardiac models, (2) an Artificial Neural Network based model, that surrogates a biophysically detailed but computationally demanding microscale model of active force generation and (3) appropriate partitioned schemes to couple the different models in this multiphysics setting. We employ a flexible and scalable intergrid transfer operator, which allows to interpolate Finite Element functions between nested meshes and, possibly, among arbitrary Finite Element spaces for the different core models. Our core 3D electromechanical model of the left ventricle is coupled with a closed-loop 0D model of the vascular network (and the other cardiac chambers) by an approach that is energy preserving. More precisely, we derive a balance law for the mechanical energy of the whole circulatory network. This provides a quantitative insight into the energy utilization, dissipation and transfer among the different compartments of the cardiovascular network and during different stages of the heartbeat. On this ground, a new tool is proposed to validate some energy indicators adopted in the daily clinical practice. A further contribution of this paper is the proposition of a robust algorithm for the reconstruction of the stress-free reference configuration. This feature is fundamental to correctly initialize our electromechanical simulations. As a matter of fact, the geometry acquired from medical imaging typically refers to a configuration affected by residual internal stresses, whereas the elastodynamics equations that govern the mechanics core model are related to a stress-free configuration. To prove the biophysical accuracy of our computational model, we address different scenarios of clinical interest, namely by varying preload, afterload and contractility.

© 2022 The Author(s). Published by Elsevier Inc. This is an open access article under the CC BY license (http://creativecommons.org/licenses/by/4.0/).

\* Corresponding author.
   *E-mail address:* francesco.regazzoni@polimi.it (F. Regazzoni).

## 1. Introduction

The coupling between the electric and mechanical activities of the heart is the fundamental physiological process at the basis of the cardiac function [1,2]. For this reason, numerical simulations of cardiac electromechanics are increasingly becoming the cornerstone of computational cardiology and precision medicine of the heart. These electromechanical models offer promising tools to assist clinicians in the decision-making process, by providing personalized assessments of various pathological conditions and related treatments. For instance, patient-specific computational models are built to address rhythm disorders [3]. Among them, an important role is played by cardiac arrhythmias, such as ventricular tachycardia and fibrillation [4], or cardiac dyssynchrony, such as left bundle branch block [5]. In other cases these cardiac *in silico* models, i.e. digital replicas of patients' hearts, are used to study short-term and long-term structural remodeling, which may occur in presence of heart failure, ischemic and hypertrophic cardiomyopathy, and many other diseases [6–9]. Along this line, several mathematical and numerical models have been proposed in the literature, ranging from ventricles [10–15] and atria [16,17] to four chamber human hearts [18–21].

In this paper we present a novel and comprehensive mathematical and numerical model of cardiac electromechanics. We consider a fully coupled model of the cardiac function, which results from the concerted action of several physical processes – electrophysiology, biochemistry, mechanics – interacting at different spatial and temporal scales [14,22–24] ranging from nanometers to centimeters and from nanoseconds to seconds, respectively [1,25]. We describe all of these phenomena in terms of biophysically detailed models, written as systems of PDEs (partial differential equations) and ODEs (ordinary differential equations), which realize the coupling of electrophysiology, ionic model, active force generation at the cellular and tissue levels, passive mechanics of the myocardium, blood flow in the chambers and in the circulatory system. Among the original contributions of this paper, we present a 0D (zero-dimensional) hemodynamic model of the whole cardiovascular system, which is coupled with our 3D electromechanical model of specific cardiac chambers to form a closed-loop 3D-0D circulation model. Such coupling is an essential step to provide physically meaningful numerical simulations, which are performed considering a 3D electromechanical description of the left ventricle only.

Among the different physical phenomena concurring to the heart function, the intrinsic complexity of the subcellular mechanisms underlying active force generation typically dictates the use of phenomenological models [26–28] or Monte Carlo approximations of physics-based models [29–31], which are however characterized by large computational costs. In our electromechanical model, instead, we rely on a physics-based model of force generation, with explicit representation of the cooperative interactions among the subcellular units [32]. As this model features more than 2'000 internal variables, we surrogate it thanks to the Machine Learning algorithm that we proposed in [33]. Specifically, we train – in an offline phase – a reduced-order model, based on Artificial Neural Networks (ANNs), that approximates within a prescribed accuracy the results of the original one. By using this ANN-based model (featuring only two internal variables) instead of the high-fidelity one in the multiscale electromechanical simulation, we reduce the number of variables from more than 2'000 to only 2, with an overall relative error of the order of $10^{-3}$ [33].

We prove that our closed-loop circulation model satisfies a balance of mechanical energy. We provide a quantitative insight in the cardiac energy distribution by calculating the different terms of this balance during a heart beat. We highlight the features of different compartments during the different stages of the heartbeat, i.e. when energy is injected, dissipated or transformed. Thanks to our model we can also assess the validity of simplified relationships commonly used in the clinical practice to estimate the main indicators of heart energy distribution [34].

We prove that the coupling between the 3D electromechanical model and the 0D circulation model is consistent with the principles of energy conservation. Indeed, we impose a boundary condition at the base of the left ventricle that we purposely denote as energy-consistent boundary condition [33,35]. Moreover, we apply a boundary condition at the epicardium that keeps into account the effect of the pericardial sac [14,15].

The computational model for cardiac electromechanics presented in this paper relies on segregated schemes [36–38]. These schemes, also called partitioned, often suffer from instability issues [36,39–41], despite being computationally more attractive than monolithic schemes [15,37,42]. Nonetheless, our numerical approach enables to couple the core models describing the different physics in a numerically stable manner, yet allowing to adopt different resolutions in space and time to reflect their characteristic scales [12,14,43,44,2,45]. With this aim, we implement an efficient and flexible intergrid transfer operator [14,46,47] that allows to couple models defined on different computational meshes and possibly different Finite Element spaces. The single core models are approximated by suitable implicit-explicit (IMEX) schemes [48] in time, aimed at lowering the computational effort associated with each time step without introducing severe CFL restrictions on the time step size otherwise associated to fully explicit schemes [35]. The computational framework presented in this paper realizes a very favorable trade-off between the biophysical detail of the underlying mathematical models and computational efficiency of the corresponding solver. Mathematical rigor, model accuracy and computational efficiency are the landmarks of the proposed electromechanical solver.

We also couple the 3D and the 0D models [49,50] in the segregated scheme by means of a novel numerical approach. We reinterpret the cavity pressure of the left ventricle as a Lagrange multiplier to enforce a volumetric constraint to couple together the 0D circulation model and the 3D electromechanical model. We end up with a saddle-point structure for the mechanical problem, which is numerically solved using the Schur complement reduction [51]. Our scheme is numerically stable and can be applied to all the phases of the heart cycle (filling phase, ejection phase and isovolumetric contraction
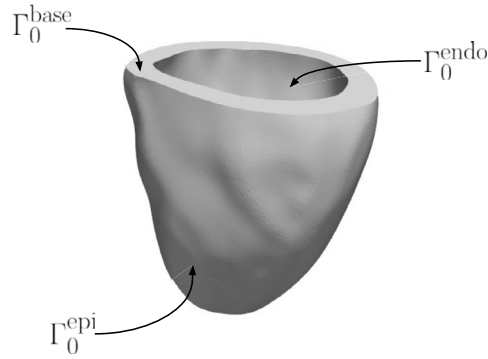
**Fig. 1.** Representation of boundaries $\Gamma_0^{\text{epi}}$, $\Gamma_0^{\text{base}}$ and $\Gamma_0^{\text{endo}}$ of the domain $\Omega_0$, given by the Zygote Solid 3D left ventricle [52].

and relaxation phases) without the need of switching among different 0D models and without considering any change in the parameters of the equations [11,14].

Looking towards the patient-specific customization of our model, we note that cardiac geometries are mostly acquired in vivo with imaging techniques. In this setting, atria and ventricles are loaded, mainly by the pressures acting on the endocardium, and present residual internal stresses. Therefore, the stress-free configuration, to which the equations for cardiac electromechanics must refer, is not known a priori. As this is necessary to set the reference configuration for the mechanical model, we formulate an inverse problem aimed at recovering such stress-free reference configuration starting from the geometry acquired from medical imaging. We also propose a novel and robust algorithm to solve this inverse problem. Nevertheless, its numerical resolution can be computationally demanding for highly refined meshes. For this reason, our algorithm for the recovery of the reference configuration is supplied by a projection technique that accurately retrieve the stress-free configuration from a coarser and independent representation of the computational domain.

We show the effectiveness of our mathematical and numerical approach by simulating the response of the electromechanical model in some physiological and meaningful configurations, namely varying preload, afterload and contractility.

### 1.1. Paper outline

This paper is organized as follows. In Sec. 2 we describe the core cardiac models. In Sec. 3 we derive a balance of the mechanical energy for both the 0D blood circulation model and the 3D-0D electromechanical-circulation coupled model. In Sec. 4 we present the numerical discretization of the different core models and the strategy followed for their coupling. In Sec. 5 we illustrate our algorithm to recover the reference configuration from a stressed geometry. In Sec. 6 we present the numerical results. In particular, we perform different numerical tests by varying preload, afterload and contractility, thus showing the ability of our mathematical model to investigate different scenarios of clinical interest. Finally, in Sec. 7, we draw our conclusions and outlook on future research.

### 2. Mathematical models

We consider a computational domain $\Omega_0 \subset \mathbb{R}^3$, representing the 3D region occupied by the left ventricle (Fig. 1). We split the boundary of $\Omega_0$ into endocardium ($\Gamma_0^{\text{endo}}$), epicardium ($\Gamma_0^{\text{epi}}$) and ventricular base ($\Gamma_0^{\text{base}}$), namely the artificial boundary located where the left ventricle geometry is cut.

In this paper, we consider a multiphysics and multiscale model of cardiac electromechanics made of five different blocks (henceforth denoted as *core models*) plus a coupling condition. The core models are associated with the different physical phenomena concurring – at different spatial and temporal scales – at the heart function. They correspond to the propagation of the electrical potential ($\mathcal{E}$) [53–56], ion dynamics ($\mathcal{I}$) [57–59], active contraction of cardiomyocytes ($\mathcal{A}$) [33,60–63], tissue mechanics ($\mathcal{M}$) [64,65] and blood circulation ($\mathcal{C}$) [49,50]. Finally, the volume conservation condition ($\mathcal{V}$) enables to consistently couple ($\mathcal{M}$) and ($\mathcal{C}$) core models. In Fig. 2 we depict the electric analog circuit corresponding to our 0D circulation model, along with the coupling with a 3D electromechanical description of the left ventricle.

The model features the following unknowns:

$$u: \Omega_0 \times (0,T) \to \mathbb{R}, \qquad \boldsymbol{w}: \Omega_0 \times (0,T) \to \mathbb{R}^{n_{\boldsymbol{w}}}, \qquad \boldsymbol{z}: \Omega_0 \times (0,T) \to \mathbb{R}^{n_{\boldsymbol{z}}},$$
$$\boldsymbol{s}: \Omega_0 \times (0,T) \to \mathbb{R}^{n_{\boldsymbol{s}}}, \qquad \boldsymbol{d}: \Omega_0 \times (0,T) \to \mathbb{R}^3, \qquad \boldsymbol{c}_1: (0,T) \to \mathbb{R}^{n_{\boldsymbol{c}}}, \qquad (1)$$
$$p_{\text{LV}}: (0,T) \to \mathbb{R}$$

where $u$ denotes the transmembrane potential, $\boldsymbol{w}$ and $\boldsymbol{z}$ the ionic variables, $\boldsymbol{s}$ the states variables of the force generation model, $\boldsymbol{d}$ the mechanical displacement of the tissue, $\boldsymbol{c}_1$ is the state vector of the circulation models (pressures, volumes and
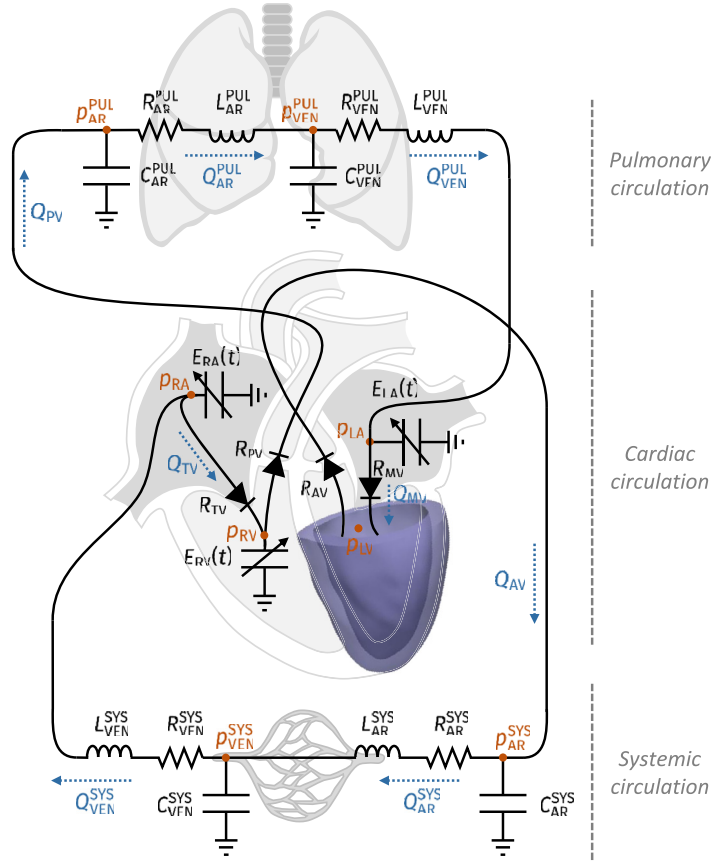
**Fig. 2.** 3D-0D coupling between the left ventricle 3D electromechanical model and the 0D model. The state variables corresponding to pressures and fluxes are depicted in orange and blue, respectively. (For interpretation of the colors in the figure(s), the reader is referred to the web version of this article.)

fluxes in the different compartments of the vascular network) and $p_{LV}$ is the left ventricle pressure. The model reads as follows:

$$(\mathscr{E}) \begin{cases} J\chi_m \left[ C_m \dfrac{\partial u}{\partial t} + \mathcal{I}_{ion}(u, \boldsymbol{w}, \boldsymbol{z}) \right] - \nabla \cdot (J\mathbf{F}^{-1}\boldsymbol{D}_M\mathbf{F}^{-T}\nabla u) = J\chi_m \mathcal{I}_{app}(t), \\ \left( J\mathbf{F}^{-1}\boldsymbol{D}_M\mathbf{F}^{-T}\nabla u \right) \cdot \mathbf{N} = 0 \qquad\qquad\qquad \text{on } \partial\Omega_0 \times (0, T), \end{cases} \tag{2a}$$

in $\Omega_0 \times (0, T)$, with $u = u_0$ in $\Omega_0$ at time $t = 0$.

$$(\mathscr{I}) \begin{cases} \dfrac{\partial \boldsymbol{w}}{\partial t} - \boldsymbol{H}(u, \boldsymbol{w}) = \boldsymbol{0}, \\ \dfrac{\partial \boldsymbol{z}}{\partial t} - \boldsymbol{G}(u, \boldsymbol{w}, \boldsymbol{z}) = \boldsymbol{0}, \end{cases} \tag{2b}$$

in $\Omega_0 \times (0, T)$, with $\boldsymbol{w} = \boldsymbol{w}_0$ and $\boldsymbol{z} = \boldsymbol{z}_0$ in $\Omega_0$ at time $t = 0$.

$$(\mathscr{A}) \quad \dfrac{\partial \mathbf{s}}{\partial t} = \boldsymbol{K}(\mathbf{s}, [Ca^{2+}]_i, SL), \tag{2c}$$

in $\Omega_0 \times (0, T)$, with $\mathbf{s}(0) = \mathbf{s}_0$ in $\Omega_0$ at time $t = 0$.

$$(\mathscr{M}) \begin{cases} \rho_s \dfrac{\partial^2 \mathbf{d}}{\partial t^2} - \nabla \cdot \mathbf{P}(\mathbf{d}, T_a(\mathbf{s})) = \boldsymbol{0}, \\ \mathbf{P}(\mathbf{d}, T_a(\mathbf{s}))\mathbf{N} + \mathbf{K}^{epi}\mathbf{d} + \mathbf{C}^{epi}\dfrac{\partial \mathbf{d}}{\partial t} = \boldsymbol{0} & \text{on } \Gamma_0^{epi} \times (0, T), \\ \mathbf{P}(\mathbf{d}, T_a(\mathbf{s}))\mathbf{N} = p_{LV}(t) \, |J\mathbf{F}^{-T}\mathbf{N}| \, \mathbf{v}^{base} & \text{on } \Gamma_0^{base} \times (0, T), \\ \mathbf{P}(\mathbf{d}, T_a(\mathbf{s}))\mathbf{N} = -p_{LV}(t) \, J\mathbf{F}^{-T}\mathbf{N} & \text{on } \Gamma_0^{endo} \times (0, T), \end{cases} \tag{2d}$$

in $\Omega_0 \times (0, T)$, with $\mathbf{d} = \mathbf{d}_0$ and $\dfrac{\partial \mathbf{d}}{\partial t} = \dot{\mathbf{d}}_0$ in $\Omega_0$ at time $t = 0$.

$$(\mathscr{C}) \quad \frac{d\boldsymbol{c}_1(t)}{dt} = \widetilde{\boldsymbol{D}}(t, \boldsymbol{c}_1(t), p_{\mathrm{LV}}(t)), \tag{2e}$$

for $t \in (0, T)$, with $\boldsymbol{c}_1(0) = \boldsymbol{c}_{1,0}$.

$$(\mathscr{V}) \quad V_{\mathrm{LV}}^{\mathrm{0D}}(\boldsymbol{c}_1(t)) = V_{\mathrm{LV}}^{\mathrm{3D}}(\mathbf{d}(t)), \tag{2f}$$

for $t \in (0, T)$.

Hereafter we will denote the pair $(\mathscr{E})$–$(\mathscr{I})$ as *cardiac electrophysiology*. In the following sections, we will detail the different core models, along with the meaning of all the variables, and their coupling.

## 2.1. Electrophysiology $(\mathscr{E})$–$(\mathscr{I})$

We model the propagation of transmembrane potential $u$ with the monodomain equation $(\mathscr{E})$, a diffusion-reaction PDE describing the electric activity of cardiac muscle cells [53–56]. We couple the monodomain equation with the ten Tusscher-Panfilov ionic model, that we denote by TTP06, due to our focus on the physiological ventricular activity [59]. This model enables to describe the dynamics of ionic fluxes across the cell membrane in an accurate and detailed manner, which is essential for electromechanical coupling [66].

In the electrophysiological model $(\mathscr{E})$–$(\mathscr{I})$, $C_{\mathrm{m}}$ is the total membrane capacitance and $\chi_{\mathrm{m}}$ is the area of cell membrane per tissue volume. The vector $\boldsymbol{w} = \{w_1, w_2, ..., w_{n_{\boldsymbol{w}}}\}$ expresses $n_{\boldsymbol{w}}$ recovery (or gating) variables, which play the role of density functions and model the fraction of open ionic channels across the membrane of a single cell. The vector $\boldsymbol{z} = \{z_1, z_2, ..., z_{n_{\boldsymbol{z}}}\}$ defines $n_{\boldsymbol{z}}$ concentration variables of specific ionic species (among which intracellular calcium ions concentration $[\mathrm{Ca}^{2+}]_{\mathrm{i}}$, which plays a crucial role in the mechanical activation). $\boldsymbol{H}$ and $\boldsymbol{G}$ are suitably defined vector-valued functions, depending on the specific ionic model at hand.

The transmission of the electrical potential $u$ through the so-called gap junctions is described in $(\mathscr{E})$ by means of the diffusion term $\nabla \cdot (J\mathbf{F}^{-1}\boldsymbol{D}_{\mathrm{M}}\mathbf{F}^{-T}\nabla u)$. In this term, $\boldsymbol{D}_{\mathrm{M}}$ is the diffusion tensor in the deformed configuration (material coordinates). To account for the dependence of the electrical properties on the tissue on its stretch (mechano-electrical feedback, see e.g. [53,54]), we introduce the deformation gradient tensor $\mathbf{F} = \mathbf{I} + \nabla\mathbf{d}$, where $\mathbf{d}$ denotes the displacement of the myocardium, and the deformation Jacobian $J = \det(\mathbf{F})$, and we compute the pull-back of $\boldsymbol{D}_{\mathrm{M}}$ in the reference configuration.

The applied current $\mathcal{I}_{\mathrm{app}}(t)$ mimics the effect of the Purkinje network [67–69], which we do not model in this context, by triggering the action potential at specific locations of the myocardium. The ionic current $\mathcal{I}_{\mathrm{ion}}(u, \boldsymbol{w}, \boldsymbol{z})$ models the multiscale effects from the cellular level up to the tissue one and strictly depends on the selected ionic model. A no-flux (Neumann) boundary condition represents an electrically isolated domain.

To reduce the number of parameters, we rescale the first equation in $(\mathscr{E})$ by $C_{\mathrm{m}}^{-1}\chi_{\mathrm{m}}^{-1}$, yielding:

$$J\left[\frac{\partial u}{\partial t} + \widetilde{\mathcal{I}}_{\mathrm{ion}}(u, \boldsymbol{w}, \boldsymbol{z})\right] = \nabla \cdot (J\mathbf{F}^{-1}\widetilde{\boldsymbol{D}}_{\mathrm{M}}\mathbf{F}^{-T}\nabla u) + J\widetilde{\mathcal{I}}_{\mathrm{app}}(t), \tag{3}$$

where $\widetilde{\mathcal{I}}_{\mathrm{ion}} := C_{\mathrm{m}}^{-1}\mathcal{I}_{\mathrm{ion}}$, $\widetilde{\boldsymbol{D}}_{\mathrm{M}} = C_{\mathrm{m}}^{-1}\chi_{\mathrm{m}}^{-1}\boldsymbol{D}_{\mathrm{M}}$ and $\widetilde{\mathcal{I}}_{\mathrm{app}} := C_{\mathrm{m}}^{-1}\mathcal{I}_{\mathrm{app}}$. We formulate the diffusion tensor as follows:

$$\boldsymbol{D}_{\mathrm{M}} = \sigma_{\mathrm{l}}\frac{\mathbf{F}\mathbf{f}_0 \otimes \mathbf{F}\mathbf{f}_0}{||\mathbf{F}\mathbf{f}_0||^2} + \sigma_{\mathrm{t}}\frac{\mathbf{F}\mathbf{s}_0 \otimes \mathbf{F}\mathbf{s}_0}{||\mathbf{F}\mathbf{s}_0||^2} + \sigma_{\mathrm{n}}\frac{\mathbf{F}\mathbf{n}_0 \otimes \mathbf{F}\mathbf{n}_0}{||\mathbf{F}\mathbf{n}_0||^2},$$

being $\mathbf{f}_0$ the vector field expressing the fiber direction, $\mathbf{s}_0$ the vector field containing the sheet normal direction, $\mathbf{n}_0$ the vector field that indicates the crossfiber direction, and $\sigma_{\mathrm{l}}, \sigma_{\mathrm{t}}, \sigma_{\mathrm{n}} \in \mathbb{R}^+$ longitudinal, transversal and normal conductivities, respectively [53,70]. $\mathbf{f}_0$, $\mathbf{s}_0$ and $\mathbf{n}_0$ account for the anisotropic properties of the cardiac tissue. This local orthonormal coordinate system defined at each point of the computational domain $\Omega_0$ can be generated using rule-based algorithms [71–73] and has a significant role in the electromechanical framework [74].

## 2.2. Active force generation $(\mathscr{A})$

Heart contraction is the result of mechano-chemical interactions among the contractile proteins actin and myosin, taking place at the scale of the sarcomeres, the fundamental contractile unit of the cardiac muscle [1,25,35,60,75]. To model such complex mechanisms, we consider the model that we proposed in [32], henceforth denoted as RDQ18 model. This model is based on a biophysically detailed description of the sarcomeric proteins with an explicit representation of the cooperative nearest-neighboring interactions, responsible for the high sensitivity of the cardiac contractile apparatus to changes in calcium concentration, which is one of the ionic species modelled by the TTP06 ionic model. Thanks to the spatially-explicit representation of the sarcomere filaments, the RDQ18 model also incorporates the feedback of the sarcomere shortening, resulting from the muscle contraction, on the force generation mechanism itself. This is of outmost importance since the regulation due to the sarcomere length ($SL$) constitutes the microscopical basis of the well-known Frank-Starling mechanism at the macroscale level; in practice, higher end-diastolic volumes translate into higher stroke volumes [1].

The RDQ18 model is a system of ODEs in the form of $(\mathscr{A})$, where the vector $\mathbf{s}$ collects the variables of the RDQ18 model and where $\boldsymbol{K}$ is a suitable function defined in [32] (we remark that $\boldsymbol{K}$ does not involve derivatives of $\mathbf{s}$ with respect to the

spatial variable). Within a multiscale framework, the RDQ18 model is ideally set at every point of the computational domain $\Omega_0$. The input variable $[\mathrm{Ca}^{2+}]_i$ is provided by the TTP06 ionic model in each point of the domain, while $SL$ is provided by the solution of the mechanical model, as we will explain later in Sec. 2.3.

The output of the RDQ18 model is the permissivity $P \in [0, 1]$, obtained as a function of the states **s** (i.e. $P = G(\mathbf{s})$, where $G$ is a linear function defined in [32]). The permissivity represents the fraction of contractile units being in the force-generating state. Hence, the effective active tension is given by $T_a = T_a^{\max} P$, where $T_a^{\max}$ denotes the tension generated when all the contractile units are generating force (i.e. for $P = 1$).

The RDQ18 model accurately describes the microscopic force generation mechanisms. This accuracy results in a higher computational cost compared to phenomenological models typically used for multiscale simulations (see e.g. [26,27]). To overcome this issue, in the multiscale model of electromechanics we take advantage of the model based on Artificial Neural Networks (ANNs) presented in [33]. This model is a fast surrogate of the RDQ18 model (high-fidelity model), learned from a collection of pre-computed simulations obtained with the RDQ18 model itself, thanks to the Machine Learning algorithm that we proposed in [76]. Such reduced-order model is written in the same form of ($\mathscr{A}$). However, the state vector **s** of ANN-based model only contains two variables, instead of the more than 2'000 variables of the high fidelity model. This significantly reduces the computational costs associated with its numerical approximation (both in terms of CPU time and memory storage), at the price of only a small approximation, as the overall relative error between the results of the high-fidelity and of the reduced-order models is of the order of $10^{-3}$ [33]. In this way we obtain an excellent trade-off between computational cost and biophysical accuracy of the results.

## 2.3. Active and passive mechanics ($\mathscr{M}$)

We describe the dynamics of the tissue displacement **d** by the momentum conservation equation ($\mathscr{M}$) (see e.g. [65]). The Piola-Kirchhoff stress tensor $\mathbf{P} = \mathbf{P}(\mathbf{d}, T_a)$ incorporates both passive and active mechanics of the tissue. Under the hyperelasticity assumption, once the strain energy density function $\mathcal{W} : \mathrm{Lin}^+ \to \mathbb{R}$ is introduced, the passive part of the Piola-Kirchhoff stress tensor is obtained as $\frac{\partial}{\partial \mathbf{F}} \mathcal{W}(\mathbf{F})$. In conclusion, the full Piola-Kirchhoff tensor reads:

$$\mathbf{P}(\mathbf{d}, T_a) = \frac{\partial \mathcal{W}(\mathbf{F})}{\partial \mathbf{F}} + T_a \frac{\mathbf{F}\mathbf{f}_0 \otimes \mathbf{f}_0}{\sqrt{\mathcal{I}_{4f}}}, \tag{4}$$

where the first term stands as the passive part, while the latter as the active one of the tensor **P**, and where $T_a$ denotes the active tension, provided the force generation model of Sec. 2.2. $\mathcal{I}_{4f} = \mathbf{F}\mathbf{f}_0 \cdot \mathbf{F}\mathbf{f}_0$ is a measure of the tissue stretch along the fiber direction.

Several models have been proposed in literature to describe the anisotropic nature of the cardiac muscle tissue. In this paper, we consider the Guccione strain energy density function [64,77], that reads $\mathcal{W}(\mathbf{F}) = \frac{C}{2}(e^Q - 1)$, with

$$Q = b_{\mathrm{ff}} E_{\mathrm{ff}}^2 + b_{\mathrm{ss}} E_{\mathrm{ss}}^2 + b_{\mathrm{nn}} E_{\mathrm{nn}}^2 + b_{\mathrm{fs}}\left(E_{\mathrm{fs}}^2 + E_{\mathrm{sf}}^2\right) + b_{\mathrm{fn}}\left(E_{\mathrm{fn}}^2 + E_{\mathrm{nf}}^2\right) + b_{\mathrm{sn}}\left(E_{\mathrm{sn}}^2 + E_{\mathrm{ns}}^2\right), \tag{5}$$

where $E_{ab} = \mathbf{E}\boldsymbol{a}_0 \cdot \boldsymbol{b}_0$ for $a, b \in \{f, s, n\}$ are the entries of $\mathbf{E} = \frac{1}{2}(\mathbf{C} - \mathbf{I})$, i.e. the Green-Lagrange strain energy tensor, being $\mathbf{C} = \mathbf{F}^T \mathbf{F}$ the right Cauchy-Green deformation tensor. We consider a further term, defined as $\mathcal{W}_{\mathrm{vol}}(J) = \frac{B}{2}(J - 1)\log(J)$, convex in $J$ and such that $J = 1$ is the global minimum, which penalizes large variations of volume, thus realizing a (weakly) incompressible constraint [78–80]; $B \in \mathbb{R}^+$ represents the bulk modulus.

To model the interaction of the left ventricle with the pericardium [14,15,13,8], we impose at the epicardial boundary $\Gamma_0^{\mathrm{epi}}$ the generalized Robin boundary condition $\mathbf{PN} + \mathbf{K}^{\mathrm{epi}}\mathbf{d} + \mathbf{C}^{\mathrm{epi}}\frac{\partial \mathbf{d}}{\partial t} = \mathbf{0}$, by defining the following tensors

$$\mathbf{K}^{\mathrm{epi}} = K_\perp^{\mathrm{epi}}(\mathbf{N} \otimes \mathbf{N}) + K_\parallel^{\mathrm{epi}}(\mathbf{I} - \mathbf{N} \otimes \mathbf{N}),$$

$$\mathbf{C}^{\mathrm{epi}} = C_\perp^{\mathrm{epi}}(\mathbf{N} \otimes \mathbf{N}) + C_\parallel^{\mathrm{epi}}(\mathbf{I} - \mathbf{N} \otimes \mathbf{N}),$$

where the constants $K_\perp^{\mathrm{epi}}, K_\parallel^{\mathrm{epi}}, C_\perp^{\mathrm{epi}}, C_\parallel^{\mathrm{epi}} \in \mathbb{R}^+$ are local values of stiffness and viscosity of the epicardial tissue in the normal or tangential directions, respectively. The tangential components are aimed at constraining the rigid rotations of the ventricle around the apico-basal axis, with respect to which the structure would be under-constrained. They surrogate the action of the right ventricle, main veins and arteries, which oppose the rigid rotations of the left ventricle while allowing torsion. In our experience, coefficients in the tangential direction one order of magnitude smaller than the normal direction are sufficient to constrain rigid rotations without affecting the twisting (see Appendix A). At the base $\Gamma_0^{\mathrm{base}}$, we set the energy-consistent boundary condition $\mathbf{PN} = p_{\mathrm{LV}}(t)|J\mathbf{F}^{-T}\mathbf{N}|\mathbf{v}^{\mathrm{base}}$, originally proposed in [33], that provides an explicit expression for the stresses located at the artificial boundary $\Gamma_0^{\mathrm{base}}$, where we have defined the vector

$$\mathbf{v}^{\mathrm{base}} = \frac{\int_{\Gamma_0^{\mathrm{endo}}} J\mathbf{F}^{-T}\mathbf{N}d\Gamma_0}{\int_{\Gamma_0^{\mathrm{base}}} |J\mathbf{F}^{-T}\mathbf{N}|d\Gamma_0}.$$

As we later show (Sec. 3.2), this formulation allows to straightforwardly couple the 3D mechanical model with a 0D model of the whole circulation in an energetically consistent manner. Finally, at the endocardium $\Gamma_0^{\text{endo}}$, the boundary condition $\mathbf{PN} = -p_{\text{LV}}(t) J\mathbf{F}^{-T}\mathbf{N}$ accounts for the pressure $p_{\text{LV}}(t)$ exerted by the blood contained in the ventricular chamber, modeled through 0D closed-loop circulation model.

As anticipated, the mechanical model ($\mathscr{M}$) has a feedback on the force generation model of ($\mathscr{A}$), as $\mathbf{d}$ determines the local sarcomere length $SL$. More precisely, since sarcomeres are aligned with the muscle fibers $\mathbf{f}_0$, the local sarcomere length $SL$ is given as $SL = SL_0\sqrt{\mathcal{I}_{4f}}$, where $SL_0$ denotes the sarcomere length at rest.

### 2.4. Blood circulation ($\mathscr{C}$)

To model the hemodynamics of the whole circulatory network, we propose a lumped-parameter closed-loop model, inspired by previous models available in literature [49,50]. Systemic and pulmonary circulations are modeled with resistance-inductance-capacitance (RLC) circuits, one for the arterial part and the other one for the venous part. The four chambers are modeled by time-varying elastance elements, whereas the four valves are represented as non-ideal diodes. Our 0D closed-loop circulation model reads:

$$
\begin{cases}
\dfrac{dV_{\text{LA}}(t)}{dt} = Q_{\text{VEN}}^{\text{PUL}}(t) - Q_{\text{MV}}(t), \qquad \dfrac{dV_{\text{LV}}(t)}{dt} = Q_{\text{MV}}(t) - Q_{\text{AV}}(t), & \text{(a)} \\[2mm]
\dfrac{dV_{\text{RA}}(t)}{dt} = Q_{\text{VEN}}^{\text{SYS}}(t) - Q_{\text{TV}}(t), \qquad \dfrac{dV_{\text{RV}}(t)}{dt} = Q_{\text{TV}}(t) - Q_{\text{PV}}(t), & \text{(b)} \\[2mm]
C_{\text{AR}}^{\text{SYS}}\dfrac{dp_{\text{AR}}^{\text{SYS}}(t)}{dt} = Q_{\text{AV}}(t) - Q_{\text{AR}}^{\text{SYS}}(t), \;\; C_{\text{VEN}}^{\text{SYS}}\dfrac{dp_{\text{VEN}}^{\text{SYS}}(t)}{dt} = Q_{\text{AR}}^{\text{SYS}}(t) - Q_{\text{VEN}}^{\text{SYS}}(t), & \text{(c)} \\[2mm]
C_{\text{AR}}^{\text{PUL}}\dfrac{dp_{\text{AR}}^{\text{PUL}}(t)}{dt} = Q_{\text{PV}}(t) - Q_{\text{AR}}^{\text{PUL}}(t), \;\; C_{\text{VEN}}^{\text{PUL}}\dfrac{dp_{\text{VEN}}^{\text{PUL}}(t)}{dt} = Q_{\text{AR}}^{\text{PUL}}(t) - Q_{\text{VEN}}^{\text{PUL}}(t), & \text{(d)} \\[2mm]
\dfrac{L_{\text{AR}}^{\text{SYS}}}{R_{\text{AR}}^{\text{SYS}}}\dfrac{dQ_{\text{AR}}^{\text{SYS}}(t)}{dt} = -Q_{\text{AR}}^{\text{SYS}}(t) - \dfrac{p_{\text{VEN}}^{\text{SYS}}(t) - p_{\text{AR}}^{\text{SYS}}(t)}{R_{\text{AR}}^{\text{SYS}}}, & \text{(e)} \\[2mm]
\dfrac{L_{\text{VEN}}^{\text{SYS}}}{R_{\text{VEN}}^{\text{SYS}}}\dfrac{dQ_{\text{VEN}}^{\text{SYS}}(t)}{dt} = -Q_{\text{VEN}}^{\text{SYS}}(t) - \dfrac{p_{\text{RA}}(t) - p_{\text{VEN}}^{\text{SYS}}(t)}{R_{\text{VEN}}^{\text{SYS}}}, & \text{(f)} \\[2mm]
\dfrac{L_{\text{AR}}^{\text{PUL}}}{R_{\text{AR}}^{\text{PUL}}}\dfrac{dQ_{\text{AR}}^{\text{PUL}}(t)}{dt} = -Q_{\text{AR}}^{\text{PUL}}(t) - \dfrac{p_{\text{VEN}}^{\text{PUL}}(t) - p_{\text{AR}}^{\text{PUL}}(t)}{R_{\text{AR}}^{\text{PUL}}}, & \text{(g)} \\[2mm]
\dfrac{L_{\text{VEN}}^{\text{PUL}}}{R_{\text{VEN}}^{\text{PUL}}}\dfrac{dQ_{\text{VEN}}^{\text{PUL}}(t)}{dt} = -Q_{\text{VEN}}^{\text{PUL}}(t) - \dfrac{p_{\text{LA}}(t) - p_{\text{VEN}}^{\text{PUL}}(t)}{R_{\text{VEN}}^{\text{PUL}}}, & \text{(h)}
\end{cases}
\tag{6}
$$

with $t \in (0, T)$, where:

$$p_{\text{LV}}(t) = p_{\text{EX}}(t) + E_{\text{LV}}(t)\left(V_{\text{LV}}(t) - V_{0,\text{LV}}\right), \tag{7a}$$

$$p_{\text{LA}}(t) = p_{\text{EX}}(t) + E_{\text{LA}}(t)\left(V_{\text{LA}}(t) - V_{0,\text{LA}}\right), \tag{7b}$$

$$p_{\text{RV}}(t) = p_{\text{EX}}(t) + E_{\text{RV}}(t)\left(V_{\text{RV}}(t) - V_{0,\text{RV}}\right), \tag{7c}$$

$$p_{\text{RA}}(t) = p_{\text{EX}}(t) + E_{\text{RA}}(t)\left(V_{\text{RA}}(t) - V_{0,\text{RA}}\right), \tag{7d}$$

$$Q_{\text{MV}}(t) = \frac{p_{\text{LA}}(t) - p_{\text{LV}}(t)}{R_{\text{MV}}(p_{\text{LA}}(t), p_{\text{LV}}(t))}, \qquad Q_{\text{AV}}(t) = \frac{p_{\text{LV}}(t) - p_{\text{AR}}^{\text{SYS}}(t)}{R_{\text{AV}}(p_{\text{LV}}(t), p_{\text{AR}}^{\text{SYS}}(t))}, \tag{7e}$$

$$Q_{\text{TV}}(t) = \frac{p_{\text{RA}}(t) - p_{\text{RV}}(t)}{R_{\text{TV}}(p_{\text{RA}}(t), p_{\text{RV}}(t))}, \qquad Q_{\text{PV}}(t) = \frac{p_{\text{RV}}(t) - p_{\text{AR}}^{\text{PUL}}(t)}{R_{\text{PV}}(p_{\text{RV}}(t), p_{\text{AR}}^{\text{PUL}}(t))}, \tag{7f}$$

with $t \in (0, T)$. In this model, $p_{\text{LA}}(t)$, $p_{\text{RA}}(t)$, $p_{\text{LV}}(t)$, $p_{\text{RV}}(t)$, $V_{\text{LA}}(t)$, $V_{\text{RA}}(t)$, $V_{\text{LV}}(t)$ and $V_{\text{RV}}(t)$ refer to pressures and volumes in left atrium, right atrium, left ventricle and right ventricle, respectively. The variables $Q_{\text{MV}}(t)$, $Q_{\text{AV}}(t)$, $Q_{\text{TV}}(t)$ and $Q_{\text{PV}}(t)$ indicate the flow rates through mitral, aortic, tricuspid and pulmonary valves, respectively. Moreover, $p_{\text{AR}}^{\text{SYS}}(t)$, $Q_{\text{AR}}^{\text{SYS}}(t)$, $p_{\text{VEN}}^{\text{SYS}}(t)$ and $Q_{\text{VEN}}^{\text{SYS}}(t)$ express pressures and flow rates of the systemic circulation (arterial and venous). Similarly, $p_{\text{AR}}^{\text{PUL}}(t)$, $Q_{\text{AR}}^{\text{PUL}}(t)$, $p_{\text{VEN}}^{\text{PUL}}(t)$ and $Q_{\text{VEN}}^{\text{PUL}}(t)$ define pressures and flow rates of the pulmonary circulation (arterial and venous). $p_{\text{EX}}(t)$ represents the pressure exerted outside the heart by the surrounding organs and respiration. In this paper, we set for simplicity $p_{\text{EX}}(t) \equiv 0$. We remark that, in case $p_{\text{EX}}(t) \neq 0$, the pericardium boundary conditions could be modified accordingly to account for $p_{\text{EX}}(t) \neq 0$. Time varying $E_{\text{LA}}(t)$, $E_{\text{LV}}(t)$, $E_{\text{RA}}(t)$, $E_{\text{RV}}(t)$ are the analytically prescribed elastances of the four cardiac

chambers calibrated on a physiological basis, with values ranging from $E_{\text{LA}}^{\text{pass}}$, $E_{\text{LV}}^{\text{pass}}$, $E_{\text{RA}}^{\text{pass}}$, $E_{\text{RV}}^{\text{pass}}$ – when the chambers are at rest – to $(E_{\text{LA}}^{\text{pass}} + E_{\text{LA}}^{\text{act,max}})$, $(E_{\text{LV}}^{\text{pass}} + E_{\text{LV}}^{\text{act,max}})$, $(E_{\text{RA}}^{\text{pass}} + E_{\text{RA}}^{\text{act,max}})$, $(E_{\text{RV}}^{\text{pass}} + E_{\text{RV}}^{\text{act,max}})$ – when the chambers are fully contracted. More precisely, we consider the analytically prescribed activation transient

$$\phi(t, t_{\text{C}}, t_{\text{R}}, T_{\text{C}}, T_{\text{R}}) = \begin{cases} \dfrac{1}{2}\left[1 - \cos\left(\dfrac{\pi}{T_{\text{C}}}\,\text{mod}(t - t_{\text{C}}, T_{\text{HB}})\right)\right] & \text{if } 0 \leq \text{mod}(t - t_{\text{C}}, T_{\text{HB}}) < T_{\text{C}}, \\[3mm] \dfrac{1}{2}\left[1 + \cos\left(\dfrac{\pi}{T_{\text{R}}}\,\text{mod}(t - t_{\text{R}}, T_{\text{HB}})\right)\right] & \text{if } 0 \leq \text{mod}(t - t_{\text{R}}, T_{\text{HB}}) < T_{\text{R}}, \\[3mm] 0 & \text{otherwise,} \end{cases} \tag{8}$$

where $t_{\text{C}}$ and $t_{\text{R}}$ are the times in which contraction and relaxation begin, respectively; $T_{\text{C}}$ and $T_{\text{R}}$ are the durations of contraction and relaxation, respectively; $T_{\text{HB}}$ is the heartbeat period. Notice that $t_{\text{R}} = t_{\text{C}} + T_{\text{C}}$, for consistency. Then, we define the time-varying elastances of the four cardiac chambers as

$$E_{\text{i}}(t) = E_{\text{i}}^{\text{pass}} + E_{\text{i}}^{\text{act,max}}\phi(t, t_{\text{C}}^i, t_{\text{R}}^i, T_{\text{C}}^i, T_{\text{R}}^i), \qquad \text{for } i \in \{\text{LA, LV, RA, RV}\}. \tag{9}$$

Finally, $R_{\text{MV}}(p_1, p_2)$, $R_{\text{AV}}(p_1, p_2)$, $R_{\text{TV}}(p_1, p_2)$ and $R_{\text{PV}}(p_1, p_2)$ define the behavior of valves as diodes, according to the following relationship:

$$R_{\text{i}}(p_1, p_2) = \begin{cases} R_{\min}, & p_1 < p_2 \\ R_{\max}, & p_1 \geq p_2 \end{cases} \quad \text{for } i \in \{\text{MV, AV, TV, PV}\},$$

where $p_1$ and $p_2$ denote the pressures ahead and behind the valve leaflets with respect to the flow direction, whereas $R_{\min}$ and $R_{\max}$ are the minimum and maximum resistance of the valves. For an idealized valve, one would have $R_{\min} = 0$ and $R_{\max} = +\infty$ instead. By setting $R_{\min} > 0$, one has dissipation of mechanical energy taking place when the blood flows through the opened valve (see Sec. 3); we set $R_{\max} < +\infty$ sufficiently large so that blood leakage when the valve is closed is negligible.

Hereafter, for the sake of brevity, Eqs. (6)–(7) will be expressed in the following compact form:

$$\begin{cases} \dfrac{d\boldsymbol{c}_1(t)}{dt} = \boldsymbol{D}(t, \boldsymbol{c}_1(t), \boldsymbol{c}_2(t)) & t \in (0, T], \\[3mm] \boldsymbol{c}_2(t) = \boldsymbol{W}(t, \boldsymbol{c}_1(t)) & t \in [0, T], \\[2mm] \boldsymbol{c}_1(0) = \boldsymbol{c}_{1,0}, \end{cases} \tag{10}$$

where:

$$\boldsymbol{c}_1(t) = (V_{\text{LA}}(t), V_{\text{LV}}(t), V_{\text{RA}}(t), V_{\text{RV}}(t), p_{\text{AR}}^{\text{SYS}}(t), p_{\text{VEN}}^{\text{SYS}}(t), p_{\text{AR}}^{\text{PUL}}(t), p_{\text{VEN}}^{\text{PUL}}(t), Q_{\text{AR}}^{\text{SYS}}(t), Q_{\text{VEN}}^{\text{SYS}}(t), Q_{\text{AR}}^{\text{PUL}}(t), Q_{\text{VEN}}^{\text{PUL}}(t))^T,$$

$$\boldsymbol{c}_2(t) = (p_{\text{LV}}(t), p_{\text{LA}}(t), p_{\text{RV}}(t), p_{\text{RA}}(t), Q_{\text{MV}}(t), Q_{\text{AV}}(t), Q_{\text{TV}}(t), Q_{\text{PV}}(t))^T;$$

$\boldsymbol{D}(t, \boldsymbol{c}_1(t), \boldsymbol{c}_2(t))$ collects the whole r.h.s. of Eq. (6), while $\boldsymbol{c}_2(t) = \boldsymbol{W}(t, \boldsymbol{c}_1(t))$ stands as a compact notation for Eq. (7), rewritten in explicit form with respect to the variable $\boldsymbol{c}_2$.

### 2.5. 3D-0D coupling ($\mathscr{V}$)

In Eq. (10) each cardiac chamber is modeled as a time-varying elastance element, that is a 0D simplified model. In this paper, we employ this 0D circulation model in conjunction with the 3D left ventricular model given by $(\mathscr{E})$–$(\mathscr{I})$–$(\mathscr{A})$–$(\mathscr{M})$. With this goal, we remove from the circulation model the time-varying elastance element associated with the left ventricle, and we replace it with the 3D electromechanical model. Hence, the pressure-volume relationship between $p_{\text{LV}}$ and $V_{\text{LV}}$ is no longer prescribed by Eq. (7a), but by the resolution of the 3D electromechanical model. The resulting 3D–0D coupled model (depicted in Fig. 2) must satisfy at each time $t \in (0, T)$ the volume-consistency coupling condition $V_{\text{LV}}^{\text{0D}}(\boldsymbol{c}_1(t)) = V_{\text{LV}}^{\text{3D}}(\mathbf{d}(t))$, that we denote by $(\mathscr{V})$, where $V_{\text{LV}}^{\text{0D}}(\boldsymbol{c}_1(t)) = V_{\text{LV}}(t)$ represents the left ventricle volume in the 0D circulation model. $V_{\text{LV}}^{\text{3D}}(\mathbf{d}(t))$ represents the left ventricle volume in the 3D model and it is computed as:

$$V_{\text{LV}}^{\text{3D}}(\mathbf{d}(t)) = \int_{\Gamma_0^{\text{endo}}} J(t)\,((\mathbf{h} \otimes \mathbf{h})\,(\mathbf{x} + \mathbf{d}(t) - \mathbf{b})) \cdot \mathbf{F}^{-T}(t)\mathbf{N}\,d\Gamma_0,$$

where $\mathbf{h}$ is a vector orthogonal to the left ventricle centerline (i.e. lying on the left ventricle base) [81]. Subtracting to the space coordinate $\mathbf{x} + \mathbf{d}(t)$ that of a point $\mathbf{b}$, lying inside the left ventricle, improves the accuracy of the formula when the ventricular base changes its orientation.

Having introduced an additional scalar equation, i.e. $(\mathscr{V})$, we expect an additional unknown: it is in fact $p_{\text{LV}}$, which is not determined by Eq. (7a) anymore. Rather, it acts as a Lagrange multiplier enforcing the constraint $(\mathscr{V})$.
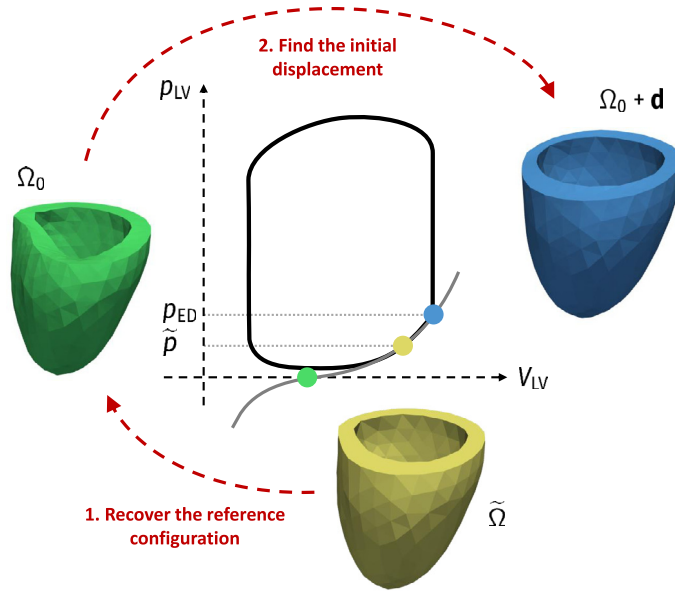
**Fig. 3.** Sketch of the strategy used to initialize the simulation. The gray line represents the so-called Klotz curve [82], that is the pressure-volume relationship of the relaxed ventricle. The black line represents the pressure-volume loop of the left ventricle.

Hence, we define the "reduced" vector $\widetilde{\boldsymbol{c}}_2$ such that $\boldsymbol{c}_2^T = (p_{\text{LV}}, \widetilde{\boldsymbol{c}}_2^T)$, so that we can rewrite Eqs. (7a)–(7f) as $\widetilde{\boldsymbol{c}}_2(t) = \widetilde{\boldsymbol{W}}(t, \boldsymbol{c}_1(t), p_{\text{LV}}(t))$. This allows to write the "reduced" version of Eq. (10) as ($\mathscr{C}$) where we have defined

$$\widetilde{\boldsymbol{D}}(t, \boldsymbol{c}_1, p_{\text{LV}}) := \boldsymbol{D}\left(t, \boldsymbol{c}_1, \begin{pmatrix} p_{\text{LV}} \\ \widetilde{\boldsymbol{W}}(t, \boldsymbol{c}_1, p_{\text{LV}}) \end{pmatrix}\right).$$

In conclusion, we obtain the coupled 3D-0D model reported in Eq. (2). We remark that the number of equations balances with the number of unknowns defined in (1): we have $1 + n_w + n_z + n_s + 3$ unknowns (respectively, equations) defined in $\Omega_0 \times (0, T)$ and $n_{\boldsymbol{c}} + 1$ unknowns (respectively, equations) defined in $(0, T)$.

### 2.6. Reference configuration and initial displacement

In the mechanical model ($\mathscr{M}$), the stress-strain relationship (4) is referred to the natural stress-free configuration $\Omega_0$. However, the cardiac chambers are never unloaded during the cardiac cycle.

Let us denote by $\widetilde{\Omega}$ a medical image to generate the LV. This configuration presents residual stresses, since an internal pressure $p_{\text{LV}} \neq 0$ is acting at every stage of the heartbeat. Therefore, in the preprocessing stage, we need to recover the reference configuration $\Omega_0$ from $\widetilde{\Omega}$.

Our strategy to initialize the numerical simulation is sketched in Fig. 3. As a first step, starting from the geometry acquired from medical imaging $\widetilde{\Omega}$, we recover the stress-free reference configuration $\Omega_0$, by virtually deflating the left ventricle, previously subject to an internal pressure $\widetilde{p}$. Then, as a second step, we inflate the left ventricle again, by applying the end diastolic pressure $p_{\text{ED}}$ at the endocardium. The last part of diastole is chosen for the following reasons:

- The diastolic phase is typically captured in the clinical practice of cardiac imaging.
- As it will be shown in Sect. 2.6.1, we consider a quasi-static approximation of the mechanical problem, which is more legitimate during the last part of diastole, when ventricular filling has slowed before atrial contraction.
- It is less challenging to deflate the left ventricle from a low pressure regime rather than starting from the systolic phase (i.e. mid to high pressure regime).

In the next sections we give the mathematical details behind the steps reported in Fig. 3.

### 2.6.1. Recovering the reference configuration

We assume that the configuration $\widetilde{\Omega}$ occurs during diastole, when the left ventricle is loaded by a pressure $p_{\text{LV}} = \widetilde{p}$ and only a residual active tension $T_{\text{a}} = \widetilde{T}_{\text{a}} > 0$ acts. By adopting a quasi-static assumption (motivated by the slow movement of the myocardium during the final part of diastole), the tissue displacement is given by the solution of the following differential problem: find $\boldsymbol{d}$ such that

$$\begin{cases} \nabla \cdot \mathbf{P}(\mathbf{d}, T_a) = \mathbf{0} & \text{in } \Omega_0, \\ \mathbf{P}(\mathbf{d}, T_a)\mathbf{N} + \mathbf{K}^{\text{epi}}\mathbf{d} = \mathbf{0} & \text{on } \Gamma_0^{\text{epi}}, \\ \mathbf{P}(\mathbf{d}, T_a)\mathbf{N} = p_{\text{LV}} \,|\, J\mathbf{F}^{-T}\mathbf{N}|\, \mathbf{v}^{\text{base}} & \text{on } \Gamma_0^{\text{base}}, \\ \mathbf{P}(\mathbf{d}, T_a)\mathbf{N} = -p_{\text{LV}} \, J\mathbf{F}^{-T}\mathbf{N} & \text{on } \Gamma_0^{\text{endo}}. \end{cases} \tag{11}$$

Eq. (11) is derived from $(\mathcal{M})$ by setting to zero the time-dependent terms. Thus, to recover the coordinate $\mathbf{x}_0$ of the configuration $\Omega_0$ we need to solve the following inverse problem: find the domain $\Omega_0$ such that, if we displace $\mathbf{x}_0$ by the solution $\mathbf{d} = \mathbf{d}_{\text{eq}}(\mathbf{x}_0, p_{\text{LV}}, T_a)$ of Eq. (11) obtained for $p_{\text{LV}} = \widetilde{p}$ and $T_a = \widetilde{T}_a$, we get the coordinate $\widetilde{\mathbf{x}}$ of the domain $\widetilde{\Omega}$ (i.e. $\widetilde{\mathbf{x}} = \mathbf{x}_0 + \mathbf{d}$). In Sec. 5 we present an algorithm for its numerical solution.

### 2.6.2. Finding the initial displacement

After the recovery of the reference configuration $\Omega_0$, we set $p_{\text{LV}} = p_{\text{ED}}$. Then, we solve again Eq. (11). In this manner, we obtain the end-diastolic configuration of the LV, i.e. $\mathbf{d}_{\text{ED}}$. Hence, we set $\mathbf{d}_0 = \mathbf{d}_{\text{ED}}$ in $(\mathcal{M})$.

## 3. On the balance of mechanical energy of the electromechanical model

We derive a balance of the mechanical energy for the whole cardiovascular system. In particular, we analyze how mechanical energy is injected, dissipated and transferred in the different compartments of the heart and in both systemic and pulmonary circulation. First, in Sec. 3.1, we consider the 0D closed-loop circulation model $(\mathscr{C})$ introduced in Sec. 2.4. Then, in Sec. 3.2 we focus on the coupled 3D-0D model $(\mathcal{M})$–$(\mathcal{V})$–$(\mathscr{C})$.

### 3.1. Energy balance for the 0D model

To define the terms associated with the work performed by the cardiac chambers, we write $E_i(t) = E_i^{\text{pass}} + E_i^{\text{act}}(t)$ (for $i \in \{\text{LA, LV, RA, RV}\}$), where $E_i^{\text{pass}}$ is the passive elastance of the tissue (i.e. the elastance when the tissue is not activated) and $E_i^{\text{act}}$ is instead the active component of the elastance.

**Definition 1.** We define the total mechanical energy of the whole 0D circulation model as

$$\begin{aligned} \mathcal{M}(t) = {} & \mathcal{E}_{\text{LA}}(t) + \mathcal{E}_{\text{LV}}(t) + \mathcal{E}_{\text{RA}}(t) + \mathcal{E}_{\text{RV}}(t) + \mathcal{E}_{\text{AR}}^{\text{SYS}}(t) + \mathcal{E}_{\text{VEN}}^{\text{SYS}}(t) + \mathcal{E}_{\text{AR}}^{\text{PUL}}(t) + \mathcal{E}_{\text{VEN}}^{\text{PUL}}(t) \\ & + \mathcal{K}_{\text{AR}}^{\text{SYS}}(t) + \mathcal{K}_{\text{VEN}}^{\text{SYS}}(t) + \mathcal{K}_{\text{AR}}^{\text{PUL}}(t) + \mathcal{K}_{\text{VEN}}^{\text{PUL}}(t), \end{aligned}$$

where, for $i \in \{\text{LA, LV, RA, RV}\}$, $j \in \{\text{AR, VEN}\}$ and $k \in \{\text{SYS, PUL}\}$:

- $\mathcal{E}_i(t) = \frac{1}{2} E_i^{\text{pass}} \left(V_i(t) - V_{0,i}\right)^2$ is the elastic energy stored by a cardiac chamber;
- $\mathcal{E}_j^k(t) = \frac{1}{2} C_j^k \left(p_j^k(t)\right)^2$ is the elastic energy stored in the vascular network, due to vessels compliance;
- $\mathcal{K}_j^k(t) = \frac{1}{2} L_j^k \left(Q_j^k(t)\right)^2$ is the kinetic energy related to the blood flow inertia.

We provide now a deeper explanation of the definition of $\mathcal{E}_j^k$. Let us consider, as an example, $\mathcal{E}_{\text{AR}}^{\text{SYS}}$. First, we notice that $Q_{\text{AV}}(t) - Q_{\text{AR}}^{\text{SYS}}(t)$ is the net blood flux passing through the arterial systemic network. Hence, by denoting with $V_{\text{AR}}^{\text{SYS}}(t)$ the blood volume stored in the arterial systemic network, we have:

$$\frac{dV_{\text{AR}}^{\text{SYS}}(t)}{dt} = Q_{\text{AV}}(t) - Q_{\text{AR}}^{\text{SYS}}(t).$$

By comparing the latter equation to the first equation of (6c) we get:

$$p_{\text{AR}}^{\text{SYS}}(t) = \frac{1}{C_{\text{AR}}^{\text{SYS}}} \left(V_{\text{AR}}^{\text{SYS}}(t) - V_{0,\text{AR}}^{\text{SYS}}\right),$$

where $V_{0,\text{AR}}^{\text{SYS}}$ is the blood volume stored within the arterial systemic network when the pressure is null. In conclusion, we have $\mathcal{E}_{\text{AR}}^{\text{SYS}}(t) = (2\,C_{\text{AR}}^{\text{SYS}})^{-1} \left(V_{\text{AR}}^{\text{SYS}}(t) - V_{0,\text{AR}}^{\text{SYS}}\right)^2$, where $1/C_{\text{AR}}^{\text{SYS}}$ is the arterial systemic network elastance (the inverse of the compliance), coherently with the definition of $\mathcal{E}_{\text{LA}}$.

**Definition 2.** We define the power generated by active contraction, due to ATP consumption occurring at the cellular level, as

$$\Pi^{\text{act}}(t) = \Pi_{\text{LA}}^{\text{act}}(t) + \Pi_{\text{LV}}^{\text{act}}(t) + \Pi_{\text{RA}}^{\text{act}}(t) + \Pi_{\text{RV}}^{\text{act}}(t),$$

where $\Pi_i^{act}(t) = -E_i^{act}(t)\left(V_i(t) - V_{0,i}\right)\frac{dV_i}{dt}(t)$ is the power exerted by the active contraction of a cardiac chamber (for $i \in \{LA, LV, RA, RV\}$).

**Definition 3.** We define the power dissipated within the 0D circulation model by viscous forces as the blood flows through the valves and the vascular network as

$$\Pi^{diss}(t) = \Pi_{MV}(t) + \Pi_{AV}(t) + \Pi_{TV}(t) + \Pi_{PV}(t) + \Pi_{AR}^{SYS}(t) + \Pi_{VEN}^{SYS}(t) + \Pi_{AR}^{PUL}(t) + \Pi_{VEN}^{PUL}(t),$$

where:

- the power dissipated by the blood flux through the cardiac valves:

$$\Pi_{MV}(t) = -\frac{(p_{LA}(t) - p_{LV}(t))^2}{R_{MV}(p_{LA}(t), p_{LV}(t))}, \qquad \Pi_{AV}(t) = -\frac{\left(p_{LV}(t) - p_{AR}^{SYS}(t)\right)^2}{R_{AV}(p_{LV}(t), p_{AR}^{SYS}(t))},$$

$$\Pi_{TV}(t) = -\frac{(p_{RA}(t) - p_{RV}(t))^2}{R_{TV}(p_{RA}(t), p_{RV}(t))}, \qquad \Pi_{PV}(t) = -\frac{\left(p_{RV}(t) - p_{AR}^{PUL}(t)\right)^2}{R_{PV}(p_{RV}(t), p_{AR}^{PUL}(t))}; \tag{12}$$

- $\Pi_j^k(t) = -R_j^k\left(Q_j^k(t)\right)^2$, that is the power dissipated by the arterial systemic network (for $j \in \{AR, VEN\}$ and $k \in \{SYS, PUL\}$).

We remark that all the terms in Eq. (12) are nonpositive.

**Definition 4.** We define the power due to the action of the external pressure $p_{EX}$ on the myocardium as

$$\Pi^{ex}(t) = \Pi_{LA}^{ex}(t) + \Pi_{LV}^{ex}(t) + \Pi_{RA}^{ex}(t) + \Pi_{RV}^{ex}(t),$$

where $\Pi_i^{ex}(t) = -p_{EX}(t)\frac{dV_i}{dt}(t)$ is the power exerted by the external pressure $p_{EX}(t)$ acting on a cardiac chamber (for $i \in \{LA, LV, RA, RV\}$).

We have the following result.

**Proposition 1.** *The solution of Eq. (10) for the whole 0D circulation model satisfies the energy balance*

$$\frac{d}{dt}\mathcal{M}(t) = \Pi^{act}(t) + \Pi^{diss}(t) + \Pi^{ex}(t), \tag{13}$$

*whose terms are defined in Definitions 1–4.*

**Proof.** To derive Eq. (13) we consider, as illustrative examples, a representative cardiac chamber, a cardiac valve and a vascular branch. In fact, similar calculations will apply to the other chambers, valves and vascular compartments.
*Energy balance of the cardiac chambers.* Let us consider for now the left atrium (LA). By multiplying Eq. (7b) by $\frac{dV_{LA}(t)}{dt}$ and thanks to Eq. (6a), we get:

$$p_{LA}(t)(Q_{VEN}^{PUL}(t) - Q_{MV}(t)) = \frac{d}{dt}\mathcal{E}_{LA}(t) - \Pi_{LA}^{act}(t) - \Pi_{LA}^{ex}(t). \tag{14}$$

*Energy balance of the cardiac valves.* From (7e) we obtain

$$(p_{LA}(t) - p_{LV}(t))Q_{MV}(t) = -\Pi_{MV}(t). \tag{15}$$

Similar considerations hold for the other valves.
*Energy balance of the peripheral blood reservoirs.* By multiplying the first equation of (6c) by $p_{AR}^{SYS}(t)$, we get:

$$p_{AR}^{SYS}(t)Q_{AV}(t) - p_{AR}^{SYS}(t)Q_{AR}^{SYS}(t) = \frac{d}{dt}\mathcal{E}_{AR}^{SYS}(t) \tag{16}$$

*Energy balance of the peripheral blood conducting system.* By multiplying (6e) by $R_{AR}^{SYS}Q_{AR}^{SYS}(t)$, we get:

$$p_{AR}^{SYS}(t)Q_{AR}^{SYS}(t) - p_{VEN}^{SYS}(t)Q_{AR}^{SYS}(t) = \frac{d}{dt}\mathcal{K}_{AR}^{SYS}(t) - \Pi_{AR}^{SYS}(t). \tag{17}$$

*Total balance.* By proceeding as above for the other cardiac chambers, valves and circulation systems, and summing up the resulting equations, we obtain Eq. (13). This completes the proof. □

Each of the four terms of Eq. (13) represents the result of the sum of different contributions, associated with the four chambers, the four valves and the different compartments of the vascular network (systemic and pulmonary, arterial and venous). The total work performed in a time interval $[0, T]$ is obtained by integrating the corresponding power over time, according to the following definition.

**Definition 5.** Let us consider a time horizon $T > 0$. The total work performed by active and dissipative forces in the time interval $[0, T]$ are defined as

$$W^{\text{act}} = \int_0^T \Pi^{\text{act}}(t)\,dt, \qquad W^{\text{diss}} = \int_0^T \Pi^{\text{diss}}(t)\,dt,$$

respectively.

When the heart rhythm has reached a periodic regime, it carries out its function alongside a cyclical path. In this case, the work balance of the following proposition holds.

**Proposition 2.** Let us suppose that $p_{\text{EX}}(t)$ is constant in time. Then, periodic solutions of Eq. (10) (i.e. with $\boldsymbol{c}_1(0) = \boldsymbol{c}_1(T)$) satisfy

$$W^{\text{act}} + W^{\text{diss}} = 0. \tag{18}$$

**Proof.** We integrate the energy balance of Eq. (13) over a cardiac cycle $[0, T]$. Thanks to the periodicity assumption, the contribution of the mechanical energy term $\mathcal{M}$ is null. Moreover, it is easy to show that the term $\Pi^{\text{ex}}(t)$ is conservative and hence its contribution over $[0, T]$ is also null. $\square$

Therefore, when the heart is functioning in a periodic regime, the work performed by the contraction of the four chambers balances the energy dissipated by the four valves and by the blood flux through the systemic and pulmonary circulations.

### 3.2. Energy balance of the 3D-0D coupled model

*Energy balance of the 3D left ventricle model*  By multiplying the first equation of $(\mathcal{M})$ by $\frac{\partial \mathbf{d}}{\partial t}$ and integrating over $\Omega_0$ we obtain:

$$\int_{\Omega_0} \rho_s \frac{\partial^2 \mathbf{d}}{\partial t^2} \cdot \frac{\partial \mathbf{d}}{\partial t} d\mathbf{x} + \int_{\Omega_0} \mathbf{P}(\mathbf{d}, T_a) : \nabla \left( \frac{\partial \mathbf{d}}{\partial t} \right) d\mathbf{x} = \int_{\partial \Omega_0} \mathbf{P}(\mathbf{d}, T_a) \mathbf{N} \cdot \frac{\partial \mathbf{d}}{\partial t} d\Gamma_0. \tag{19}$$

By substituting the boundary conditions of $(\mathcal{M})$ into (19), we obtain the following energy balance for the 3D left ventricle model:

$$\frac{d}{dt} \mathcal{K}_{\text{LV,3D}}(t) + \frac{d}{dt} \mathcal{E}_{\text{LV,3D}}(t) = \Pi^{\text{act}}_{\text{LV,3D}}(t) + \Pi^{\text{diss}}_{\text{LV,3D}}(t) + \Pi^{\text{press}}_{\text{LV,3D}}(t). \tag{20}$$

This relation reveals the mutual balance of:

- the kinetic energy associated with the motion of the LV:

$$\mathcal{K}_{\text{LV,3D}}(t) = \frac{1}{2} \int_{\Omega_0} \rho_s \left| \frac{\partial \mathbf{d}}{\partial t} \right|^2 d\mathbf{x};$$

- the elastic energy internally stored by the left ventricle muscle and by the elastic components of the surrounding tissues:

$$\mathcal{E}_{\text{LV,3D}}(t) = \int_{\Omega_0} \mathcal{W}(\mathbf{F}) d\mathbf{x} + \frac{1}{2} \int_{\Gamma_0^{\text{epi}}} \left[ K_\perp^{\text{epi}} |\mathbf{d} \cdot \mathbf{N}|^2 + K_\parallel^{\text{epi}} |(\mathbf{I} - \mathbf{N} \otimes \mathbf{N})\mathbf{d}|^2 \right] d\Gamma_0,$$

    where the displacement at the epicardium is split into the normal $|\mathbf{d} \cdot \mathbf{N}|$ and tangent $|(\mathbf{I} - \mathbf{N} \otimes \mathbf{N})\mathbf{d}|$ component;
- the power exerted by the active contraction of the LV:

$$\Pi^{\text{act}}_{\text{LV,3D}}(t) = - \int_{\Omega_0} T_a \frac{\mathbf{F}\mathbf{f}_0 \otimes \mathbf{f}_0}{\sqrt{\mathcal{I}_{4f}}} : \nabla \left( \frac{\partial \mathbf{d}}{\partial t} \right) d\mathbf{x};$$

- the power dissipated by the interaction with the pericardium:

$$\Pi_{\text{LV,3D}}^{\text{diss}}(t) = - \int_{\Gamma_0^{\text{epi}}} \left[ C_\perp^{\text{epi}} \left| \frac{\partial \mathbf{d}}{\partial t} \cdot \mathbf{N} \right|^2 + C_\parallel^{\text{epi}} \left| (\mathbf{I} - \mathbf{N} \otimes \mathbf{N}) \frac{\partial \mathbf{d}}{\partial t} \right|^2 \right] d\Gamma_0 \leq 0,$$

$\forall t$, which is a nonpositive term;

- the power exchanged with the blood contained in the left ventricle cavity, by means of the action of pressure $p_{\text{LV}}(t)$ on the endocardium:

$$\Pi_{\text{LV,3D}}^{\text{press}}(t) = p_{\text{LV}}(t) \left[ \int_{\Gamma_0^{\text{endo}}} J\mathbf{F}^{-T}\mathbf{N} \cdot \frac{\partial \mathbf{d}}{\partial t} \, d\Gamma_0 - \int_{\Gamma_0^{\text{base}}} |J\mathbf{F}^{-T}\mathbf{N}| \frac{\partial \mathbf{d}}{\partial t} \, d\Gamma_0 \cdot \mathbf{v}^{\text{base}} \right].$$

As in [33], the term in square brackets corresponds to the time derivative of the left ventricle volume, that is $\Pi_{\text{LV,3D}}^{\text{press}}(t) = p_{\text{LV}}(t) \frac{d}{dt} V_{\text{LV}}^{\text{3D}}(\mathbf{d}(t))$. Then, in virtue of the coupling condition ($\mathscr{V}$) and by Eq. (6a), we obtain $\Pi_{\text{LV,3D}}^{\text{press}}(t) = p_{\text{LV}}(t)(Q_{\text{MV}}(t) - Q_{\text{AV}}(t))$.

*Total energy balance* By setting $p_{\text{EX}}(t) \equiv 0$, i.e. by neglecting the effect of the pressure exerted by the surrounding organs, and by replacing the energy balance of the 0D left ventricle model with Eq. (20), we obtain again Eq. (13), where the total mechanical energy is now

$$\begin{aligned} \mathcal{M}(t) = {} & \mathcal{E}_{\text{LA}}(t) + \mathcal{E}_{\text{LV,3D}}(t) + \mathcal{E}_{\text{RA}}(t) + \mathcal{E}_{\text{RV}}(t) + \mathcal{E}_{\text{AR}}^{\text{SYS}}(t) + \mathcal{E}_{\text{VEN}}^{\text{SYS}}(t) + \mathcal{E}_{\text{AR}}^{\text{PUL}}(t) + \mathcal{E}_{\text{VEN}}^{\text{PUL}}(t) \\ & + \mathcal{K}_{\text{AR}}^{\text{SYS}}(t) + \mathcal{K}_{\text{VEN}}^{\text{SYS}}(t) + \mathcal{K}_{\text{AR}}^{\text{PUL}}(t) + \mathcal{K}_{\text{VEN}}^{\text{PUL}}(t) + \mathcal{K}_{\text{LV,3D}}(t) \end{aligned} \tag{21}$$

and the power of active contraction and the total dissipated power ($\Pi^{\text{diss}}(t) \geq 0$) are

$$\begin{aligned} \Pi^{\text{act}}(t) = {} & \Pi_{\text{LA}}^{\text{act}}(t) + \Pi_{\text{LV,3D}}^{\text{act}}(t) + \Pi_{\text{RA}}^{\text{act}}(t) + \Pi_{\text{RV}}^{\text{act}}(t); \\ \Pi^{\text{diss}}(t) = {} & \Pi_{\text{MV}}(t) + \Pi_{\text{AV}}(t) + \Pi_{\text{TV}}(t) + \Pi_{\text{PV}}(t) \\ & + \Pi_{\text{AR}}^{\text{SYS}}(t) + \Pi_{\text{VEN}}^{\text{SYS}}(t) + \Pi_{\text{AR}}^{\text{PUL}}(t) + \Pi_{\text{VEN}}^{\text{PUL}}(t) + \Pi_{\text{LV,3D}}^{\text{diss}}(t), \end{aligned}$$

respectively; here $\Pi^{\text{ex}}(t) \equiv 0$. We remark that Proposition 2 applies also to this case. Finally, we conclude that the 3D-0D coupled model satisfies the principle of conservation of mechanical energy. We remark that this result is achieved thanks to the energy-consistent boundary conditions imposed at the left ventricle base; see ($\mathscr{M}$). As a matter of fact, if other boundary conditions – such as homogeneous Neumann conditions – are imposed at the base instead, the relationship $\Pi_{\text{LV,3D}}^{\text{press}}(t) = p_{\text{LV}}(t) \frac{d}{dt} V_{\text{LV}}^{\text{3D}}(\mathbf{d}(t))$ may not hold and the balance of Eq. (13) would not be satisfied.

We notice that, compared to the fully 0D case, the 3D electromechanical model shows two additional terms, namely $\mathcal{K}_{\text{LV,3D}}(t)$ and $\Pi_{\text{LV,3D}}^{\text{diss}}$, respectively accounting for the kinetic energy of the left ventricle and for the dissipation associated with the interaction of $\Gamma_0^{\text{epi}}$ with surrounding tissues. Indeed, both features are not included in the 0D circulation model, in which cardiac chambers are modeled quasistatically.

### 3.3. Quantitative analysis of cardiac energetics

In Fig. 4 we report all the energy and power terms over a characteristic steady-state cardiac cycle obtained with a numerical simulation of the 0D circulation model. For this simulation we employ the parameters reported in Table 3, with $E_{\text{LV}}^{\text{act,max}} = 2.75$ mmHg mL$^{-1}$ and $E_{\text{LV}}^{\text{pass}} = 0.08$ mmHg mL$^{-1}$, with $E_{\text{LV}}^{\text{act,max}} = 2.75$ mmHg mL$^{-1}$ and $E_{\text{LV}}^{\text{pass}} = 0.08$ mmHg mL$^{-1}$. Fig. 4 (top-left) displays the time evolution of the terms of Eq. (13). We notice that, while the energy input ($\Pi^{\text{act}}$) occurs in a short time interval of nearly 100 ms (during systole), energy dissipation ($\Pi^{\text{diss}}$) takes place throughout the entire duration of the heartbeat. As a matter of fact, mechanical energy $\mathcal{M}$ plays a dominant role. Moreover, it is initially accumulated and then it is gradually dissipated as the blood flows through systemic and pulmonary circulations.

Fig. 4 (top-right, bottom-left, bottom-right) illustrate the details of the three terms $\mathcal{M}$, $\Pi^{\text{act}}$ and $\Pi^{\text{diss}}$, showing how they are split into the various subterms during the different phases of the heartbeat. Specifically, we notice that the chamber that contributes the most to the work generation is the LV, followed by the RV, while the atria only contribute – albeit to a small extent – around $t = 0.8$ s, during the atrial systole. The large part of mechanical energy and of dissipated power are associated with the systemic arterial circulation, as this branch of the circulatory network is located downstream the LV, the chamber carrying out most of the mechanical work. We remark that a non negligible dissipation of energy also takes place across the open valves, due to the high-speed blood flow across the valvular orifices.

Our model allows to estimate the daily production of mechanical work of the heart. This is obtained by multiplying the number of seconds in a day times the average generated power, given by:
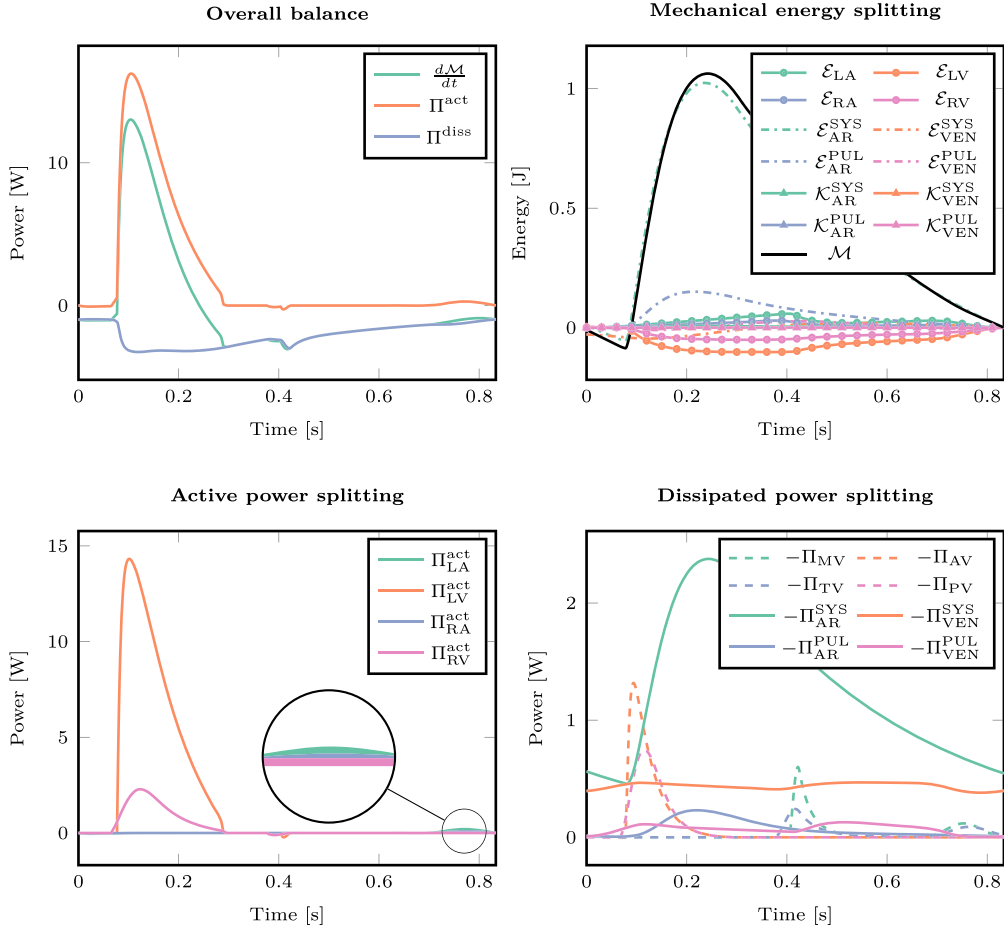
**Fig. 4.** Time evolution of both power and energy terms ($\mathcal{M}$, $\mathcal{E}$, $\mathcal{K}$, $\Pi^{\mathrm{act}}$, $\Pi^{\mathrm{diss}}$) of the 0D circulation model. A single heartbeat in a periodic regime is considered.

$$\overline{\Pi}^{\mathrm{act}} = \frac{1}{T} \int_0^T \Pi^{\mathrm{act}}(t)\, dt.$$

Applying this formula to the results of the simulation considered in Fig. 4, we obtain a daily work production of 182.5 kJ, of which 155.9 kJ attributable to the left ventricle, 24.8 kJ to the right ventricle and only 1.8 kJ to the atria.

In the daily clinical practice, the work generated by the myocardium is instead estimated through simple relationships [34,83]. In this regard, our model offers a tool to estimate the validity of these approaches. A commonly used formula [34] is

$$\overline{\Pi}^{\mathrm{act}} \simeq \overline{p_{\mathrm{AR}}^{\mathrm{SYS}}}\, \frac{SV}{T_{\mathrm{beat}}}, \tag{22}$$

where $\overline{p_{\mathrm{AR}}^{\mathrm{SYS}}}$ denotes the average systemic arterial pressure (corresponding to the wrist average blood pressure), $SV$ is the stroke volume (i.e. the difference between maximum and minimum $V_{\mathrm{LV}}$) and $T_{\mathrm{beat}}$ is the heartbeat period. By applying (22) to the results of the above simulation, we obtain a daily work generation of 152.4 kJ. Hence (22) underestimates the mechanical work by 16%. As a matter of fact, (22) only refers to the work done by the left ventricle (which is, instead, approximated up to an error of only 2%). The large part of the error is thus attributable to the work performed by the right ventricle, which is not accounted for in (22).

In common clinical practice, then, $\overline{p_{\mathrm{AR}}^{\mathrm{SYS}}}$ is not directly measured, but it is estimated as $1/3\, p_{\mathrm{max}} + 2/3\, p_{\mathrm{min}}$, where $p_{\mathrm{max}}$ and $p_{\mathrm{min}}$ are the maximum (systolic) and minimum (diastolic) arterial pressures (see e.g. [83]). With this further approximation we obtain an estimated daily work of 138.8 kJ: this underestimates the left ventricle work by 11% and the total work of the myocardium by 24%.
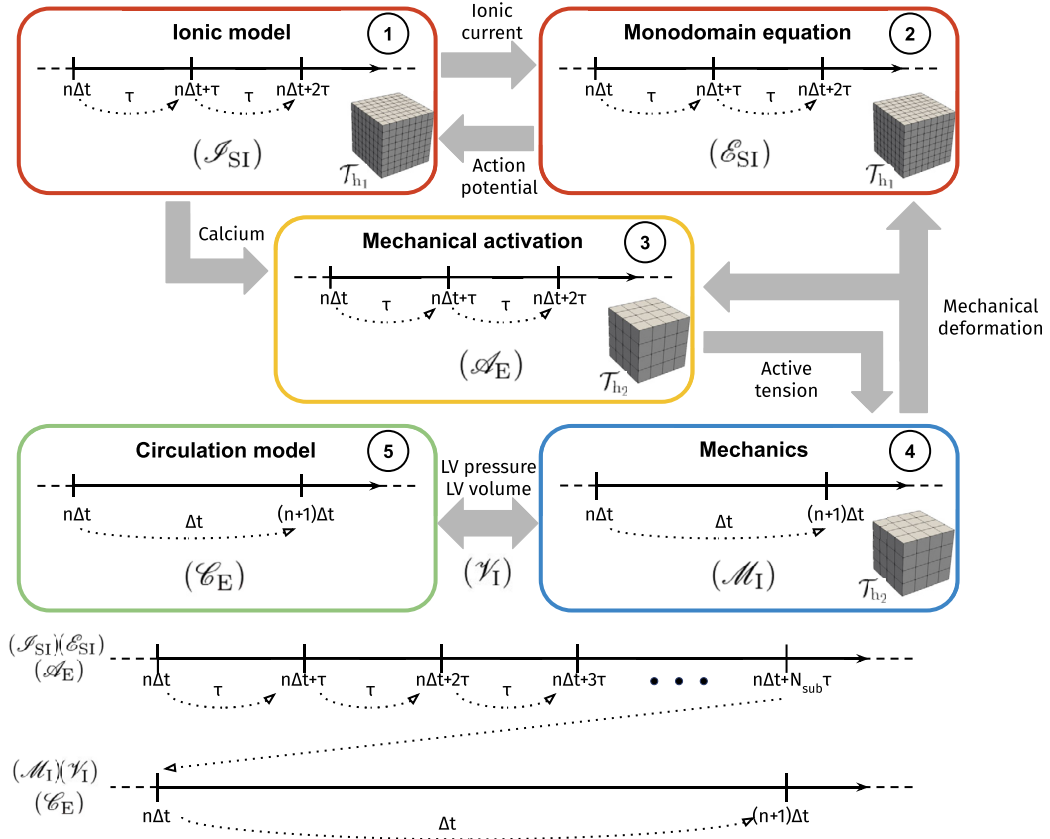
**Fig. 5.** Sketch of the segregated-intergrid-staggered numerical scheme.

## 4. Numerical approximation

We sketch in Fig. 5 the numerical approximation of problem (2). We use a partitioned numerical scheme that allows to separate and properly manage the space and time scales related to cardiac electromechanics, by using different mesh sizes and different time steps according to the characteristic scale of each core model. Our scheme is thus segregated (as the different core models are solved sequentially) and staggered (as different time step sizes can be used for the different core models) [14,37].

We perform the numerical approximation of the core models by using the Finite Element Method (FEM) in space and Finite Difference schemes in time [48].

We consider a fine representation of the computational domain for both $(\mathscr{I})$ and $(\mathscr{E})$ models, whereas a coarser one is employed for both $(\mathscr{A})$ and $(\mathscr{M})$. This is motivated by the requirement of a higher resolution for $(\mathscr{I})$ and $(\mathscr{E})$, due to the sharp wavefronts characterizing electrophysiological solutions, whereas both $(\mathscr{A})$ and $(\mathscr{M})$ feature larger spatial scales [14,10,54]. Moreover, the nonlinearities of $(\mathscr{M})$ warrants for the use of a coarser space discretization to make the numerical solution less computationally intensive.

For what concerns time discretization, we use a staggered strategy based on the Godunov splitting scheme [84]. This approach introduces a first order splitting error [37,38], which is compatible with the first order errors associated with the backward Euler method used for $(\mathscr{I})$, $(\mathscr{E})$, $(\mathscr{A})$, $(\mathscr{M})$–$(\mathscr{V})$, and the forward Euler method used for $(\mathscr{C})$. Moreover, the Godunov splitting scheme does not undermine the stability of the numerical scheme [38]. In our pipeline, we first update the variables of $(\mathscr{I})$ and $(\mathscr{E})$, then the variables of $(\mathscr{A})$ and finally, after updating the unknowns of $(\mathscr{M})$–$(\mathscr{V})$, we update the ones of $(\mathscr{C})$.

For electrophysiology, we employ a semi-implicit scheme, that we denote by $(\mathscr{I}_{\mathrm{SI}})$–$(\mathscr{E}_{\mathrm{SI}})$, where SI stands for semi-implicit. Mechanical activation $(\mathscr{A}_{\mathrm{E}})$, is solved with an explicit method in time. Mechanics $(\mathscr{M}_{\mathrm{I}})$ is instead implicitly discretized in time, due to the fact that the highly nonlinear (exponential) terms of the strain energy function $\mathcal{W}$ would need a restriction on the time step in both the semi-implicit and explicit contexts. Finally, we employ an explicit scheme for the circulation model, indicated as $(\mathscr{C}_{\mathrm{E}})$. We use two different time steps for $(\mathscr{I}_{\mathrm{SI}})$–$(\mathscr{E}_{\mathrm{SI}})$–$(\mathscr{A}_{\mathrm{E}})$ and for $(\mathscr{M}_{\mathrm{I}})$–$(\mathscr{V}_{\mathrm{I}})$–$(\mathscr{C}_{\mathrm{E}})$.

We propose a novel strategy to perform the 3D-0D coupling, given by $(\mathscr{V})$, between $(\mathscr{M})$ and $(\mathscr{C})$, at the numerical level, within a segregated setting. Specifically, we solve the 3D mechanical problem under a volumetric constraint coming

from the 0D circulation model. The cavity pressure acts as Lagrange multiplier associated with this constraint. Thus, we obtain a saddle-point problem that we address, at the algebraic level, by means of a Schur complement reduction.

### 4.1. Space discretization and intergrid interpolation

We implemented an intergrid transfer operator between nested grids that can be generalized to the case of locally-refined non-conforming nested grids. More details about this strategy can be found in [46]. We built an efficient and scalable interpolation data structure on top of the intergrid transfer operator that enables to evaluate the feedback coming from ($\mathscr{E}$) at the quadrature nodes defined on the mesh used for ($\mathscr{M}$) (and vice-versa), regardless of the polynomial degree used to discretize the two different models. This enables for a high level of numerical flexibility: different Finite Element degrees, as well as different levels of mesh refinement, can be effortlessly selected to tune the computational efficiency on the desired accuracy.

We consider two nested hexahedral meshes $\mathcal{T}_{h_1}$ and $\mathcal{T}_{h_2}$ of the computational domain $\Omega_0$, where $\mathcal{T}_{h_1}$ has been generated by uniformly refining $\mathcal{T}_{h_2}$ according to an octree structure [46,85], i.e. by recursively splitting each parent element of $\mathcal{T}_{h_2}$ into eight sub-elements for a prescribed number of times, i.e. until the desired geometrical detail is reached. Here $h_1$ and $h_2$ (with $h_1 < h_2$) represent the mesh sizes, which we compute as the mean of the maximum diameter of each element.

We denote by $N_u$, $N_{w,z}$, $N_s$ and $N_d$ the number of degrees of freedom (DOFs, that is the number of variables) for the dimensionless transmembrane potential, gating and concentration variables, mechanical activation variables and displacement, respectively. We denote the set of tensor-products of polynomials with degree smaller than or equal to $r$ over a mesh element $K$ by $\mathbb{Q}_r(K)$, and we introduce the following finite dimensional spaces:

$$\mathcal{X}_{h_1}^r = \{v \in C^0(\overline{\Omega}_0) : v|_K \in \mathbb{Q}_r(K) \ \forall K \in \mathcal{T}_{h_1}\},$$
$$\mathcal{X}_{h_2}^s = \{v \in C^0(\overline{\Omega}_0) : v|_K \in \mathbb{Q}_s(K) \ \forall K \in \mathcal{T}_{h_2}\},$$

for $r, s \geq 1$.

We adopt the following notation. We denote by, e.g., $\mathbf{d}_{h_1}(t) \approx \mathbf{d}(t)$ the semi-discretized Finite Element approximation of the variable $\mathbf{d}(t)$, defined over the computational mesh $\mathcal{T}_{h_1}$. On the other hand, we denote by $\underline{\mathbf{d}}_{h_1}(t)$ the vector collecting the DOFs associated with $\mathbf{d}_{h_1}(t)$. Finally, we denote by $\underline{\mathbf{d}}_{h_1}^n \simeq \underline{\mathbf{d}}_{h_1}(t^n)$ the vector collecting the DOFs of the fully discretized Finite Element problem.

*Monodomain equation*  The set of basis functions for $\mathcal{X}_{h_1}^r$ with $N_u = \dim(\mathcal{X}_{h_1}^r)$ is given by $\{\phi_i\}_{i=1}^{N_u}$. The semi-discretized formulation of the monodomain equation reads: find $u_{h_1}(t) \in \mathcal{X}_{h_1}^r$ for all $t \in (0, T)$ such that

$$\int_{\Omega_0} \dot{u}_{h_1}(t)\phi_i \, d\Omega_0 + \int_{\Omega_0} (J_{h_1}\mathbf{F}_{h_1}^{-1}(\mathbf{d}_{h_1}(t))\widetilde{\boldsymbol{D}}_{M,h_1}(\mathbf{d}_{h_1}(t))\mathbf{F}_{h_1}^{-T}(\mathbf{d}_{h_1}(t))\nabla u_{h_1}(t)) \cdot \nabla\phi_i \, d\Omega_0$$

$$+ \int_{\Omega_0} \widetilde{\mathcal{I}}_{ion}(u_{h_1}(t), \boldsymbol{w}_{h_1}(t), \boldsymbol{z}_{h_1}(t))\phi_i \, d\Omega_0 = \int_{\Omega_0} \widetilde{\mathcal{I}}_{app}(t)\phi_i \, d\Omega_0 \quad \forall i = 1, ..., N_u, \tag{23}$$

with $u_{h_1}(0) = \sum_{j=1}^{N_u}(u_0, \phi_j)_{L^2(\Omega_0)}\phi_j$. The functions $\boldsymbol{w}_{h_1}(t)$ and $\boldsymbol{z}_{h_1}(t)$ are the semi-discretized versions of the gating variables and of the concentration variables, whereas $u_{h_1}(t) = \sum_{j=1}^{N_u} u_{j,h_1}(t)\phi_j$ is the Finite Element solution that approximates $u = u(t)$. The tensor $\mathbf{F}_{h_1}$ is the interpolated deformation tensor, obtained through the following procedure:

- The approximate solution $\mathbf{d}_{h_2}$ to problem ($\mathscr{M}$) is interpolated from $\mathcal{T}_{h_2}$ to $\mathcal{T}_{h_1}$ to compute $\mathbf{d}_{h_1}$. The evaluation of $\mathbf{d}_{h_1}$ at the quadrature points used to approximate Eq. (23) is performed using our intergrid transfer operator between nested meshes and arbitrary Finite Element spaces.
- We build $\mathbf{F}_{h_1} = \mathbf{I} + \nabla\mathbf{d}_{h_1}$ directly on $\mathcal{T}_{h_1}$ after the interpolation procedure applied on the displacement field.

We rewrite Eq. (23) as a system of nonlinear ODEs by setting $\underline{\boldsymbol{u}}_{h_1}(t) = \{u_{j,h_1}(t)\}_{j=1}^{N_u}$:

$$\begin{cases} \mathcal{M}\dot{\underline{\boldsymbol{u}}}_{h_1}(t) + \mathcal{K}(\underline{\mathbf{d}}_{h_1}(t))\underline{\boldsymbol{u}}_{h_1}(t) + \boldsymbol{I}_{ion}(\underline{\boldsymbol{u}}_{h_1}(t), \underline{\boldsymbol{w}}_{h_1}(t), \underline{\boldsymbol{z}}_{h_1}(t)) = \boldsymbol{I}_{app}(t) \quad \forall t \in (0, T), \\ \underline{\boldsymbol{u}}_{h_1}(0) = \underline{\boldsymbol{u}}_{0,h_1}, \end{cases} \tag{24}$$

where we have defined the following matrices

$$\mathcal{M}_{ij} = \int_{\Omega_0} J_{h_1}\phi_j\phi_i \, d\Omega_0, \quad \mathcal{K}_{ij}(\underline{\mathbf{d}}_{h_1}(t)) = \int_{\Omega_0} (J_{h_1}\mathbf{F}_{h_1}^{-1}\widetilde{\boldsymbol{D}}_{M,h_1}\mathbf{F}_{h_1}^{-T}\nabla\phi_j) \cdot \nabla\phi_i \, d\Omega_0,$$

and the following vectors

$$\left(\boldsymbol{I}_{\text{ion}}(\underline{\boldsymbol{u}}_{\text{h}_1}(t), \underline{\boldsymbol{w}}_{\text{h}_1}(t), \underline{\boldsymbol{z}}_{\text{h}_1}(t))\right)_{\text{i}} = \int\limits_{\Omega_0} J_{\text{h}_1} \widetilde{\mathcal{I}}_{\text{ion}}(u_{\text{h}_1}(t), \boldsymbol{w}_{\text{h}_1}(t), \boldsymbol{z}_{\text{h}_1}(t))\phi_{\text{i}} \, d\Omega_0,$$

$$\left(\boldsymbol{I}_{\text{app}}(t)\right)_{\text{i}} = \int\limits_{\Omega_0} J_{\text{h}_1} \widetilde{\mathcal{I}}_{\text{app}}(t)\phi_{\text{i}} \, d\Omega_0.$$

For the evaluation of the nonlinear term $\boldsymbol{I}_{\text{ion}}(\underline{\boldsymbol{u}}_{\text{h}_1}(t), \underline{\boldsymbol{w}}_{\text{h}_1}(t), \underline{\boldsymbol{z}}_{\text{h}_1}(t))$, three strategies are available [15,86–89]. In this work, we use the so-called ionic current interpolation (ICI) approach, which yields a faster assembly of the ionic term [15,86]. By denoting by $\{\boldsymbol{x}_q^K\}_{q=1}^{N_q}$ and $\{\omega_q^K\}_{q=1}^{N_q}$ the quadrature nodes and weights of a generic mesh element of $K \in \mathcal{T}_{\text{h}_1}$, the term $\boldsymbol{I}_{\text{ion}}(\underline{\boldsymbol{u}}_{\text{h}_1}(t), \underline{\boldsymbol{w}}_{\text{h}_1}(t), \underline{\boldsymbol{z}}_{\text{h}_1}(t))$ is firstly evaluated at the DOFs and then interpolated at the quadrature nodes, i.e.:

$$\int\limits_{\Omega_0} J_{\text{h}_1} \widetilde{\mathcal{I}}_{\text{ion}}(u_{\text{h}_1}(t), \boldsymbol{w}_{\text{h}_1}(t), \boldsymbol{z}_{\text{h}_1}(t))\phi_{\text{i}} \, d\Omega_0$$

$$\approx \sum_{K \in \mathcal{T}_{\text{h}_1}} \left( \sum_{q=1}^{N_q} J_{\text{q,h}_1} \sum_{j=1}^{N_u} \widetilde{\mathcal{I}}_{\text{ion}}\left(u_{\text{j,h}_1}(t), \boldsymbol{w}_{\text{j,h}_1}(t)\boldsymbol{z}_{\text{j,h}_1}(t)\right) \phi_{\text{j}}(\boldsymbol{x}_q^K)\phi_{\text{i}}(\boldsymbol{x}_q^K)\omega_q^K \right). \tag{25}$$

*Ionic model*   The ionic model under consideration is a system of 18 ODEs (12 for the gating variables, 6 for the concentration variables), which indirectly depends on the space variable over the mesh $\mathcal{T}_{\text{h}_1}$ through the transmembrane potential $u$. The semi-discrete formulation can be written as follows:

$$\begin{cases} \underline{\dot{\boldsymbol{w}}}_{\text{h}_1}(t) = \overline{\boldsymbol{H}}(\underline{\boldsymbol{u}}_{\text{h}_1}(t), \underline{\boldsymbol{w}}_{\text{h}_1}(t)) & \forall t \in (0, T), \\ \underline{\dot{\boldsymbol{z}}}_{\text{h}_1}(t) = \overline{\boldsymbol{G}}(\underline{\boldsymbol{u}}_{\text{h}_1}(t), \underline{\boldsymbol{w}}_{\text{h}_1}(t), \underline{\boldsymbol{z}}_{\text{h}_1}(t)) & \forall t \in (0, T), \\ \underline{\boldsymbol{w}}_{\text{h}_1}(0) = \underline{\boldsymbol{w}}_{0, \text{h}_1}, \\ \underline{\boldsymbol{z}}_{\text{h}_1}(0) = \underline{\boldsymbol{z}}_{0, \text{h}_1}. \end{cases} \tag{26}$$

*Mechanical activation model*   The semi-discrete formulation, which is written on $\mathcal{T}_{\text{h}_2}$, reads:

$$\begin{cases} \underline{\dot{\boldsymbol{s}}}_{\text{h}_2}(t) = \overline{\boldsymbol{K}}(\underline{\boldsymbol{s}}_{\text{h}_2}(t), ([\text{Ca}^{2+}]_{\text{i,h}_2}(t), SL_{\text{h}_2}(t))^T) & \forall t \in (0, T), \\ \underline{\boldsymbol{s}}_{\text{h}_2}(0) = \underline{\boldsymbol{s}}_{0, \text{h}_2}, \end{cases} \tag{27}$$

where $[\text{Ca}^{2+}]_{\text{i,h}_2}(t)$ is obtained by interpolating the intracellular calcium concentration of TTP06 model from $\mathcal{T}_{\text{h}_1}$ to $\mathcal{T}_{\text{h}_2}$ as explained in the introduction to this section. The operator $\overline{\boldsymbol{K}}$ represents the element-wise application of the ANN associated with the activation model, previously trained from a collection of simulations obtained with the high-fidelity RDQ18 model [32,33]. On the other hand, $SL_{\text{h}_2}(t) \in \mathcal{X}_{\text{h}_2}^s$ is obtained by solving, for any $t \in (0, T)$:

$$\int\limits_{\Omega_0} SL_{\text{h}_2}(t)\phi + \sum_{K \in \mathcal{T}_{\text{h}_2}} \int\limits_K h^2 \nabla SL_{\text{h}_2}(t) \cdot \nabla\phi = \int\limits_{\Omega_0} SL_0 \sqrt{\mathcal{I}_{4f, \text{h}_2}(t)} \phi \qquad \forall\phi \in \mathcal{X}_{\text{h}_2}^s, \tag{28}$$

where $\mathcal{I}_{4f, \text{h}_2}(t) = \mathbf{F}_{\text{h}_2}(t)\mathbf{f}_0 \cdot \mathbf{F}_{\text{h}_2}(t)\mathbf{f}_0$. Equation (28) corresponds to an $L^2$ projection of the field $SL_0\sqrt{\mathcal{I}_{4f, \text{h}_2}(t)}$ onto the Finite Element space $\mathcal{X}_{\text{h}_2}^s$ with an harmonic smoothing. We notice that the smoothing term scales as $h^2$ (the mesh size). This term allows to regularize the $SL$ field in the case of coarse meshes, by smoothing the discontinuities that the displacement gradient might show across the mesh elements. In the case of fine meshes, instead, the term becomes irrelevant as it vanishes for $h \to 0$. This is in fact numerically consistent with the continuous problem [48]. Finally, $T_{\text{a,h}_2}(t)$ denotes the semi-discretized active tension, obtained by evaluating the function $T_{\text{a}} = T_{\text{a}}^{\max}G(\boldsymbol{s})$ at the nodes.

*Mechanical model*   We denote by $[\mathcal{X}_{\text{h}_2}^s]^3$ the finite dimensional subspace of vector valued functions and by $\{\boldsymbol{\phi}_{\text{i}}\}_{\text{i}=1}^{N_\mathbf{d}}$ its basis. The semi-discretized version of $(\mathcal{M})$ reads: given $T_{\text{a,h}_2}(t)$, find $\mathbf{d}_{\text{h}_2} = \mathbf{d}_{\text{h}_2}(t) \in [\mathcal{X}_{\text{h}_2}^s]^3$ for all $t \in (0, T)$ such that

$$
\int_{\Omega_0} \rho_{\mathrm{s}} \ddot{\mathbf{d}}_{\mathrm{h}_2}(t) \cdot \boldsymbol{\phi}_{\mathrm{i}} \, d\Omega_0 + \int_{\Omega_0} \mathbf{P}(\mathbf{d}_{\mathrm{h}_2}(t), T_{\mathrm{a},\mathrm{h}_2}(t)) : \nabla \boldsymbol{\phi}_{\mathrm{i}} \, d\Omega_0
$$

$$
+ \int_{\Gamma_0^{\mathrm{epi}}} \left[ (\mathbf{N}_{\mathrm{h}_2} \otimes \mathbf{N}_{\mathrm{h}_2}) \left( K_\perp^{\mathrm{epi}} \mathbf{d}_{\mathrm{h}_2}(t) + C_\perp^{\mathrm{epi}} \dot{\mathbf{d}}_{\mathrm{h}_2}(t) \right) \right.
$$

$$
\left. + (\mathbf{I} - \mathbf{N}_{\mathrm{h}_2} \otimes \mathbf{N}_{\mathrm{h}_2}) \left( K_\parallel^{\mathrm{epi}} \mathbf{d}_{\mathrm{h}_2}(t) + C_\parallel^{\mathrm{epi}} \dot{\mathbf{d}}_{\mathrm{h}_2}(t) \right) \right] \cdot \boldsymbol{\phi}_{\mathrm{i}} \, d\Gamma_0 \tag{29}
$$

$$
= -p_{\mathrm{LV}}(t) \int_{\Gamma_0^{\mathrm{endo}}} J_{\mathrm{h}_2} \mathbf{F}_{\mathrm{h}_2}^{-T} \mathbf{N} \cdot \boldsymbol{\phi}_{\mathrm{i}} \, d\Gamma_0 + p_{\mathrm{LV}}(t) \int_{\Gamma_0^{\mathrm{base}}} |J_{\mathrm{h}_2} \mathbf{F}_{\mathrm{h}_2}^{-T} \mathbf{N}| \mathbf{v}_{\mathrm{h}_2}^{\mathrm{base}} \cdot \boldsymbol{\phi}_{\mathrm{i}} \, d\Gamma_0
$$

$$
\forall i = 1, \ldots, N_{\mathbf{d}},
$$

with $\mathbf{d}_{\mathrm{h}_2}(0) = \sum_{j=1}^{N_{\mathbf{d}}} (\mathbf{d}_0, \boldsymbol{\phi}_{\mathrm{j}})_{[L^2(\Omega_0)]^3} \boldsymbol{\phi}_{\mathrm{j}}$, $\dot{\mathbf{d}}_{\mathrm{h}_2}(0) = \sum_{j=1}^{N_{\mathbf{d}}} (\dot{\mathbf{d}}_0, \boldsymbol{\phi}_{\mathrm{j}})_{[L^2(\Omega_0)]^3} \boldsymbol{\phi}_{\mathrm{j}}$ and where

$$
\mathbf{v}_{\mathrm{h}_2}^{\mathrm{base}} = \frac{\int_{\Gamma_0^{\mathrm{endo}}} J_{\mathrm{h}_2} \mathbf{F}_{\mathrm{h}_2}^{-T} \mathbf{N} \, d\Gamma_0}{\int_{\Gamma_0^{\mathrm{base}}} |J_{\mathrm{h}_2} \mathbf{F}_{\mathrm{h}_2}^{-T} \mathbf{N}| \, d\Gamma_0}.
$$

The corresponding algebraic formulation reads:

$$
\begin{cases}
\rho_{\mathrm{s}} \mathcal{M} \ddot{\underline{\mathbf{d}}}_{\mathrm{h}_2}(t) + \mathcal{F} \dot{\underline{\mathbf{d}}}_{\mathrm{h}_2}(t) + \mathcal{G} \underline{\mathbf{d}}_{\mathrm{h}_2}(t) + \boldsymbol{S}(\underline{\mathbf{d}}_{\mathrm{h}_2}(t), T_{\mathrm{a},\mathrm{h}_2}(t)) = p_{\mathrm{LV}}(t) \, \boldsymbol{p}(\underline{\mathbf{d}}_{\mathrm{h}_2}(t)) & \forall t \in (0, T), \\
\underline{\mathbf{d}}_{\mathrm{h}_2}(0) = \underline{\mathbf{d}}_{0,\mathrm{h}_2}, \quad \dot{\underline{\mathbf{d}}}_{\mathrm{h}_2}(0) = \dot{\underline{\mathbf{d}}}_{0,\mathrm{h}_2},
\end{cases} \tag{30}
$$

with:

$$
\boldsymbol{S}_i(\underline{\mathbf{d}}_{\mathrm{h}_2}(t), T_{\mathrm{a},\mathrm{h}_2}(t)) = \int_{\Omega_0} \mathbf{P}(\mathbf{d}_{\mathrm{h}_2}(t), T_{\mathrm{a},\mathrm{h}_2}(t)) : \nabla \boldsymbol{\phi}_{\mathrm{i}} \, d\Omega_0,
$$

$$
\mathcal{F}_{\mathrm{i,j}} = \int_{\Gamma_0^{\mathrm{epi}}} \left[ (\mathbf{N}_{\mathrm{h}_2} \otimes \mathbf{N}_{\mathrm{h}_2}) C_\perp^{\mathrm{epi}} + (\mathbf{I} - \mathbf{N}_{\mathrm{h}_2} \otimes \mathbf{N}_{\mathrm{h}_2}) C_\parallel^{\mathrm{epi}} \right] \boldsymbol{\phi}_{\mathrm{j}} \cdot \boldsymbol{\phi}_{\mathrm{i}} \, d\Gamma_0,
$$

$$
\mathcal{G}_{\mathrm{i,j}} = \int_{\Gamma_0^{\mathrm{epi}}} \left[ (\mathbf{N}_{\mathrm{h}_2} \otimes \mathbf{N}_{\mathrm{h}_2}) K_\perp^{\mathrm{epi}} + (\mathbf{I} - \mathbf{N}_{\mathrm{h}_2} \otimes \mathbf{N}_{\mathrm{h}_2}) K_\parallel^{\mathrm{epi}} \right] \boldsymbol{\phi}_{\mathrm{j}} \cdot \boldsymbol{\phi}_{\mathrm{i}} \, d\Gamma_0,
$$

$$
\boldsymbol{p}_{\mathrm{i}}(\underline{\mathbf{d}}_{\mathrm{h}_2}(t)) = \int_{\Gamma_0^{\mathrm{base}}} |J_{\mathrm{h}_2} \mathbf{F}_{\mathrm{h}_2}^{-T} \mathbf{N}| \mathbf{v}_{\mathrm{h}_2}^{\mathrm{base}} \cdot \boldsymbol{\phi}_{\mathrm{i}} \, d\Gamma_0 - \int_{\Gamma_0^{\mathrm{endo}}} J_{\mathrm{h}_2} \mathbf{F}_{\mathrm{h}_2}^{-T} \mathbf{N} \cdot \boldsymbol{\phi}_{\mathrm{i}} \, d\Gamma_0,
$$

where $\underline{\mathbf{d}}_{\mathrm{h}_2}(t) = \{\mathbf{d}_{\mathrm{j},\mathrm{h}_2}(t)\}_{j=1}^{N_{\mathbf{d}}}$. Equations (23), (26), (27) and (29) provide a splitted semi-discretization of the entire electromechanical model.

## 4.2. Time discretization

We define $\Delta t$ as the time step for $(\mathcal{M}_{\mathrm{I}})$–$(\mathcal{V}_{\mathrm{I}})$, $(\mathcal{C}_{\mathrm{E}})$ and $\tau = \Delta t / N_{\mathrm{sub}}$ as the time step for $(\mathcal{I}_{\mathrm{SI}})$, $(\mathcal{E}_{\mathrm{SI}})$, $(\mathcal{A}_{\mathrm{E}})$, being $N_{\mathrm{sub}} \in \mathbb{N}$ the number of intermediate substeps that need to be solved by $(\mathcal{I}_{\mathrm{SI}})$–$(\mathcal{E}_{\mathrm{SI}})$–$(\mathcal{A}_{\mathrm{E}})$ before a time step $\Delta t$ of $(\mathcal{M}_{\mathrm{I}})$–$(\mathcal{V}_{\mathrm{I}})$ and $(\mathcal{C}_{\mathrm{E}})$ is performed.

Problem $(\mathcal{I}_{\mathrm{SI}})$–$(\mathcal{E}_{\mathrm{SI}})$–$(\mathcal{A}_{\mathrm{E}})$ from $t^n$ to $t^{n+1}$, once we set $t^{n+\frac{m}{N_{\mathrm{sub}}}} = t^n + m\tau$, for $m = 1, \ldots, N_{\mathrm{sub}}$, reads as follows:

- We find $\underline{\boldsymbol{w}}_{\mathrm{h}_1}^{n+\frac{m}{N_{\mathrm{sub}}}}$ and $\underline{\boldsymbol{z}}_{\mathrm{h}_1}^{n+\frac{m}{N_{\mathrm{sub}}}}$ defined on $\mathcal{T}_{\mathrm{h}_1}$ by solving:

$$
\begin{cases}
\dfrac{1}{\tau} \underline{\boldsymbol{w}}_{\mathrm{h}_1}^{n+\frac{m}{N_{\mathrm{sub}}}} = \dfrac{1}{\tau} \underline{\boldsymbol{w}}_{\mathrm{h}_1}^n + \overline{\boldsymbol{H}}(\underline{\boldsymbol{u}}_{\mathrm{h}_1}^n, \underline{\boldsymbol{w}}_{\mathrm{h}_1}^{n+\frac{m}{N_{\mathrm{sub}}}}), \\
\dfrac{1}{\tau} \underline{\boldsymbol{z}}_{\mathrm{h}_1}^{n+\frac{m}{N_{\mathrm{sub}}}} = \dfrac{1}{\tau} \underline{\boldsymbol{z}}_{\mathrm{h}_1}^n + \overline{\boldsymbol{G}}(\underline{\boldsymbol{u}}_{\mathrm{h}_1}^n, \underline{\boldsymbol{w}}_{\mathrm{h}_1}^n, \underline{\boldsymbol{z}}_{\mathrm{h}_1}^n).
\end{cases} \tag{31}
$$

We adopt here the first order IMEX scheme proposed in [35]. Specifically, we employ an explicit treatment of the ionic concentrations to avoid the solution of a nonlinear system (such choice does not compromise the stability of the scheme, thanks to the non-stiff dynamics of concentrations), and an implicit treatment of the gating variables, because of the severe CFL condition on the time step induced by an explicit scheme. We notice that, thanks to the linear dynamics of the gating variables, such implicit handling does not require the solution of a system of linear or nonlinear equations.

- We interpolate $\underline{\mathbf{d}}_{h_2}^n$ on the fine mesh $\mathcal{T}_{h_1}$ at $t = t^n$. We use $\underline{\mathbf{z}}_{h_1}^{n+\frac{m}{N_{sub}}}$ from (31) and $\underline{\mathbf{d}}_{h_1}^n$ to find $\underline{\mathbf{u}}_{h_1}^{n+\frac{m}{N_{sub}}}$ over $\mathcal{T}_{h_1}$ by solving:

$$
\left( \frac{1}{\tau} \mathcal{M} + \mathcal{K}(\underline{\mathbf{d}}_{h_1}^n) + \boldsymbol{I}_u^{ion} \left( \underline{\mathbf{u}}_{h_1}^n, \underline{\mathbf{z}}_{h_1}^{n+\frac{m}{N_{sub}}} \right) \right) \underline{\mathbf{u}}_{h_1}^{n+\frac{m}{N_{sub}}} =
$$
$$
\frac{1}{\tau} \mathcal{M} \underline{\mathbf{u}}_{h_1}^n - \tilde{\boldsymbol{I}}^{ion} \left( \underline{\mathbf{u}}_{h_1}^n, \underline{\mathbf{z}}_{h_1}^{n+\frac{m}{N_{sub}}} \right) + \boldsymbol{I}_{app} \left( t^{n+\frac{m}{N_{sub}}} \right).
\tag{32}
$$

  $\boldsymbol{I}_u^{ion}$ is the derivative of the terms of $\boldsymbol{I}_{ion}$ that linearly depends on $\underline{\mathbf{u}}_{h_1}$, while $\tilde{\boldsymbol{I}}^{ion}$ collects all the other terms.

- We interpolate $[Ca^{2+}]_{i,h_2}^{n+\frac{m}{N_{sub}}}$ from (31) on the coarse mesh $\mathcal{T}_{h_2}$, and we find $\underline{\mathbf{s}}_{h_2}^{n+\frac{m}{N_{sub}}}$ by solving:

$$
\underline{\mathbf{s}}_{h_2}^{n+\frac{m}{N_{sub}}} = \underline{\mathbf{s}}_{h_2}^n + \tau \overline{\boldsymbol{K}}(\underline{\mathbf{s}}_{h_2}^n, ([Ca^{2+}]_{i,h_2}^{n+\frac{m}{N_{sub}}}, SL_{h_2}^n)^T),
\tag{33}
$$

  where $SL_{h_2}^n$ is obtained by solving problem (28).

After having solved (31), (32) and (33) for $N_{sub}$ steps, we treat $(\mathcal{M}_I)$–$(\mathcal{V}_I)$ and $(\mathcal{C}_E)$ at $t^{n+1}$ in the following way:

- We update $\underline{\mathbf{d}}_{h_2}^{n+1}$ and $p_{LV}^{n+1}$ with the following system:

$$
\begin{cases}
\left( \rho_s \frac{1}{\Delta t^2} \mathcal{M} + \frac{1}{\Delta t} \mathcal{F} + \mathcal{G} \right) \underline{\mathbf{d}}_{h_2}^{n+1} + \boldsymbol{S}(\underline{\mathbf{d}}_{h_2}^{n+1}, \mathbf{T}_{a,h_2}^{n+1}) \\
\qquad = \rho_s \frac{2}{\Delta t^2} \mathcal{M} \underline{\mathbf{d}}_{h_2}^n - \rho_s \frac{1}{\Delta t^2} \mathcal{M} \underline{\mathbf{d}}_{h_2}^{n-1} + \frac{1}{\Delta t} \mathcal{F} \underline{\mathbf{d}}_{h_2}^n + p_{LV}^{n+1} \boldsymbol{p}(\underline{\mathbf{d}}_{h_2}^{n+1}), \\
V_{LV}^{3D}(\underline{\mathbf{d}}_{h_2}^{n+1}) = V_{LV}^{0D}(\boldsymbol{c}_1^n).
\end{cases}
\tag{34}
$$

- We find $\boldsymbol{c}_1^{n+1}$ with the forward Euler method:

$$
\boldsymbol{c}_1^{n+1} = \boldsymbol{c}_1^n + \Delta t \, \tilde{\boldsymbol{D}} \left( t^n, \boldsymbol{c}_1^n, p_{LV}^{n+1} \right).
\tag{35}
$$

Eq. (34) is a nonlinear saddle-point problem. In the next section (Sec. 4.3) we provide details about its numerical approximation at the algebraic level. An alternative to our approach for numerical discretization would be employing implicit monolithic schemes, which are known to be stable and accurate, but at the same time they present constraints in the choice of the time steps and they are characterized by high computational costs [14,15]. Indeed, we can only use one time step and one mesh with a monolithic approach. Therefore, we are forced to choose a small time step and a fine representation of the computational domain due to the requirements of cardiac electrophysiology. Our approach is instead accurate and computationally efficient, thanks to the flexibility in the choice of both space and time resolution among the different core models.

### 4.3. Algorithm for the resolution of Eq. (34)

We approximate the solution of Eq. (34) by means of a quasi-Newton strategy [48], as we proposed in [33]. Specifically, in the computation of the Jacobian matrix, we neglect the derivative of the nonlocal term $\mathbf{v}_{h_2}^{base}$ in the pressure variable, and we update the Jacobian at each time step, but not through the iterations of Newton's loop. By moving all the terms in Eq. (34) to the left hand side and by rewriting its first and second line as $\mathbf{r}_{\mathbf{d}}^{n+1}(\underline{\mathbf{d}}_{h_2}^{n+1}, p_{LV}^{n+1}) = \mathbf{0}$ and $r_p^{n+1}(\underline{\mathbf{d}}_{h_2}^{n+1}) = 0$, respectively, the quasi-Newton algorithm reads as follows:

- We set $\underline{\mathbf{d}}_{h_2}^{n+1,0} = \underline{\mathbf{d}}_{h_2}^n$ and $p_{LV}^{n+1,0} = p_{LV}^n$.
- For $j = 0, 1, \ldots$, until a convergence criterion is not fulfilled, we solve the following linear system:

$$
\begin{pmatrix} J_{\mathbf{d},\mathbf{d}}^{n+1} & J_{\mathbf{d},p}^{n+1} \\ J_{p,\mathbf{d}}^{n+1} & 0 \end{pmatrix} \begin{pmatrix} \Delta \underline{\mathbf{d}}_{h_2}^{n+1,j} \\ \Delta p_{LV}^{n+1,j} \end{pmatrix} = - \begin{pmatrix} \mathbf{r}_{\mathbf{d}}^{n+1,j} \\ r_p^{n+1,j} \end{pmatrix},
\tag{36}
$$

  where $J_{\mathbf{d},\mathbf{d}}^{n+1} \simeq \frac{\partial}{\partial \underline{\mathbf{d}}} \mathbf{r}_{\mathbf{d}}^{n+1}(\underline{\mathbf{d}}_{h_2}^n, p_{LV}^n)$ (wherein we neglected the derivative with respect to the nonlocal term $\mathbf{v}_{h_2}^{base}$), $J_{\mathbf{d},p}^{n+1} = \frac{\partial}{\partial p} \mathbf{r}_{\mathbf{d}}^{n+1}(\underline{\mathbf{d}}_{h_2}^n, p_{LV}^n)$, $J_{p,\mathbf{d}}^{n+1} = \frac{\partial}{\partial \underline{\mathbf{d}}} r_p^{n+1}(\underline{\mathbf{d}}_{h_2}^n)$, $\mathbf{r}_{\mathbf{d}}^{n+1,j} = \mathbf{r}_{\mathbf{d}}^{n+1}(\underline{\mathbf{d}}_{h_2}^{n+1,j}, p_{LV}^{n+1,j})$ and $r_p^{n+1,j} = r_p^{n+1}(\underline{\mathbf{d}}_{h_2}^{n+1,j})$.
- We update $\underline{\mathbf{d}}_{h_2}^{n+1,j+1} = \underline{\mathbf{d}}_{h_2}^{n+1,j} + \Delta \underline{\mathbf{d}}_{h_2}^{n+1,j}$ and $p_{LV}^{n+1,j+1} = p_{LV}^{n+1,j} + \Delta p_{LV}^{n+1,j}$.
- When the convergence criterion is satisfied, we set $\underline{\mathbf{d}}_{h_2}^{n+1} = \underline{\mathbf{d}}_{h_2}^{n+1,j}$ and $p_{LV}^{n+1} = p_{LV}^{n+1,j}$.

From the algebraic viewpoint, we solve the saddle-point problem (36) via Schur complement reduction [51]. Specifically, we solve the two linear systems

$$J_{\mathbf{d},\mathbf{d}}^{n+1}\mathbf{v}^{n+1,j} = \mathbf{r}_{\mathbf{d}}^{n+1,j}, \qquad J_{\mathbf{d},\mathbf{d}}^{n+1}\mathbf{w}^{n+1,j} = J_{\mathbf{d},\mathrm{p}}^{n+1}$$

and we set:

$$\Delta p_{\mathrm{LV}}^{n+1,j} = \frac{r_p^{n+1,j} - J_{\mathrm{p},\mathbf{d}}^{n+1}\mathbf{v}^{n+1,j}}{J_{\mathrm{p},\mathbf{d}}^{n+1}\mathbf{w}^{n+1,j}}, \quad \Delta \underline{\mathbf{d}}_{\mathrm{h2}}^{n+1,j} = -\left(\mathbf{v}^{n+1,j} + \mathbf{w}^{n+1,j}\Delta p_{\mathrm{LV}}^{n+1,j}\right). \tag{37}$$

We remark that, thanks to the reuse of the Jacobian matrix throughout the Newton loop, $\mathbf{w}^{n+1,j}$ becomes independent of $j$ and thus it does not need to be recomputed at each iteration. Our scheme only involves the following operations: for each time step, we assemble the matrix $J_{\mathbf{d},\mathbf{d}}^{n+1}$ and the vectors $J_{\mathrm{p},\mathbf{d}}^{n+1}$ and $J_{\mathbf{d},\mathrm{p}}^{n+1}$ and we solve the linear system $J_{\mathbf{d},\mathbf{d}}^{n+1}\mathbf{w}^{n+1,0} = J_{\mathbf{d},\mathrm{p}}^{n+1}$; at each Newton iteration, we only need to solve the linear system $J_{\mathbf{d},\mathbf{d}}^{n+1}\mathbf{v}^{n+1,j} = \mathbf{r}_{\mathbf{d}}^{n+1,j}$ and perform a couple of matrix-vector multiplications and a vector-vector sum of Eq. (37). We later show, through several numerical simulations, that this approach is numerically stable. Even more importantly, our scheme is appropriate for the whole heartbeat, as it does not require adaptations according to the specific cardiac phase.

Moreover, our approach allows for a segregated solution of the 3D-0D coupled model, which is instead typically solved through a monolithic strategy [50]. As a matter of fact, segregated schemes available in literature that couple a mechanical problem with a model describing the dynamics of a fluid (even when described through a 0D circulation model) generally fail when the fluid domain is fully enclosed by the solid structure, because the incompressibility constraint of the fluid is no longer satisfied after the structure update [50]. This is known as balloon dilemma and affects also cardiac chambers, either when coupled with a 3D circulation model – within a fluid-structure interaction framework [90,91] – or with a 0D one. To overcome it, the 3D-0D cardiac circulation models available in literature rely either on a monolithic solution of the two models, where the 0D and 3D models are simultaneously discretized as a unique system and then typically solved by a Newton method [50] or iterative methods that progressively update the cavity pressures and the solid displacement, until convergence is reached. For instance, in [92], the authors proposed a method where the cavity pressure is initially estimated by extrapolating from previous time steps. Then, the cavity compliance (i.e. $\partial V / \partial p$, where $p$ and $V$ are the cavity pressure and volume, respectively) is estimated by finite differences and is used to update the pressure until the blood flux of the 3D model matches that of the 0D model within a prescribed tolerance. Similarly, in [37,38], during the isovolumic phases, the cavity pressure is iteratively updated by a fixed point scheme. However, convergence of this scheme depends upon a relaxation parameter, whose optimal value needs to be manually assessed from case to case [37].

With our approach, instead, the mechanical 3D model ($\mathscr{M}$) and the circulation 0D model ($\mathscr{C}$) are solved in both a segregated and staggered manner. Indeed, we do not solve the ($\mathscr{M}$) model simultaneously to the ($\mathscr{C}$) model, but coupled to the volume-consistency condition ($\mathscr{V}$) instead. In this way we end up with the saddle-point problem (34). Thanks to the above algorithm, finally, at each Newton iteration, we only need to solve a linear system involving the Jacobian matrix of the ($\mathscr{M}$) problem, and perform a couple of matrix-vector operations.

### 4.4. Stresses computation

Starting from [37], we define the following indicator for evaluating the components of the mechanical stress:

$$S_{\mathrm{ab}} = (\mathbf{P}\mathbf{a}_0) \cdot \frac{\mathbf{F}\mathbf{b}_0}{|\mathbf{F}\mathbf{b}_0|}, \tag{38}$$

where $a, b \in \{f, s, n\}$ indicate the fiber ($f$), the sheet ($s$) and the crossfiber ($n$) direction respectively. The metric $S_{\mathrm{ab}}$ measures the stress component in the $\mathbf{b}$ direction (where $\mathbf{b} = \frac{\mathbf{F}\mathbf{b}_0}{|\mathbf{F}\mathbf{b}_0|}$ denotes the direction $\mathbf{b}_0$ in the current configuration) across a surface normal to the direction $\mathbf{a}_0$. Hence, we refer to axial stresses when $a = b$, whereas we get shear stresses when $a \neq b$. We remark that in the active stress framework, $\mathbf{P}$ incorporates an additive decomposition between the passive and the active terms, the latter coming from the active tension $T_{\mathrm{a}}$.

Even though a possible strategy to handle the calculation of the stress tensor would be to solve a $L^2$-projection problem [37], we represent each component as a piece-wise constant ($\mathbb{Q}_0$) Finite Element vector, where the average of the values over the quadrature points of each cell is associated with the only local degree of freedom corresponding to the cell centroid. Since the stresses are only processed for visualization purposes, our strategies turn out to be very efficient while not hampering the accuracy of the computation.

## 5. Recovering the reference stress-free configuration

Here we present the algorithm for recovering the reference configuration $\Omega_0$ from the deformed configuration $\widetilde{\Omega}$, knowing that the latter is obtained from the former by applying a pressure $\widetilde{p}$ and an active tension $\widetilde{T}_{\mathrm{a}}$. The steady state version of the PDE for cardiac mechanics is reported in Eq. (11). In what follows, we denote by $\mathbf{d} = \mathbf{d}_{\mathrm{eq}}(\mathbf{x}_0, p_{\mathrm{LV}}, T_{\mathrm{a}})$ the equilibrium solution of Eq. (11) obtained on the computational domain of coordinate $\mathbf{x}_0$. Hence, our aim is finding a coordinate $\mathbf{x}_0$ such that $\mathbf{x}_0 + \mathbf{d}_{\mathrm{eq}}(\mathbf{x}_0, p_{\mathrm{LV}}, T_{\mathrm{a}}) = \widetilde{\mathbf{x}}$.
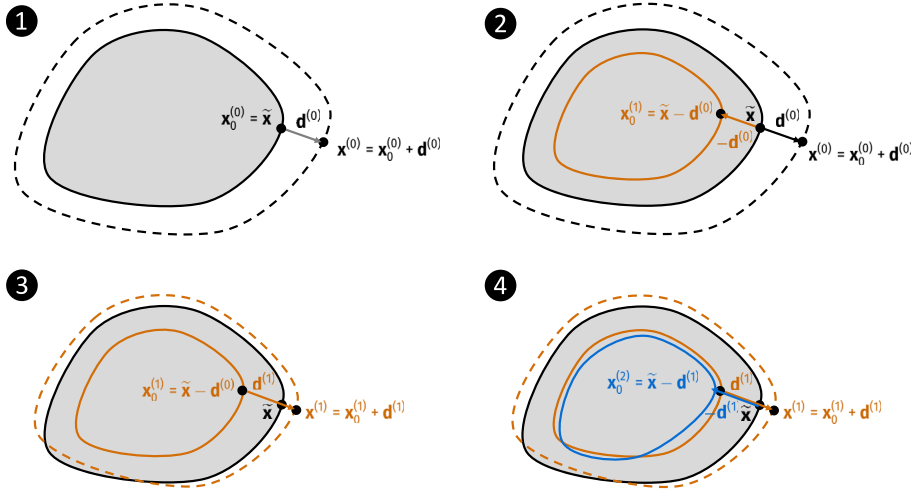
**Fig. 6.** Visual representation of the basic version of the fixed-point algorithm (see Algorithm 1).

---

**Algorithm 1** Reference configuration recovery (basic version).

---

**parameters:** $k_{max}, \epsilon_{tol}$
**output:** converged_RCB, $\mathbf{x}_0$

**procedure** REFERENCECONFIGURATIONBASE($\widetilde{\mathbf{x}}, \widetilde{p}, \widetilde{T}_a$)
    $\mathbf{x}_0^{(0)} \leftarrow \widetilde{\mathbf{x}}$
    **for** $k = 0, \ldots, k_{max}$ **do**
        (converged_SSM, $\mathbf{d}^{(k)}$) $\leftarrow$ STEADYSTATEMECHANICS($\mathbf{x}_0^{(k)}, \widetilde{p}, \widetilde{T}_a$)
        **if not** converged_SSM **then**
            **return** (false, $\mathbf{0}$)             ▷ Newton method does not converge.
        **end if**
        $\mathbf{x}^{(k)} \leftarrow \mathbf{x}_0^{(k)} + \mathbf{d}^{(k)}$
        **if** $\|\mathbf{x}^{(k)} - \widetilde{\mathbf{x}}\| \leq \epsilon_{tol} \|\mathbf{d}^{(k)}\|$ **then**
            **return** (true, $\mathbf{x}_0^{(k)}$)             ▷ Fixed-point converged.
        **end if**
        $\mathbf{x}_0^{(k+1)} \leftarrow \widetilde{\mathbf{x}} - \mathbf{d}^{(k)}$             ▷ Fixed-point update.
    **end for**
    **return** (false, $\mathbf{0}$)             ▷ Maximum number of iterations reached.
**end procedure**

---

### 5.1. Algorithm for the recovery of the reference configuration

A representation of this algorithm is shown in Fig. 6. We start by setting the coordinate of the reference configuration $\mathbf{x}_0$ equal to the coordinate of the deformed one (i.e. $\mathbf{x}_0^{(0)} = \widetilde{\mathbf{x}}$). Then, we solve the elastostatic problem of Eq. (11), and we get the displacement $\mathbf{d}^{(0)} = \mathbf{d}_{eq}(\mathbf{x}_0^{(0)}, p_{LV}, T_a)$ (Fig. 6, top-left). Since, when the configuration $\widetilde{\Omega}$ is recorded the active tension $\widetilde{T}_a$ is almost zero, in the deformed configuration $\mathbf{x}^{(0)} = \mathbf{x}_0^{(0)} + \mathbf{d}^{(0)}$ the ventricle is inflated compared to the configuration $\widetilde{\mathbf{x}}$. Thus, with the aim of correcting the mismatch between $\mathbf{x}^{(0)}$ and $\widetilde{\mathbf{x}}$, we deflate the ventricle by setting $\mathbf{x}_0^{(1)} = \mathbf{x}_0^{(0)} + (\widetilde{\mathbf{x}} - \mathbf{x}^{(0)}) = \widetilde{\mathbf{x}} - \mathbf{d}^{(0)}$ (Fig. 6, top-right). Then, we proceed by iterating the above steps. More precisely, for $k \geq 1$, we compute $\mathbf{d}^{(k)} = \mathbf{d}_{eq}(\mathbf{x}_0^{(k)}, p_{LV}, T_a)$ (Fig. 6, bottom-left) and we set $\mathbf{x}_0^{(k+1)} = \widetilde{\mathbf{x}} - \mathbf{d}^{(k)}$ (Fig. 6, bottom-right), stopping when the difference between two consecutive iterations is sufficiently small.

The whole procedure is reported in Algorithm 1, where we denote the function that solves problem (11) on the geometry with coordinates $\mathbf{x}_0$ as STEADYSTATEMECHANICS. The latter function solves the nonlinear system by means of the Newton method. In case the Newton iterations do not reach convergence (according to a criterion based both on the residual and on the difference between two consecutive iterations), it returns a flag to indicate failure of the algorithm. More precisely, the function signature reads

$$(\text{converged\_SSM}, \mathbf{d}) = \text{STEADYSTATEMECHANICS}(\mathbf{x}_0, p_{LV}, T_a)$$

where, in case of convergence, converged_SSM is true and $\mathbf{d} = \mathbf{d}_{eq}(\mathbf{x}_0, p_{LV}, T_a)$, while in case of non convergence converged_SSM is false and $\mathbf{d}$ is not used. We remark that an algorithm similar to Algorithm 1 is presented in [40].

Algorithm 1 can be interpreted as a fixed-point iteration scheme. Indeed, the fixed-point $\mathbf{x}_0$ of the map defined by the Algorithm 1 iteration satisfies $\mathbf{x}_0 = \widetilde{\mathbf{x}} - \mathbf{d}_{eq}(\mathbf{x}_0, p_{LV}, T_a)$. The fixed-point iterations of Algorithm 1 are sketched in Fig. 7. The
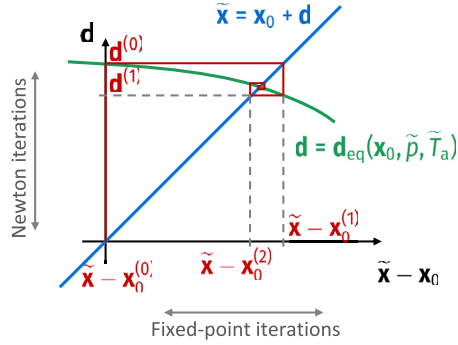
**Fig. 7.** Representation of the basic version of the reference configuration recovery algorithm (Algorithm 1).
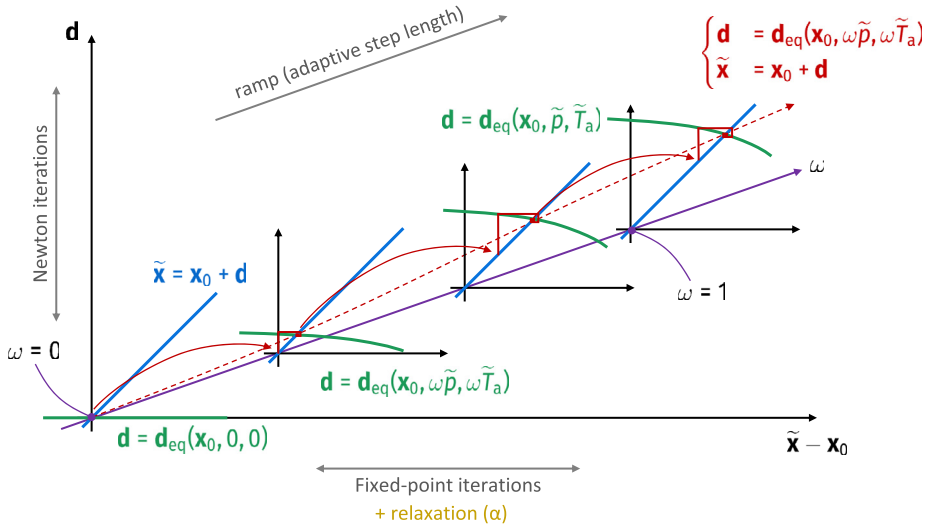


**Fig. 8.** Representation of the enhanced version of the reference configuration recovery algorithm (see Algorithms 2 and 3).

solution is obtained as the intersection between the line $\widetilde{\mathbf{x}} = \mathbf{x}_0 + \mathbf{d}$ and the manifold $\mathbf{d} = \mathbf{d}_{eq}(\mathbf{x}_0, p_{LV}, T_a)$. The algorithm proceeds iteratively in the space $(\mathbf{x}_0, \mathbf{d})$: the first variable is updated by the fixed-point iterations (horizontal axis of Fig. 7), while the second variable is updated by Newton iterations (vertical axis of Fig. 7).

However, the implementation shown in Algorithm 1 has several limitations when applied to realistic heart geometries and to highly nonlinear constitutive laws, such as in the case of cardiac mechanics. In fact, both the Newton method employed in SteadyStateMechanics and the fixed-point scheme employed in ReferenceConfigurationBase do not converge if the initial guess is not "sufficiently" close to the solution. In particular, our experience revealed that the attraction basin of the fixed-point iterations scheme gets smaller and smaller as the value of $p_{LV}$ grows and as $h$ decreases.

For a geometry with 4'588 elements (see Sec. 6 for details), the algorithm terminates successfully for $\widetilde{p} = 350$ Pa $\simeq$ 2.62 mmHg, but fails for $\widetilde{p} = 400$ Pa $\simeq$ 3 mmHg. Refining the geometry with one splitting level (36'704 elements), the algorithm succeeds up to $\widetilde{p} = 50$ Pa $\simeq$ 0.37 mmHg, but fails already for $\widetilde{p} = 100$ Pa $\simeq$ 0.75 mmHg. Therefore, we conclude that Algorithm 1 is unsuitable for realistic cardiac geometries.

For these reasons, we improved Algorithm 1 by increasing its robustness through several strategies. We propose in Algorithm 2 the enhanced version of Algorithm 1. First, we introduced a relaxation parameter $\alpha \in (0, 1]$ in the fixed-point iteration, by rewriting it as $\mathbf{x}_0^{(k)} \leftarrow \mathbf{x}_0^{(k-1)} + \alpha(\widetilde{\mathbf{x}} - \mathbf{x}^{(k-1)})$. We update $\alpha$ adaptively as written in Algorithm 3: in case of non-convergence of the Newton iterations, we repeat the last fixed-point iteration for a smaller value of $\alpha$; in case of convergence, we increase it in the next iteration. Moreover, the fixed-point iterations are nested inside an outer loop, in which we progressively increase the value of $p_{LV}$ and $T_a$ until the target value $\widetilde{p}$ and $\widetilde{T}_a$ is reached (continuation method). In this outer loop, we adaptively change the step $\omega^{(k)}$, by decreasing it in case of failure of the inner fixed-point loop and increasing it in case of success.

We remark that after each failure of either SteadyStateMechanics or FixedPoint function, we reset the value of $\mathbf{d}$ to the last solution of Eq. (11). This ensures the success of such continuation strategy, by which we move in the space $(\mathbf{x}_0, \mathbf{d}, \omega)$ staying close to the intersection of the curves $\mathbf{d} = \widetilde{\mathbf{x}} - \mathbf{x}_0$ and $\mathbf{d} = \mathbf{d}_{eq}(\mathbf{x}_0, \omega p_{LV}, \omega T_a)$ (see Fig. 8).

---

**Algorithm 2** Reference configuration recovery (enhanced version).

---

**parameters:** $k_{\max}, \epsilon_{\text{tol}}^{\text{ramp}}, \epsilon_{\text{tol}}^{\text{final}}, \gamma_\omega^+, \gamma_\omega^-, \Delta\omega_{\max}$
**output:** `converged_RC`, $\mathbf{x}_0$

**procedure** REFERENCECONFIGURATION($\widetilde{\mathbf{x}}, \widetilde{p}, \widetilde{T}_a$)
    $\mathbf{x}_0^{(0)} \leftarrow \widetilde{\mathbf{x}}$
    $\omega^{(0)} \leftarrow 0$
    $\Delta\omega \leftarrow \Delta\omega_{\max}$
    **for** $k = 0, \ldots, k_{\max}$ **do**
        $\omega^{(k)} \leftarrow \min(\omega^{(k-1)} + \Delta\omega, 1)$
        **if** $\omega^{(k)} = 1$ **then**
            $\epsilon_{\text{tol}} \leftarrow \epsilon_{\text{tol}}^{\text{final}}$
        **else**
            $\epsilon_{\text{tol}} \leftarrow \epsilon_{\text{tol}}^{\text{ramp}}$
        **end if**
        (`converged_FP`, $\mathbf{x}_0^{(k)}$) $\leftarrow$ FIXEDPOINT($\widetilde{\mathbf{x}}, \omega^{(k)}\widetilde{p}, \omega^{(k)}\widetilde{T}_a \mathbf{x}_0^{(k-1)}, \epsilon_{\text{tol}}$)
        **if** `converged_FP` **then**
            **if** $\omega^{(k)} = 1$ **then**
                **return** (true, $\mathbf{x}_0^{(k)}$)                           ▷ Ramp converged.
            **end if**
            $\Delta\omega \leftarrow \min(\gamma_\omega^+ \Delta\omega, \Delta\omega_{\max})$
        **else**
            $\Delta\omega \leftarrow \gamma_\omega^- \Delta\omega$
        **end if**
    **end for**
    **return** (false, $\mathbf{0}$)                                ▷ Maximum number of iterations reached.
**end procedure**

---

**Algorithm 3** Inner fixed-point loop of the reference configuration recovery algorithm.

---

**parameters:** $k_{\max}, \alpha_{\min}, \alpha_{\max}, \gamma_\alpha^+, \gamma_\alpha^-$
**output:** `converged_FP`, $\mathbf{x}_0$

**procedure** FIXEDPOINT($\widetilde{\mathbf{x}}, p_{\text{LV}}, T_a, \mathbf{x}_0, \epsilon_{\text{tol}}$)
    $\mathbf{x}_0^{(0)} \leftarrow \mathbf{x}_0$
    $\alpha \leftarrow \alpha_{\max}$
    (`converged_SSM`, $\mathbf{d}^{(0)}$) $\leftarrow$ STEADYSTATEMECHANICS($\mathbf{x}_0^{(0)}, p_{\text{LV}}, T_a$)
    **if not** `converged_SSM` **then**
        **return** (false, $\mathbf{0}$)
    **end if**
    **for** $k = 0, \ldots, k_{\max}$ **do**
        $\mathbf{x}_0^{(k)} \leftarrow \mathbf{x}_0^{(k-1)} + \alpha(\widetilde{\mathbf{x}} - \mathbf{x}^{(k-1)})$                       ▷ Fixed-point update.
        (`converged_SSM`, $\mathbf{d}^{(k)}$) $\leftarrow$ STEADYSTATEMECHANICS($\mathbf{x}_0^{(k)}, \widetilde{p}, \widetilde{T}_a$)
        **if** `converged_SSM` **then**
            $\mathbf{x}^{(k)} \leftarrow \mathbf{x}_0^{(k)} + \mathbf{d}^{(k)}$
            **if** $\|\mathbf{x}^{(k)} - \widetilde{\mathbf{x}}\| \leq \epsilon_{\text{tol}}\|\mathbf{d}^{(k)}\|$ **then**
                **return** (true, $\mathbf{x}_0^{(k)}$)                     ▷ Fixed-point converged.
            **end if**
            $\alpha \leftarrow \min(\gamma_\alpha^+ \alpha, \alpha_{\max})$
        **else**
            $\alpha \leftarrow \max(\gamma_\alpha^- \alpha, \alpha_{\min})$
        **end if**
    **end for**
    **return** (false, $\mathbf{0}$)                               ▷ Maximum number of iterations reached.
**end procedure**

---

### 5.2. Projection of the reference configuration from a coarser mesh

The procedure to recover the reference configuration (Algorithm 2) requires to numerically solve the elastostatic problem of Eq. (11) multiple times, until the fixed point algorithm converges. According to our experience, this procedure can be very computationally demanding in cardiac applications, especially if realistic human heart geometries and fine representations of the computational domain need to be considered. To overcome this issue, the reference configuration recovery algorithm can be run on a coarser mesh compared to the couple of nested meshes $\mathcal{T}_{h_2}$-$\mathcal{T}_{h_1}$ used for the electromechanical model. A natural choice can be to exploit once again the efficient hierarchical octree structure, but starting from a coarser level $h_3$, generating accordingly the triad of nested meshes $\mathcal{T}_{h_3}$-$\mathcal{T}_{h_2}$-$\mathcal{T}_{h_1}$. However, a further level of coarsening would imply a loss of geometric accuracy that is propagated also into the finer couple of meshes $\mathcal{T}_{h_2}$-$\mathcal{T}_{h_1}$, affecting the electromechanical model.

For this reason, we propose a projection technique which enables to map to the reference configuration $\Omega_0$ from a coarser non-nested mesh. This mesh – named $\mathcal{T}_{\widetilde{h}_3}$ – can be independently generated with a mesh size $\widetilde{h}_3$ such that $h_2 <$
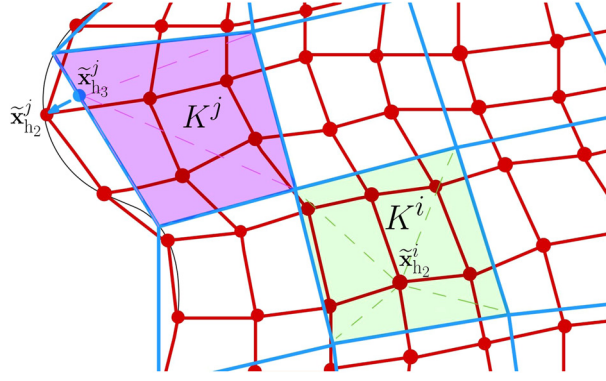
**Fig. 9.** A sketch of the projection procedure from a coarse mesh $\mathcal{T}_{\widetilde{h}_3}$ (in blue) into a finer mesh $\mathcal{T}_{h_2}$ (in red): on the internal points $\widetilde{\mathbf{x}}_{h_2}^i \in \mathcal{T}_{h_2}$ we recover the value by exploiting the basis functions of the element $K^i \in \mathcal{T}_{\widetilde{h}_3}$ (in green); on the external points $\widetilde{\mathbf{x}}_{h_2}^j \in \mathcal{T}_{h_2}$ we project the value of the closest point $\widetilde{\mathbf{x}}_{\widetilde{h}_3}^j \in \mathcal{T}_{\widetilde{h}_3}$ evaluated on the closest element $K^j \in \mathcal{T}_{\widetilde{h}_3}$ (in purple).

$\widetilde{h}_3 < h_3$. Such strategy provides the advantages of having more flexibility on the choice of the mesh size $\widetilde{h}_3$ and of preserving the geometric accuracy for the electromechanical meshes $\mathcal{T}_{h_2}$-$\mathcal{T}_{h_1}$.

The complete procedure consists of the following steps:

1. generate two non-nested computational meshes $\mathcal{T}_{h_2}$ and $\mathcal{T}_{\widetilde{h}_3}$ from the deformed configuration $\widetilde{\Omega}$, i.e. the one reconstructed from the medical images, such that $h_2 < \widetilde{h}_3$. The former is characterized by the target mesh size for the mechanical simulation.
2. solve the reference configuration recovery (Algorithm 2) on the coarser mesh $\mathcal{T}_{\widetilde{h}_3}$, obtaining the displacement field $\mathbf{d}_{\widetilde{h}_3}$;
3. project the displacement $\mathbf{d}_{\widetilde{h}_3}$ on the finer mesh $\mathcal{T}_{h_2}$ obtaining the field $\widehat{\mathbf{d}}_{h_2}$, which approximates the displacement $\mathbf{d}_{h_2}$, i.e. the one that would be computed if the reference configuration recovery (Algorithm 2) is applied directly on the finer mesh $\mathcal{T}_{h_2}$;
4. move each vertex of the mesh $\mathcal{T}_{h_2}$ according to $\mathbf{x}_0 = \widetilde{\mathbf{x}} - \widehat{\mathbf{d}}_{h_2}$, recovering the computational mesh $\mathcal{T}_{h_2}$ that describes the reference configuration $\Omega_0$;
5. hierarchically refine $\mathcal{T}_{h_2}$ to generate the fine mesh $\mathcal{T}_{h_1}$ for the electrophysiology.

We remark that the projection (step 3) is necessary despite both $\mathcal{T}_{h_2}$ and $\mathcal{T}_{\widetilde{h}_3}$ describe the same domain $\widetilde{\Omega}$. Indeed, in practice, their boundaries do not match, since they are independent polygonal surfaces made of piecewise linear elements. Thus, some vertexes of $\mathcal{T}_{h_2}$ can lie outside $\mathcal{T}_{\widetilde{h}_3}$, as illustrated in the 2D sketch of Fig. 9. As a consequence, to recover $\widehat{\mathbf{d}}_{h_2}$ in all the vertexes of the mesh $\mathcal{T}_{h_2}$, we proceed in a different way if these vertexes lie inside or outside $\mathcal{T}_{\widetilde{h}_3}$. In particular:

- for the internal vertexes – denoted as $\widetilde{\mathbf{x}}_{h_2}^i$, $i = 0, 1, 2, \ldots$ – it is sufficient to find the element $K^i \in \mathcal{T}_{h_3}$ such that $K^i \ni \widetilde{\mathbf{x}}_{h_2}^i$ and evaluate $\mathbf{d}_{h_3}(\widetilde{\mathbf{x}}_{h_2}^i)$ exploiting its Finite Element expansion on $K^i$ (see Fig. 9, green element);
- conversely, for each external point – denoted as $\widetilde{\mathbf{x}}_{h_2}^j$, $j = 0, 1, 2, \ldots$ – more sub-steps are necessary, (see Fig. 9, purple element):
    1. we find the closest element $K^j \in \mathcal{T}_{\widetilde{h}_3}$ from the external point $\widetilde{\mathbf{x}}_{h_2}^j$;
    2. on $K^j$ we find the closest point $\widetilde{\mathbf{x}}_{h_3}^j$ to $\widetilde{\mathbf{x}}_{h_2}^j$;
    3. we evaluate $\mathbf{d}_{h_3}(\widetilde{\mathbf{x}}_{h_3}^j)$ and we project the resulting value into the external point $\widetilde{\mathbf{x}}_{h_2}^j$.

From the implementation point of view, this projection is performed by exploiting the *VTK* library [93] in our Finite Element library life$^\text{x}$ (https://lifex.gitlab.io/lifex). *VTK* filtering utilities allow to locate all internal points, which are the majority, in a really fast way. Moreover, the *VTK* library is efficient in performing closest points interpolation, leading to a very fast projection procedure. However, we remark that the hierarchical octree structure [46,85] still remains more effective for electromechanical simulations, where the exchange of information between (nested) meshes occurs at each time step. Indeed, the projection presented here is intended to be a single pre-processing step to be performed before the non-stationary electromechanical simulation. An example of this projection in a left ventricle is shown in Sect. 6.1.

## 6. Numerical results

In this section, we present several electromechanical simulations obtained with a left ventricle geometry that is preprocessed from the Zygote Solid 3D heart model [52], which represents the 50$^\text{th}$ percentile of a healthy Caucasian male in the

U.S., reconstructed from a high resolution computed tomography scan. This model has been acquired at 70% of diastole, i.e. in the last part of the diastasis phase, when the initial passive filling of the heart's ventricles has slowed, but before the atria contract to complete the active filling.

First, we show an example of projection of the reference configuration from a coarser mesh by exploiting the method detailed in Sec. 5.2. Then, we show that our mathematical model can generate several scenarios according to the chosen parameter sets: specifically, we vary preload, afterload and contractility, and we evaluate the effects of these changes on the PV loops of the left ventricle.

We consider a fine mesh $\mathcal{T}_{h_1}$ for cardiac electrophysiology which consists of 2'590'464 DOFs and 2'663'817 vertices ($h_{\mathrm{mean}} = 0.75$ mm), while the coarse mesh $\mathcal{T}_{h_2}$ for cardiac mechanics is endowed with 40'476 DOFs and 47'529 vertices ($h_{\mathrm{mean}} = 3$ mm). Specifically, the fine mesh is obtained by two recursive splitting of each element of the coarse one. The mesh $\mathcal{T}_{h_2}$ is generated with `vmtk` (www.vmtk.org) [94], by exploiting the recently proposed tools for cardiac mesh generation [95].

The numerical methods of Sec. 4 have been implemented in `life`<sup>x</sup> (https://lifex.gitlab.io/lifex), a high-performance C++ library developed within the iHEART project[1] and based on the `deal.II` (https://www.dealii.org) Finite Element core [96]. The numerical simulations have been obtained by employing `life`<sup>x</sup> in a parallel setting, using either a HPC resource available at MOX (48 Intel Xeon ES-2640 CPUs) or the GALILEO supercomputer from Cineca (7 nodes endowed with 36 Intel Xeon E5-2697 v4 2.30 GHz CPUs, for a total number of 252 cores).

We apply a current $\widetilde{\mathcal{I}}_{\mathrm{app}}(\boldsymbol{x}, t)$, distributed in space as a Gaussian with peak $\widetilde{\mathcal{I}}_{\mathrm{app}}^{\mathrm{max}}$, for a duration of $t_{\mathrm{app}}$, in three different regions of the myocardium to trigger the electrical signal in the left ventricle. These regions are located at the central distance between the apex and the base of the ventricle. Even if we do not model the Purkinje network [68,69], the electrical activation of the tissue that we propose is known to provide comparable results in terms of mechanical indicators, such as displacement magnitude and blood volume over time, and minor differences in the activation maps [67]. We use the Bayer-Blake-Plank-Trayanova algorithm [71,73] to generate the fiber distribution (field $\mathbf{f}_0$) for our geometry, using $\alpha_{\mathrm{epi}} = -60°$, $\alpha_{\mathrm{endo}} = 60°$, $\beta_{\mathrm{epi}} = 20°$ and $\beta_{\mathrm{endo}} = -20°$. In all numerical tests, we set for simplicity $p_{\mathrm{EX}}(t) \equiv 0$. All the parameters related to the monodomain equation and passive mechanics are reported in Tables 1 and 2 respectively. We use a time step $\Delta t_1 = 50$ μs for electrophysiology, activation and circulation, whereas mechanics is solved in time with a time step $\Delta t_2 = 250$ μs. Further information about the parameters of both linear and nonlinear solvers is reported in Appendix B.

### 6.1. Projection of the reference configuration

We discuss the results of the linear projection of the reference configuration (Sect. 5.2) by running the recovery of reference configuration (Algorithm 2) for the Zygote left ventricle geometry. In particular, we consider the following mesh configurations:

- *config1*: a triad of nested meshes $\mathcal{T}_{h_3}$-$\mathcal{T}_{h_2}$-$\mathcal{T}_{h_1}$; the coarsest one for the recovery algorithm, the intermediate one for mechanics and the finer one for electrophysiology;
- *config2*: an independent coarser mesh $\mathcal{T}_{\widetilde{h}_3}$ for the recovery algorithm, and a couple of nested meshes $\mathcal{T}_{h_2}$-$\mathcal{T}_{h_1}$ for the electromechanical model;
- *config3*: a couple of nested meshes $\mathcal{T}_{h_2}$-$\mathcal{T}_{h_1}$ for the electromechanical model, where the mesh $\mathcal{T}_{h_2}$ is used also for the recovery algorithm.

In Fig. 10, we show the results of the recovery algorithm on these three configurations, choosing $h = 3$ mm as target mesh size for mechanics (i.e. $\mathcal{T}_{h_2}$). More in detail, we create an ad-hoc hierarchical triad $\mathcal{T}_{h_3}$ ($h_{\mathrm{mean}} = 6$ mm)-$\mathcal{T}_{h_2}$ ($h_{\mathrm{mean}} = 3$ mm)-$\mathcal{T}_{h_1}$ ($h_{\mathrm{mean}} = 0.75$ mm) for *config1*. While *config2* and *config3* exploit the hierarchical dyad $\mathcal{T}_{h_2}$ ($h_{\mathrm{mean}} = 3$ mm)-$\mathcal{T}_{h_1}$ ($h_{\mathrm{mean}} = 0.75$ mm), $\mathcal{T}_{\widetilde{h}_3}$ for *config2* contains 15'764 DOFs and 19'099 vertices ($h_{\mathrm{mean}} = 4$ mm).

The displacement field $\mathbf{d}_{h_2}$ of *config3* represents the reference result since it is obtained by running directly the recovery algorithm on $\mathcal{T}_{h_2}$, i.e. the finer mesh that we consider. On the contrary, *config1* presents a large loss of geometric accuracy, which is propagated into the two meshes $\mathcal{T}_{h_2}$-$\mathcal{T}_{h_1}$ of the electromechanical model. Indeed, $\mathcal{T}_{h_3}$ appears too sharp and not realistic, especially at the base and at the apex. Moreover, the displacement field $\mathbf{d}_{h_3}$ computed on $\mathcal{T}_{h_3}$ is qualitative different from the reference one ($\mathbf{d}_{h_2}$, *config3*).

In *config2*, we first compute the displacement field $\mathbf{d}_{\widetilde{h}_3}$ on the independent coarse mesh $\mathcal{T}_{\widetilde{h}_3}$, and then we obtain the projected field $\widehat{\mathbf{d}}_{h_2}$ on $\mathcal{T}_{h_2}$ by exploiting the linear projection procedure (Sect. 5.2). The projected field $\widehat{\mathbf{d}}_{h_2}$ features a good qualitative match with the field $\mathbf{d}_{h_2}$. More quantitatively, we obtain an average error $|\mathbf{d}_{h_2} - \widehat{\mathbf{d}}_{h_2}| = 0.105$ mm. This quantity is lower than the standard resolution of cardiac medical images (about 0.5 mm for high-quality acquisition). Thus, we can consider this error lower than the geometric uncertainty when dealing with patient-specific simulations. Moreover, being $\mathcal{T}_{\widetilde{h}_3}$ made of a considerable lower number of elements if compared to $\mathcal{T}_{h_2}$, *config2* saves a large amount of computational time for the execution of Algorithm 2, compared to *config3*.
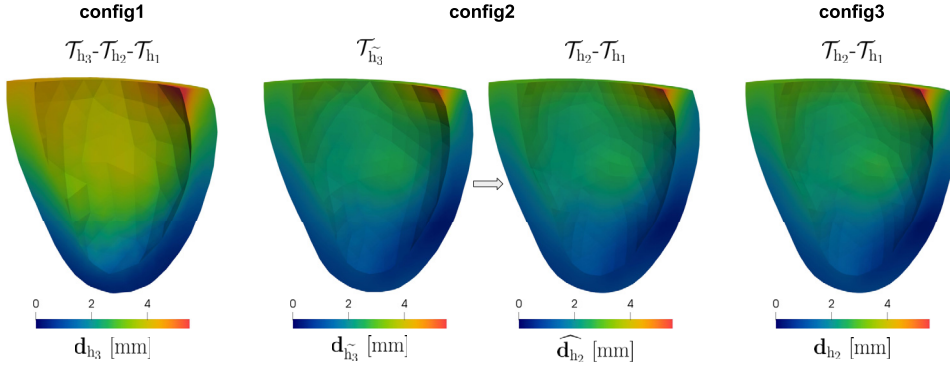
**Fig. 10.** Solving the reference configuration recovery (Algorithm 2) for three different settings, with a common target mesh size for the mechanical simulation ($\mathcal{T}_{h_2}$, $h = 3$ mm): in *config1* we apply the recovery algorithm on the coarsest mesh of a triad of hierarchical nested meshes ($\mathcal{T}_{h_3}$, $h = 6$ mm); in *config2* the algorithm runs on an independent coarse mesh ($\mathcal{T}_{\tilde{h}_3}$, $h = 4$ mm) and the displacement is projected onto $\mathcal{T}_{h_2}$; in *config3* we compute the reference configuration directly on $\mathcal{T}_{h_2}$.

*Config2* is the cheapest procedure in terms of total computational cost, moreover it presents a negligible error and does not affect the geometrical accuracy of the electromechanical model. We conclude by recommending this setting when a fine patient-specific mesh is employed for the mechanical problem.

### 6.2. Tests cases varying preload, afterload and contractility

We test the response of our electromechanical model to some scenarios of clinical interest. The parameters of the baseline simulation are reported in Appendix A. Starting from this setting, we consider three physiologically relevant scenarios, aimed at investigating the effects of changes in preload, afterload and myocardial contractility, respectively. In all the cases, we simulate 10 heartbeats, until when we reach a limit cycle, that is a periodic regime. However, we report only the PV loops related to the last cardiac cycle.

#### 6.2.1. Baseline simulation

In Fig. 11 we report the time evolution of both the transmembrane potential $V$ and the displacement magnitude $|\mathbf{d}|$ in the Zygote left ventricle, considering the last heartbeat of the simulation. We compute the initial displacement $\mathbf{d}_0$ by inflating $\Omega_0$ until the desired end-diastolic pressure is reached. In practice, we accomplish this task by performing a pressure ramp on the quasi-static approximation of the mechanical problem.

In Fig. 12 we depict the axial stresses $S_{ff}$, $S_{ss}$ and $S_{nn}$, whereas in Fig. 13 we show the shear stresses $S_{fs}$, $S_{fn}$ and $S_{sf}$. We observe that $S_{ff}$ has a dominant role with respect to $S_{ss}$ and $S_{nn}$, especially during ejection (i.e. the second part of systole) and isovolumetric relaxation (i.e. early diastole). The same considerations hold for the shear stresses components involving the fiber field $f$.

In Figs. 14 and 15 we depict the pressure and volume traces for the four cardiac chambers, namely atria and ventricles. We notice that the stroke volume of both ventricles is comparable, with an ejection fraction $EF \approx 50\%$ that mimics the heart condition of an healthy adult. Same considerations hold for the pressure peaks of both ventricles during the ejection phase. Moreover, the PV loops of the atria show both the A-loop (driven by atrial contraction) and the V-loop (driven by ventricular relaxation).

#### 6.2.2. Test Case 1

We change the ventricles preload (i.e. their end-diastolic pressure) by modifying the value of the atrial contractility with respect to the baseline setting of Appendix A. More precisely, we consider the two cases when $E_{LA}^{act,max}$ and $E_{RA}^{act,max}$ are respectively increased and decreased by 50%. As shown in Fig. 16, the larger the atrial contractility, the more blood is injected in the ventricle, thus increasing preload. Moreover, our electromechanical model predicts a larger stroke volume for a larger preload. This is consistent with the so-called Frank-Starling effect, a self-regulatory mechanism that guarantees the balance between venous return and cardiac output [1].

#### 6.2.3. Test Case 2

We investigate the effects of changing the resistance of the arterial circulation. This mimics the situation of a patient affected by diseases associated with hypertension, such as arteriosclerosis, or to the effect of vasodilator-vasoconstrictor drugs. Starting from the baseline setting, we perform two additional simulations where we respectively increase and decrease by 15% the value of $R_{AR}^{SYS}$. In both cases, we modify the value of $C_{AR}^{SYS}$ accordingly, so that the product $R_{AR}^{SYS} C_{AR}^{SYS}$, corresponding to the characteristic time constant of the arterial system, is preserved. The results in Fig. 16 show that an increase of the arterial resistance yields larger values of both the aortic valve opening pressure and the maximal left ventricle pressure (hypertensive effect).
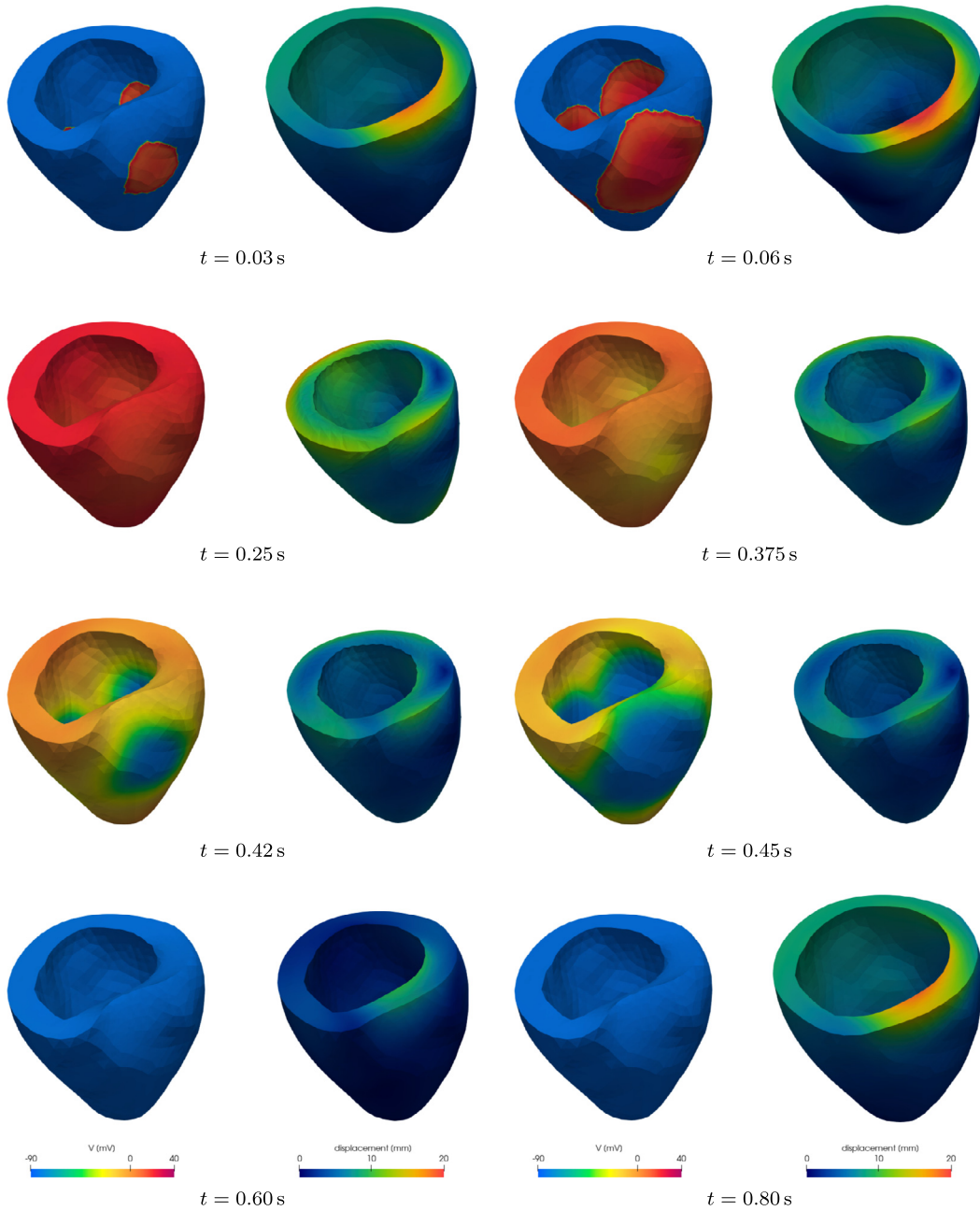
**Fig. 11.** Evolution of the transmembrane potential $V$ and the displacement magnitude $|\mathbf{d}|$ in the Zygote left ventricle during the last cardiac cycle of the baseline simulation. The right view of each picture is warped by the displacement vector. Conversely, the transmembrane potential $V$ is displayed on the reference configuration $\Omega_0$.

### 6.2.4. Test Case 3

We consider the response of our electromechanical model to either a positive or negative change in the inotropic state of the muscle, whose effect is that of increasing and, respectively, decreasing the myocardial contractility. Specifically, starting from the baseline, we first increment and then decrement the atrial contractility ($E_{LA}^{act,max}$ and $E_{RA}^{act,max}$) and the ventricular contractility ($T_a^{max}$ and $E_{RV}^{act,max}$) by 10%. The results in Fig. 16 show that an increase in myocardial contractility generates an increase of both the maximal left ventricle pressure and the stroke volume.

## 7. Conclusions

In this paper we presented a novel mathematical and numerical model for the simulation of cardiac electromechanics, where the different physical phenomena therein involved are described by means of biophysically detailed core models. We
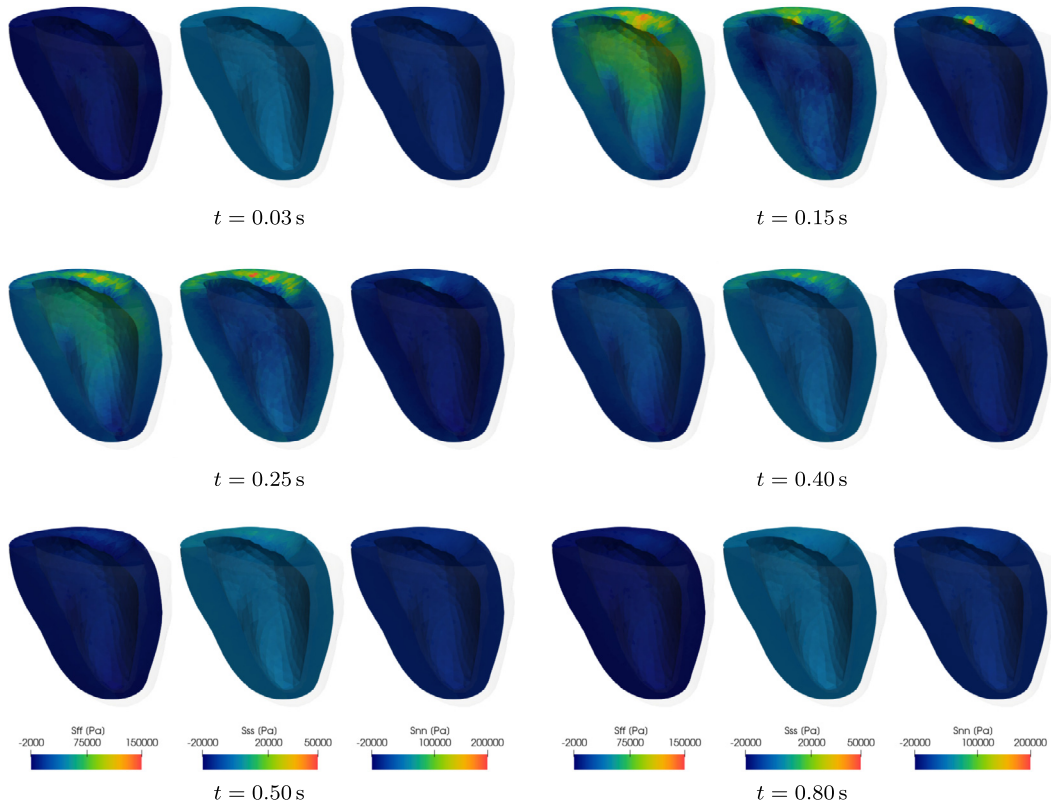
**Fig. 12.** Evolution of $S_{ff}$, $S_{ss}$, $S_{nn}$ during the last cardiac cycle of the baseline simulation.

showed that our 3D-0D closed-loop model fulfills the principle of conservation of mechanical energy. Indeed, the power exerted by the cavity pressure in the 3D electromechanical model balances the power exchanged with the 0D circulation model at the coupling interface.

We analyzed the mechanical work associated with the different compartments of our circulation model and we proved that a balance of mechanical energy is satisfied. This balance holds both when we consider the 0D circulation model alone and when we consider the 3D-0D coupled model. We showed that the circulation model considered in this paper can be exploited to provide quantitative insights into the heart energy distribution. In particular we employed this model to validate the reliability of relationships used in daily clinical practice to estimate the mechanical work performed by the heart. We highlighted that these relationships can be accurate when used to assess the ventricular function, but less accurate when the mechanical work of the whole myocardium is addressed.

The numerical schemes here proposed are aimed at coupling, in a computationally efficient and accurate manner, mathematical models with a significant degree of biophysical detail. Our computational framework is based on three main pillars, namely (1) IMEX schemes to approximate the single core physics; (2) an ANN-based emulator, built by Machine Learning on the basis of a collection of pre-computed simulations, that replaces computationally demanding biophysically detailed microscale models; (3) a fully partitioned coupling of the different core models. The advantages yielded by these features are the following:

- We designed IMEX schemes to minimize the number of nonlinear systems that need to be solved, using implicit solvers only for those core models that would otherwise lead to severe CFL restriction on the time step. In particular, our numerical scheme allows to update the variables of the ionic and activation models without the need of solving any algebraic system (neither nonlinear nor linear), and it allows to update the electrical potential by solving a single linear system at each time iteration. The unique nonlinear system of our mathematical model is associated with cardiac mechanics, for which explicit or semi-implicit schemes are unstable, unless a very fine time step is employed, because of the strong nonlinearities contained in the constitutive law [37].
- In our active stress model we replaced a biophysically detailed, but computationally demanding, subcellular model of active force generation by a surrogate model, based on an ANN [35]. This model, which is based on a Machine Learning approach from a collection of pre-computed simulations, allows to accurately reproduce the results of the high-fidelity model by reducing by a factor of 1'000 the number of internal variables [33,76]. In this way we obtain in
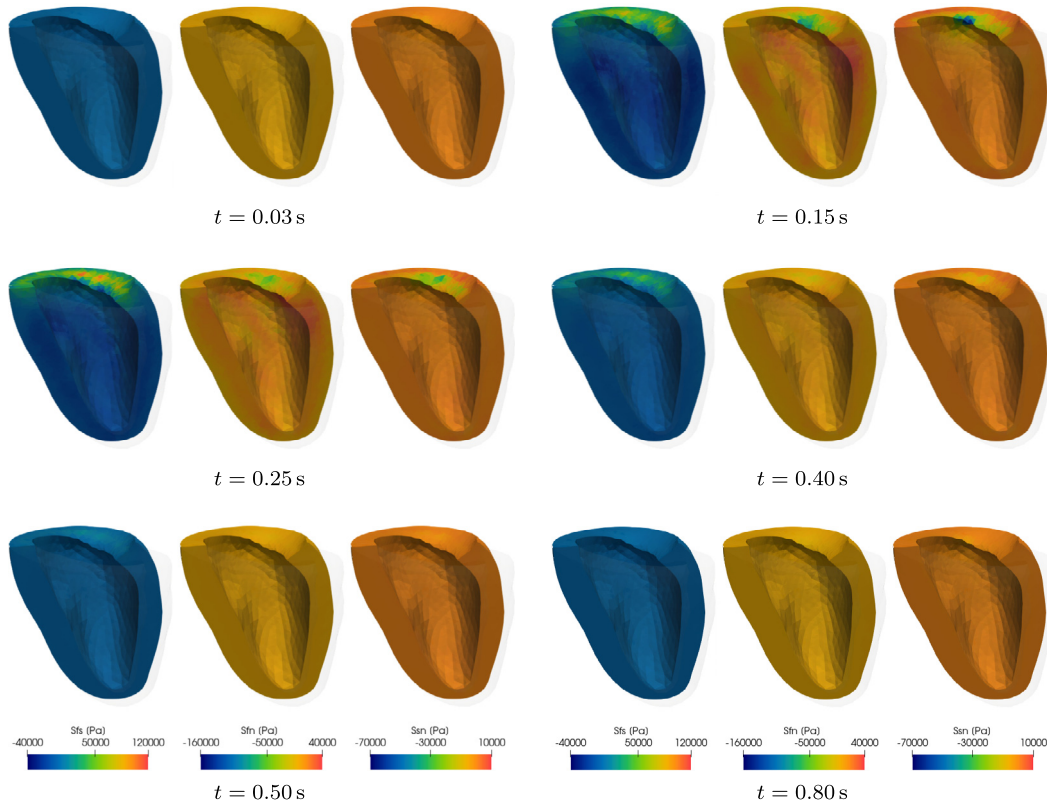
**Fig. 13.** Evolution of $S_{\text{fs}}$, $S_{\text{fn}}$ and $S_{\text{sn}}$ during the last cardiac cycle of the baseline simulation.

a very favorable trade-off between the biophysical accuracy of the results and the computational cost of our numerical simulations.

- We developed a novel scheme to couple the 3D electromechanical model with a 0D circulation model in a fully segregated manner. Our scheme does not incur in the *balloon dilemma* [50] – which affects segregated schemes wherein the displacement update is not aware of the incompressibility constraint of the enclosed fluid, thus possibly leading to the failure of the scheme [90,91] – by the introduction of a volumetric constraint on the solution of the mechanical problem. In this way, the cavity pressure can be reinterpreted as a Lagrange multiplier associated with the constraint, that enforces the coupling between the 0D circulation model and the 3D electromechanical model. At the algebraic level, we end up with a saddle-point problem, that we solve by means of Schur complement reduction [51].
- The fully segregated scheme proposed in this paper enables the use of different discretizations in space and time to approximate the variables associated with the different core models. This better reflects, at the numerical level, the typical space and time scales characterizing the associated physical phenomena. Specifically, we employ coarser spatial and temporal discretizations for the elastodynamic problem, which is characterized by larger characteristic temporal and spatial scales than the electrophysiological problem [14]. Moreover, it is the most demanding core model from the computational viewpoint, as it involves the solution of a nonlinear system and the time-consuming Jacobian matrix assembly [15].

Regarding the latter aspect, we employ a parallel and flexible intergrid transfer operator [14,46,47] that permits to interpolate the solution of a core model between nested meshes and among possibly different FEM spaces [46].

As a further new contribution, we introduced an algorithm to reconstruct the reference (i.e. stress-free) configuration of the left ventricle starting from a stressed configuration obtained from medical images, by solving a suitable inverse problem. Determining such configuration is essential to correctly initialize electromechanical simulations. This is especially useful in patient-specific scenarios where the end diastolic pressure and/or the end diastolic volume are possibly known.

Finally, we carried out several numerical simulations where we vary different parameters of the model to affect preload, afterload and contractility, thus investigating the response of our model for situations of clinical interest. Our model correctly reproduces the increase of stroke volume as a consequence of increased preload, coherently with the Frank-Starling law [1], thus guaranteeing the matching between the venous return and the cardiac output.

Albeit in this paper we focused on the left ventricle, the 3D-0D coupling that we describe (along with its numerical treatment) can be extended to a four chambers representation of the human heart, a model that we will pursue in forth-
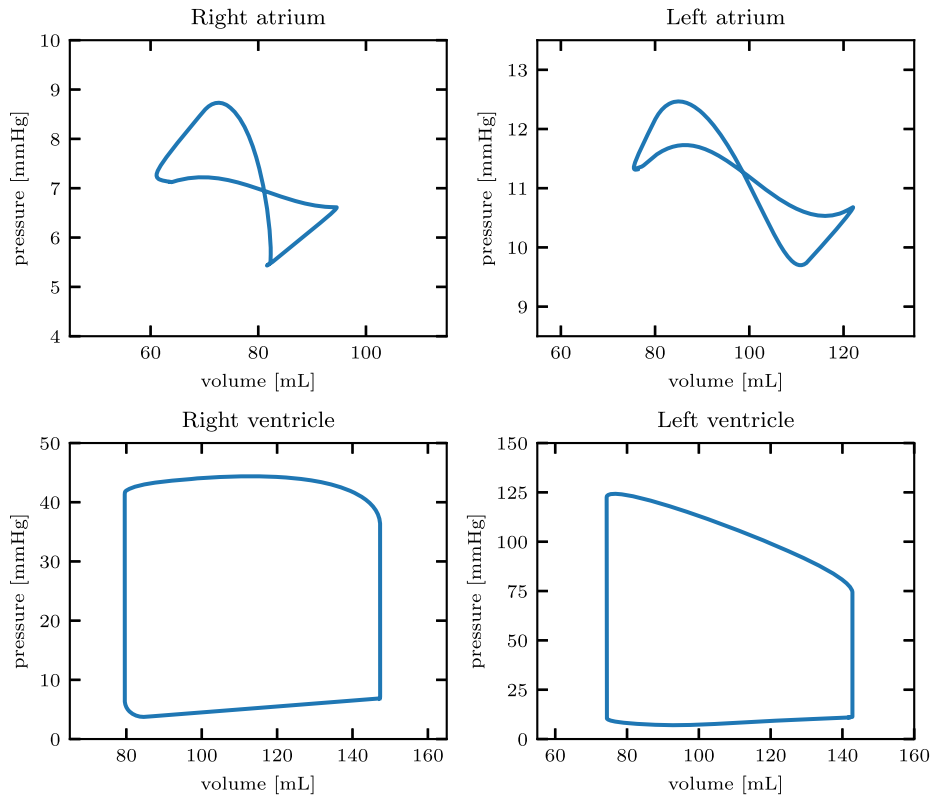
**Fig. 14.** PV loops of the left atrium (top-right), right atrium (top-left), left ventricle (bottom-right) and right ventricle (bottom-left) during the last cardiac cycle of the baseline simulation.
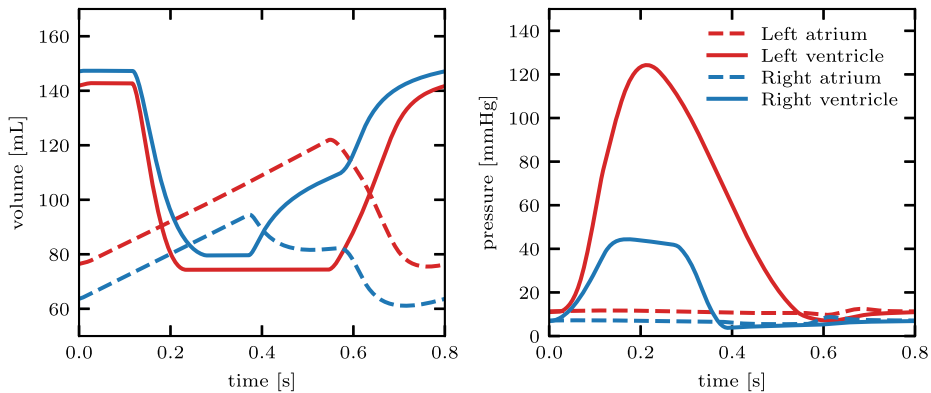


**Fig. 15.** Pressure (right) and volume (left) over time of the left atrium, right atrium, left ventricle and right ventricle during the last cardiac cycle of the baseline simulation.

coming publications. Similarly, the pipeline to reconstruct the reference geometry can be generalized and employed for both atria and ventricles.

## CRediT authorship contribution statement

**F. Regazzoni:** Conceptualization, Formal analysis, Methodology, Software, Writing – original draft. **M. Salvador:** Conceptualization, Formal analysis, Methodology, Software, Writing – original draft. **P.C. Africa:** Methodology, Software, Writing – review & editing. **M. Fedele:** Methodology, Software, Writing – review & editing. **L. Dedè:** Conceptualization, Project administration, Writing – review & editing. **A. Quarteroni:** Conceptualization, Funding acquisition, Project administration, Writing – review & editing.
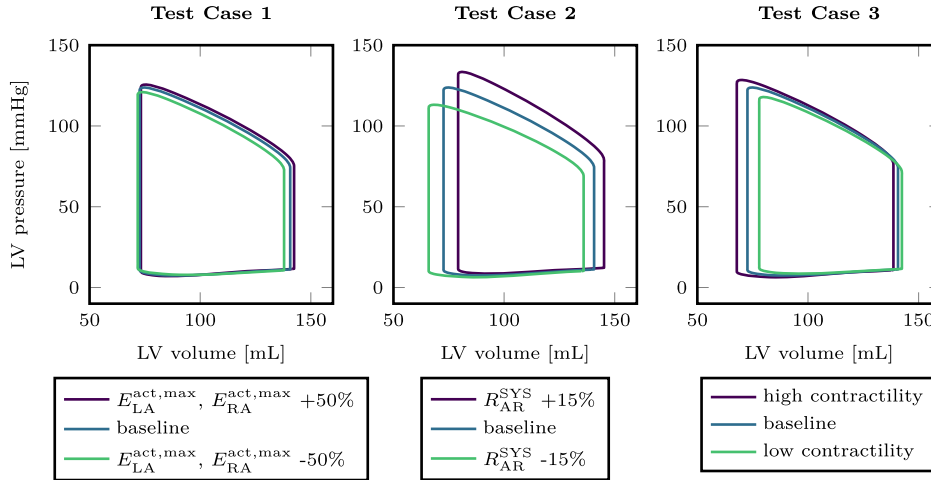
**Fig. 16.** Left ventricle PV loops obtained in the three Test Cases of Sec. 6.2 compared with baseline.

**Table 1**
Parameters of the electrophysiological model.

| Variable | Value | Unit | Variable | Value | Unit |
|----------|-------|------|----------|-------|------|
| **Conductivity tensor** | | | **Applied current** | | |
| $\sigma_{\mathrm{l}}$ | $0.7643 \cdot 10^{-4}$ | $\mathrm{m^2\,s^{-1}}$ | $\widehat{\mathcal{I}}_{\mathrm{app}}^{\mathrm{max}}$ | 35 | $\mathrm{V\,s^{-1}}$ |
| $\sigma_{\mathrm{t}}$ | $0.3494 \cdot 10^{-4}$ | $\mathrm{m^2\,s^{-1}}$ | $t_{\mathrm{app}}$ | $3 \cdot 10^{-3}$ | s |
| $\sigma_{\mathrm{n}}$ | $0.1125 \cdot 10^{-4}$ | $\mathrm{m^2\,s^{-1}}$ | | | |

## Declaration of competing interest

## Acknowledgements

## Appendix A. Model parameters

We provide the full list of parameters adopted for the simulations referred as baseline in Sec. 6.2. Specifically, Table 1 contains the parameters related to the electrophysiological model, Table 2 those related to the mechanical model and, finally, Table 3 contains the parameters of the circulation model. For the TTP06 model, we adopt the parameters reported in the original paper (for M cells) [59]. For the RDQ18 model, we employ the parameters of the original paper [32].

## Appendix B. Parameters of the linear and nonlinear solvers

We report the setting used for the linear (Table 4) and nonlinear (Table 5) solvers to produce the results shown in this paper.

**Table 2**
Parameters of the mechanical model.

| Variable | Value | Unit | Variable | Value | Unit |
|---|---|---|---|---|---|
| **Constitutive law** | | | **Boundary conditions** | | |
| $B$ | $50 \cdot 10^3$ | Pa | $K_\perp^{\text{epi}}$ | $2 \cdot 10^5$ | $\text{Pa}\,\text{m}^{-1}$ |
| $C$ | $0.88 \cdot 10^3$ | Pa | $K_\parallel^{\text{epi}}$ | $2 \cdot 10^4$ | $\text{Pa}\,\text{m}^{-1}$ |
| $b_{\text{ff}}$ | 8 | – | $C_\perp^{\text{epi}}$ | $2 \cdot 10^4$ | $\text{Pa}\,\text{s}\,\text{m}^{-1}$ |
| $b_{\text{ss}}$ | 6 | – | $C_\parallel^{\text{epi}}$ | $2 \cdot 10^3$ | $\text{Pa}\,\text{s}\,\text{m}^{-1}$ |
| $b_{\text{nn}}$ | 3 | – | | | |
| $b_{\text{fs}}$ | 12 | – | **Activation** | | |
| $b_{\text{fn}}$ | 3 | – | $T_{\text{a}}^{\max}$ | $180 \cdot 10^3$ | Pa |
| $b_{\text{sn}}$ | 3 | – | $SL_0$ | 2 | μm |
| $\rho_{\text{s}}$ | $10^3$ | $\text{kg}\,\text{m}^{-3}$ | | | |

**Table 3**
Parameters of the circulation model. We always consider a heartbeat period $T = 0.8$ s.

| Variable | Value | Unit | Variable | Value | Unit |
|---|---|---|---|---|---|
| **External circulation** | | | **Cardiac chambers** | | |
| $R_{\text{AR}}^{\text{SYS}}$ | 0.8 | $\text{mmHg}\,\text{s}\,\text{mL}^{-1}$ | $E_{\text{LA}}^{\text{pass}}$ | 0.09 | $\text{mmHg}\,\text{mL}^{-1}$ |
| $R_{\text{AR}}^{\text{PUL}}$ | 0.1625 | $\text{mmHg}\,\text{s}\,\text{mL}^{-1}$ | $E_{\text{RA}}^{\text{pass}}$ | 0.07 | $\text{mmHg}\,\text{mL}^{-1}$ |
| $R_{\text{VEN}}^{\text{SYS}}$ | 0.26 | $\text{mmHg}\,\text{s}\,\text{mL}^{-1}$ | $E_{\text{RV}}^{\text{pass}}$ | 0.05 | $\text{mmHg}\,\text{mL}^{-1}$ |
| $R_{\text{VEN}}^{\text{PUL}}$ | 0.1625 | $\text{mmHg}\,\text{s}\,\text{mL}^{-1}$ | $E_{\text{LA}}^{\text{act,max}}$ | 0.07 | $\text{mmHg}\,\text{mL}^{-1}$ |
| $C_{\text{AR}}^{\text{SYS}}$ | 1.2 | $\text{mL}\,\text{mmHg}^{-1}$ | $E_{\text{RA}}^{\text{act,max}}$ | 0.06 | $\text{mmHg}\,\text{mL}^{-1}$ |
| $C_{\text{AR}}^{\text{PUL}}$ | 10.0 | $\text{mL}\,\text{mmHg}^{-1}$ | $E_{\text{RV}}^{\text{act,max}}$ | 0.55 | $\text{mmHg}\,\text{mL}^{-1}$ |
| $C_{\text{VEN}}^{\text{SYS}}$ | 60.0 | $\text{mL}\,\text{mmHg}^{-1}$ | $V_{0,\text{LA}}$ | 4.0 | mL |
| $C_{\text{VEN}}^{\text{PUL}}$ | 16.0 | $\text{mL}\,\text{mmHg}^{-1}$ | $V_{0,\text{RA}}$ | 4.0 | mL |
| $L_{\text{AR}}^{\text{SYS}}$ | $5 \cdot 10^{-3}$ | $\text{mmHg}\,\text{s}^2\,\text{mL}^{-1}$ | $V_{0,\text{RV}}$ | 10.0 | mL |
| $L_{\text{AR}}^{\text{PUL}}$ | $5 \cdot 10^{-4}$ | $\text{mmHg}\,\text{s}^2\,\text{mL}^{-1}$ | $t_{\text{C}}^{\text{LA}}$ | 0.6 | s |
| $L_{\text{VEN}}^{\text{SYS}}$ | $5 \cdot 10^{-4}$ | $\text{mmHg}\,\text{s}^2\,\text{mL}^{-1}$ | $T_{\text{C}}^{\text{LA}}$ | 0.104 | s |
| $L_{\text{VEN}}^{\text{PUL}}$ | $5 \cdot 10^{-4}$ | $\text{mmHg}\,\text{s}^2\,\text{mL}^{-1}$ | $T_{\text{R}}^{\text{LA}}$ | 0.68 | s |
| **Cardiac valves** | | | $t_{\text{C}}^{\text{RA}}$ | 0.56 | s |
| $R_{\min}$ | 0.0075 | $\text{mmHg}\,\text{s}\,\text{mL}^{-1}$ | $T_{\text{C}}^{\text{RA}}$ | 0.064 | s |
| $R_{\max}$ | 75000 | $\text{mmHg}\,\text{s}\,\text{mL}^{-1}$ | $T_{\text{R}}^{\text{RA}}$ | 0.64 | s |
| | | | $t_{\text{C}}^{\text{RV}}$ | 0.0 | s |
| | | | $T_{\text{C}}^{\text{RV}}$ | 0.272 | s |
| | | | $T_{\text{R}}^{\text{RV}}$ | 0.12 | s |

**Table 4**
Tolerances of the linear solver for the different physics.

| Physics/Fields | Linear solver | Abs. tol. |
|---|---|---|
| Monodomain model | CG | $10^{-10}$ |
| Activation | GMRES | $10^{-10}$ |
| Mechanics | GMRES | $10^{-8}$ |

**Table 5**
Tolerances of the nonlinear solver for the mechanical problem.

| Physics/Fields | Nonlinear solver | Rel. tol. | Abs. tol. |
|---|---|---|---|
| Mechanics | Quasi-Newton | $10^{-10}$ | $10^{-8}$ |
| Reference configuration | Newton | $10^{-10}$ | $10^{-8}$ |

# References

[1] A.M. Katz, Physiology of the Heart, Lippincott Williams & Wilkins, 2010.
[2] A. Quarteroni, L. Dede', A. Manzoni, C. Vergara, Mathematical Modelling of the Human Cardiovascular System: Data, Numerical Approximation, Clinical Applications, Cambridge Monographs on Applied and Computational Mathematics, Cambridge University Press, 2019.
[3] N.A. Trayanova, Computational cardiology: the heart of the matter, ISRN Cardiol. 2012 (2012) 269680.

[4] N.A. Trayanova, Whole-heart modeling applications to cardiac electrophysiology and electromechanics, Circ. Res. 108 (2011) 113–128.

[5] A. Lee, C.M. Costa, M. Strocchi, et al., Computational modeling for cardiac resynchronization therapy, J. Cardiovasc. Transl. Res. 11 (2018) 92–108.

[6] F. Del Bianco, P. Colli Franzone, S. Scacchi, L. Fassina, Electromechanical effects of concentric hypertrophy on the left ventricle: a simulation study, Comput. Biol. Med. 99 (2018) 236–256.

[7] M. Strocchi, C.M. Augustin, M.A.F. Gsell, et al., A publicly available virtual cohort of four-chamber heart meshes for cardiac electro-mechanics simulations, PLoS ONE 15 (2020) 1–26.

[8] M. Salvador, M. Fedele, P.C. Africa, et al., Electromechanical modeling of human ventricles with ischemic cardiomyopathy: numerical simulations in sinus rhythm and under arrhythmia, Comput. Biol. Med. 136 (2021) 104674.

[9] Z.J. Wang, A. Santiago, X. Zhou, et al., Human biventricular electromechanical simulations on the progression of electrocardiographic and mechanical abnormalities in post-myocardial infarction, EP Europace 23 (Supplement1) (2021) i143–i152.

[10] D. Chapelle, M.A. Fernández, J.F. Gerbeau, et al., Numerical simulation of the electromechanical activity of the heart, in: International Conference on Functional Imaging and Modeling of Heart, vol. 5528, 2009, pp. 357–365.

[11] L. Marx, M.A.F. Gsell, A. Rund, et al., Personalization of electro-mechanical models of the pressure-overloaded left ventricle: fitting of windkessel-type afterload models, Philos. Trans. R. Soc., Math. Phys. Eng. Sci. 378 (2020) 1015–1034.

[12] D.A. Nordsletten, S.A. Niederer, M.P. Nash, et al., Coupling multi-physics models to cardiac mechanics, Prog. Biophys. Mol. Biol. 104 (2011) 77–88.

[13] R. Piersanti, F. Regazzoni, M. Salvador, A.F. Corno, L. Dede, C. Vergara, A. Quarteroni, 3D–0D closed-loop model for the simulation of cardiac biventricular electromechanics, Comput. Methods Appl. Mech. Eng. 391 (2022) 114607.

[14] M. Salvador, L. Dedè, A. Quarteroni, An intergrid transfer operator using radial basis functions with application to cardiac electromechanics, Comput. Mech. 66 (2020) 491–511.

[15] A. Gerbi, L. Dede', A. Quarteroni, A monolithic algorithm for the simulation of cardiac electromechanics in the human left ventricle, Math. Eng. 1 (2018) 1–37.

[16] S. Land, S. Niederer, Influence of atrial contraction dynamics on cardiac function, Int. J. Numer. Methods Biomed. Eng. 34 (2018).

[17] C. Augustin, T.E. Fastl, A. Neic, et al., The impact of wall thickness and curvature on wall stress in patient-specific electromechanical models of the left atrium, Biomech. Model. Mechanobiol. 19 (2019) 1015–1034.

[18] C.M. Augustin, A. Neic, M. Liebmann, A.J. Prassl, S.A. Niederer, G. Haase, G. Plank, Anatomically accurate high resolution modeling of human whole heart electromechanics: a strongly scalable algebraic multigrid solver method for nonlinear deformation, J. Comput. Phys. 305 (2016) 622–646.

[19] T. Gerach, S. Schuler, J. Fröhlich, et al., Electro-mechanical whole-heart digital twins: a fully coupled multi-physics approach, Mathematics 9 (11) (2021).

[20] A. Santiago, J. Aguado-Sierra, M. Zavala-Ake, et al., Fully coupled fluid-electro-mechanical model of the human heart for supercomputers, Int. J. Numer. Methods Biomed. Eng. 34 (2018) e3140.

[21] M. Strocchi, M.A. Gsell, C.M. Augustin, et al., Simulating ventricular systolic motion in a four-chamber heart model with spatially varying robin boundary conditions to model the effect of the pericardium, J. Biomech. 101 (2020) 109645.

[22] N. Smith, D. Nickerson, E. Crampin, P. Hunter, Multiscale computational modelling of the heart, Acta Numer. 13 (2004) 371–431.

[23] E.J. Crampin, M. Halstead, P. Hunter, P. Nielsen, D. Noble, N. Smith, M. Tawhai, Computational physiology and the physiome project, Exp. Physiol. 89 (1) (2004) 1–26.

[24] R. Chabiniok, V. Wang, M. Hadjicharalambous, L. Asner, J. Lee, M. Sermesant, E. Kuhl, A. Young, P. Moireau, M. Nash, D. Chapelle, D. Nordsletten, Multiphysics and multiscale modelling, data–model fusion and integration of organ physiology in the clinic: ventricular cardiac mechanics, Interface Focus 6 (2) (2016) 20150083.

[25] D. Bers, Excitation-Contraction Coupling and Cardiac Contractile Force, vol. 237, Springer Science & Business Media, 2001.

[26] S. Land, S. Park-Holohan, N. Smith, C. dos Remedios, J. Kentish, S. Niederer, A model of cardiac contraction based on novel measurements of tension development in human cardiomyocytes, J. Mol. Cell. Cardiol. 106 (2017) 68–83.

[27] S.A. Niederer, P.J. Hunter, N.P. Smith, A quantitative analysis of cardiac myocyte relaxation: a simulation study, Biophys. J. 90 (5) (2006) 1697–1722.

[28] J. Rice, F. Wang, D. Bers, P. de Tombe, Approximate model of cooperative activation and crossbridge cycling in cardiac muscle using ordinary differential equations, Biophys. J. 95 (5) (2008) 2368–2390.

[29] J. Hussan, P. de Tombe, J. Rice, A spatially detailed myofilament model as a basis for large-scale biological simulations, IBM J. Res. Dev. 50 (6) (2006) 583–600.

[30] T. Washio, J. Okada, A. Takahashi, K. Yoneda, Y. Kadooka, S. Sugiura, T. Hisada, Multiscale heart simulation with cooperative stochastic cross-bridge dynamics and cellular structures, Multiscale Model. Simul. 11 (4) (2013) 965–999.

[31] T. Washio, K. Yoneda, J. Okada, T. Kariya, S. Sugiura, T. Hisada, Ventricular fiber optimization utilizing the branching structure, Int. J. Numer. Methods Biomed. Eng. (2015).

[32] F. Regazzoni, L. Dede', A. Quarteroni, Active contraction of cardiac cells: a model for sarcomere dynamics with cooperative interactions, Biomech. Model. Mechanobiol. 17 (2018) 1663–1686.

[33] F. Regazzoni, L. Dedè, A. Quarteroni, Machine learning of multiscale active force generation models for the efficient simulation of cardiac electromechanics, Comput. Methods Appl. Mech. Eng. 370 (2020) 113268.

[34] G.W. Jenkins, C.P. Kemnitz, G.J. Tortora, Anatomy and Physiology: From Science to Life, Wiley, Hoboken, 2007.

[35] F. Regazzoni, Mathematical modeling and machine learning for the numerical simulation of cardiac electromechanics, Ph.D. thesis, Politecnico di Milano, 2020.

[36] C. Felippa, K. Park, C. Farhat, Partitioned analysis of coupled mechanical systems, Comput. Methods Appl. Mech. Eng. 190 (24) (2001) 3247–3270.

[37] A. Gerbi, Numerical approximation of cardiac electro-fluid-mechanical models: coupling strategies for large-scale simulation, Ph.D. thesis, EPFL, 2018.

[38] L. Dede', A. Gerbi, A. Quarteroni, Segregated algorithms for the numerical simulation of cardiac electromechanics in the left human ventricle, in: The Mathematics of Mechanobiology, Springer, 2020, pp. 81–116.

[39] F. Regazzoni, A. Quarteroni, An oscillation-free fully partitioned scheme for the numerical modeling of cardiac active mechanics, Comput. Methods Appl. Mech. Eng. 373 (2021) 113506.

[40] A. Quarteroni, T. Lassila, S. Rossi, R. Ruiz-Baier, Integrated heart – coupling multiscale and multiphysics models for the simulation of the cardiac function, Comput. Methods Appl. Mech. Eng. 314 (2017) 345–407.

[41] P. Pathmanathan, S. Chapman, D. Gavaghan, J. Whiteley, Cardiac electromechanics: the effect of contraction model on the mathematical problem and accuracy of the numerical scheme, Q. J. Mech. Appl. Math. 63 (3) (2010) 375–399.

[42] C. Carton de Wiart, L.T. Diosady, A. Garai, N.K. Burgess, P.J. Blonigan, D. Ekelschot, S.M. Murman, Design of a modular monolithic implicit solver for multi-physics applications, in: 2018 AIAA Aerospace Sciences Meeting, 2018, p. 1400.

[43] D. Boffi, L.F. Pavarino, G. Rozza, S. Scacchi, C. Vergara, Mathematical and Numerical Modeling of the Cardiovascular System and Applications, vol. 16, Springer, 2018.

[44] M. Fink, S. Niederer, E. Cherry, F. Fenton, J. Koivumäki, G. Seemann, R. Thul, H. Zhang, F. Sachse, D. Beard, E. Crampin, N. Smith, Cardiac cell modelling: observations from the heart of the cardiac physiome project, Prog. Biophys. Mol. Biol. 104 (1) (2011) 2–21.

[45] M. Vázquez, R. Arís, J. Aguado-Sierra, G. Houzeaux, A. Santiago, M. López, P. Córdoba, M. Rivero, J. Cajas, Alya Red CCM: HPC-based cardiac computational modelling, in: Selected Topics of Computational and Experimental Fluid Mechanics, Springer, 2015, pp. 189–207.

[46] P.C. Africa, Scalable adaptive simulation of organic thin-film transistors, Ph.D. thesis, Politecnico di Milano, 2019.
[47] P. Gervasio, A. Quarteroni, The INTERNODES method for non-conforming discretizations of PDEs, Commun. Appl. Math. Comput. Sci. 1 (2019) 361–401.
[48] A. Quarteroni, R. Sacco, F. Saleri, Numerical Mathematics, Springer, 2010.
[49] P.J. Blanco, R.A. Feijóo, A 3D-1D-0D computational model for the entire cardiovascular system, Comput. Mech. 24 (2010) 5887–5911.
[50] M. Hirschvogel, M. Bassilious, L. Jagschies, et al., A monolithic 3D-0D coupled closed-loop model of the heart and the vascular system: experiment-based parameter estimation for patient-specific cardiac mechanics, Int. J. Numer. Methods Biomed. Eng. 33 (8) (2017) e2842.
[51] M. Benzi, G.H. Golub, J. Liesen, Numerical solution of saddle point problems, Acta Numer. 14 (2005) 1–137.
[52] Zygote Media Group Inc., Zygote solid 3D heart generation II development report, Technical Report, 2014.
[53] P. Colli Franzone, L.F. Pavarino, G. Savaré, Computational Electrocardiology: Mathematical and Numerical Modeling, Springer, 2006, pp. 187–241.
[54] P. Colli Franzone, L.F. Pavarino, S. Scacchi, A numerical study of scalable cardiac electro-mechanical solvers on HPC architectures, Front. Physiol. 9 (2018) 268.
[55] M. Potse, B. Dubé, J. Richer, et al., A comparison of monodomain and bidomain reaction-diffusion models for action potential propagation in the human heart, IEEE Trans. Biomed. Eng. 53 (2006) 2425–2435.
[56] J. Sainte-Marie, D. Chapelle, R. Cimrman, et al., Modeling and estimation of the cardiac electromechanical activity, Comput. Struct. 84 (2006) 1743–1759.
[57] A. Bueno-Orovio, E.M. Cherry, F.H. Fenton, Minimal model for human ventricular action potentials in tissue, J. Theor. Biol. 253 (2008) 544–560.
[58] C. Luo, Y. Rudy, A dynamic model of the cardiac ventricular action potential. I. Simulations of ionic currents and concentration changes, Circ. Res. 74 (1994) 1071–1096.
[59] K.H. ten Tusscher, A.V. Panfilov, Alternans and spiral breakup in a human ventricular tissue model, Am. J. Physiol., Heart Circ. Physiol. 291 (2006) 1088–1100.
[60] F. Regazzoni, L. Dedè, A. Quarteroni, Biophysically detailed mathematical models of multiscale cardiac active mechanics, PLoS Comput. Biol. 16 (10) (2020) e1008294.
[61] S. Rossi, R. Ruiz-Baier, L.F. Pavarino, A. Quarteroni, Orthotropic active strain models for the numerical simulation of cardiac biomechanics, Int. J. Numer. Methods Biomed. Eng. 28 (2012) 761–788.
[62] S. Rossi, T. Lassila, R. Ruiz-Baier, et al., Thermodynamically consistent orthotropic activation model capturing ventricular systolic wall thickening in cardiac electromechanics, Eur. J. Mech. A, Solids 48 (2014) 129–142.
[63] R. Ruiz-Baier, A. Gizzi, S. Rossi, et al., Mathematical modelling of active contraction in isolated cardiomyocytes, Math. Med. Biol. 31 (2014) 259–283.
[64] J.M. Guccione, A.D. McCulloch, L.K. Waldman, Passive material properties of intact ventricular myocardium determined from a cylindrical model, J. Biomech. Eng. 113 (1991) 42–55.
[65] R. Ogden, Non-linear Elastic Deformations, Dover Publications, 1997.
[66] P. Colli Franzone, L.F. Pavarino, S. Scacchi, Mathematical Cardiac Electrophysiology, Springer, 2014.
[67] M. Landajuela, C. Vergara, A. Gerbi, et al., Numerical approximation of the electromechanical coupling in the left ventricle with inclusion of the Purkinje network, Int. J. Numer. Methods Biomed. Eng. 34 (2018) e2984.
[68] D. Romero, R. Sebastian, B.H. Bijnens, et al., Effects of the Purkinje system and cardiac geometry on biventricular pacing: a model study, Ann. Biomed. Eng. 38 (2010) 1388–1398.
[69] C. Vergara, M. Lange, S. Palamara, et al., A coupled 3D-1D numerical monodomain solver for cardiac electrical activation in the myocardium with detailed Purkinje network, J. Comput. Phys. 308 (2016) 218–238.
[70] J.E. Saffitz, H.L. Kanter, K.G. Green, et al., Tissue-specific determinants of anisotropic conduction velocity in canine atrial and ventricular myocardium, Circ. Res. 74 (1994) 1065–1070.
[71] J.D. Bayer, R.C. Blake, G. Plank, N.A. Trayanova, A novel rule-based algorithm for assigning myocardial fiber orientation to computational heart models, Ann. Biomed. Eng. 40 (2012) 2243–2254.
[72] R. Doste, D. Soto-Iglesias, G. Bernardino, A rule-based method to model myocardial fiber orientation in cardiac biventricular geometries with outflow tracts, Int. J. Numer. Methods Biomed. Eng. 35 (2019).
[73] R. Piersanti, P.C. Africa, M. Fedele, C. Vergara, L. Dede', A.F. Corno, A. Quarteroni, Modeling cardiac muscle fibers in ventricular and atrial electrophysiology simulations, Comput. Methods Appl. Mech. Eng. 373 (2021) 113468.
[74] L. Azzolin, L. Dede', A. Gerbi, A. Quarteroni, Effect of fibre orientation and bulk modulus on the electromechanical modelling of human ventricles, Math. Eng. 2 (2020) 614 (mine-02-04-028).
[75] M. Caruel, L. Truskinovsky, Physics of muscle contraction, Rep. Prog. Phys. 81 (3) (2018) 036602.
[76] F. Regazzoni, L. Dedè, A. Quarteroni, Machine learning for fast and reliable solution of time-dependent differential equations, J. Comput. Phys. 397 (2019) 108852.
[77] J.M. Guccione, A.D. McCulloch, Finite element modeling of ventricular mechanics, in: Theory of Heart, Springer, 1991, pp. 121–144.
[78] A. Cheng, F. Langer, F. Rodriguez, et al., Transmural cardiac strains in the lateral wall of the ovine left ventricle, Am. J. Physiol., Heart Circ. Physiol. 288 (2005) 1546–1556.
[79] S. Doll, K. Schweizerhof, On the development of volumetric strain energy functions, J. Appl. Math. 67 (2000) 17–21.
[80] F.C. Yin, C.C. Chan, R.M. Judd, Compressibility of perfused passive myocardium, Am. J. Physiol., Heart Circ. Physiol. 271 (1996) 1864–1870.
[81] S. Rossi, Anisotropic modeling of cardiac mechanical activation, Ph.D. thesis, EPFL, 2014.
[82] S. Klotz, I. Hay, M.L. Dickstein, G.-H. Yi, J. Wang, M.S. Maurer, D.A. Kass, D. Burkhoff, Single-beat estimation of end-diastolic pressure-volume relationship: a novel method with potential for noninvasive application, Am. J. Physiol., Heart Circ. Physiol. 291 (1) (2006) H403–H412.
[83] T.M. Nosek, Essentials of Human Physiology, Gold Standard Multimedia, 1998.
[84] S. Godunov, A difference method for numerical calculation of discontinuous solutions of the equations of hydrodynamics, Mat. Sb. 89 (1959) 271–306.
[85] C. Burstedde, L.C. Wilcox, O. Ghattas, p4est: scalable algorithms for parallel adaptive mesh refinement on forests of octrees, SIAM J. Sci. Comput. 33 (3) (2011) 1103–1133.
[86] S. Krishnamoorthi, M. Sarkar, W.S. Klug, Numerical quadrature and operator splitting in finite element methods for cardiac electrophysiology, Int. J. Numer. Methods Biomed. Eng. 29 (2003) 1243–1266.
[87] A.S. Patelli, L. Dede', T. Lassila, et al., Isogeometric approximation of cardiac electrophysiology models on surfaces: an accuracy study with application to the human left atrium, Comput. Methods Appl. Mech. Eng. 317 (2017) 248–273.
[88] P. Pathmanathan, M.O. Bernabeu, S.A. Niederer, et al., Computational modelling of cardiac electrophysiology: explanation of the variability of results from different numerical solvers, Int. J. Numer. Methods Biomed. Eng. 28 (2012) 890–903.
[89] P. Pathmanathan, G.R. Mirams, J. Southern, et al., The significant effect of the choice of ionic current integration method in cardiac electro-physiological simulations, Int. J. Numer. Methods Biomed. Eng. 27 (2011) 1751–1770.
[90] B.E. Griffith, N.A. Patankar, Immersed methods for fluid-structure interaction, Annu. Rev. Fluid Mech. 52 (2020) 421–448.
[91] Y. Bao, A. Donev, B.E. Griffith, An immersed boundary method with divergence-free velocity interpolation, J. Comput. Phys. 347 (2017) 183–206.
[92] R.C. Kerckhoffs, M.L. Neal, Q. Gu, J.B. Bassingthwaighte, J.H. Omens, A.D. McCulloch, Coupling of a 3D finite element model of cardiac ventricular mechanics to lumped systems models of the systemic and pulmonic circulation, Ann. Biomed. Eng. 35 (1) (2007) 1–18.
[93] W.J. Schroeder, B. Lorensen, K. Martin, The visualization toolkit: an object-oriented approach to 3D graphics, Kitware (2004).

[94] L. Antiga, M. Piccinelli, L. Botti, B. Ene-Iordache, A. Remuzzi, D.A. Steinman, An image-based modeling framework for patient-specific computational hemodynamics, Med. Biol. Eng. Comput. 46 (11) (2008) 1097.

[95] M. Fedele, A. Quarteroni, Polygonal surface processing and mesh generation tools for the numerical simulation of the cardiac function, Int. J. Numer. Methods Biomed. Eng. 37 (4) (2021) e3435, https://doi.org/10.1002/cnm.3435.

[96] D. Arndt, W. Bangerth, B. Blais, T.C. Clevenger, M. Fehling, A.V. Grayver, T. Heister, L. Heltai, M. Kronbichler, M. Maier, P. Munch, J.-P. Pelteret, R. Rastak, I. Thomas, B. Turcksin, Z. Wang, D. Wells, The deal.II library, version 9.2, J. Numer. Math. 28 (3) (2020) 131–146, https://doi.org/10.1515/jnma-2020-0043, https://dealii.org/deal92-preprint.pdf.